Quantum Transport in Scalable MBE SAG InSb Nanowires for Majorana Bound States

Lieuwe J. Stek

Developments in Selective Area Grown InSb Nanowires using Molecular Beam Epitaxy from Delft

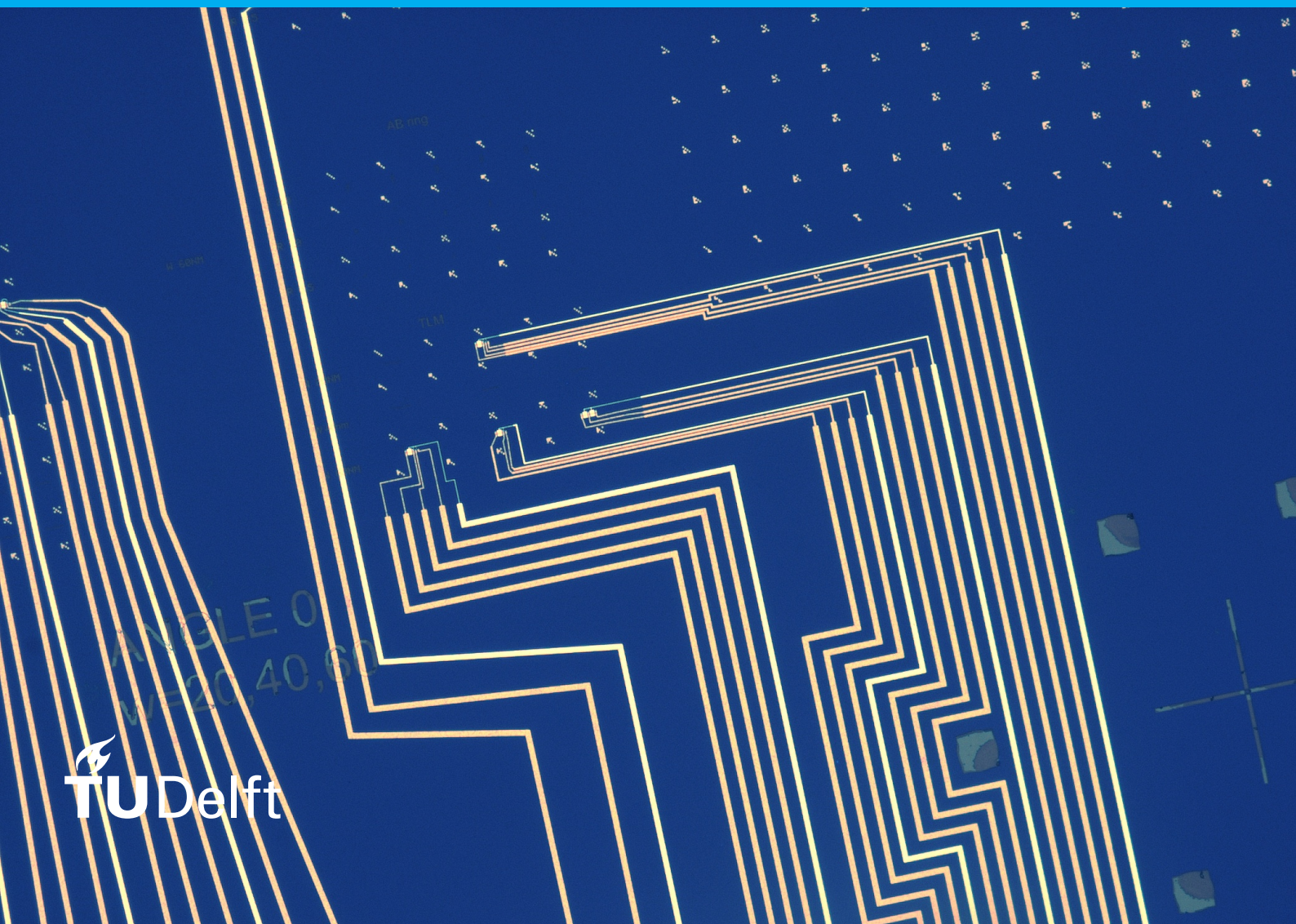

TU Delft

Quantum Transport in Scalable MBE SAG InSb Nanowires for Majorana Bound States

by

Lieuwe J. Stek

to obtain the degree of Master of Science
at the Delft University of Technology,
to be defended publicly on Friday January 25, 2019 at 3 PM.

Student number:	4152166	
Project duration:	April 7, 2018 – January 25, 2019	
Thesis committee:	Prof. dr. ir. L.P. Kouwenhoven,	TU Delft, Microsoft, supervisor
	Prof. dr. G.A. Steele,	TU Delft
	Dr. S. Goswami,	TU Delft
	Dr. ir. G. de Lange,	Microsoft
	G. Wang, PhD candidate,	TU Delft

An electronic version of this thesis is available at `http://repository.tudelft.nl/`.

TU Delft

Contents

Acknowledgements

I cannot believe my masters thesis work is already over, time seems to have gone by so quickly. During my time here, I have learned a great deal and have gotten a taste of what it is like to work in a research group, an experience I am grateful for and will not soon forget. Thesis work is something that is not done alone, and many fine people have helped me over the past many months.

Firstly, I wish to thank Guanzhong Wang and Luca Binci, of whose help and knowledge I have benefited greatly. I could always count on you guys for any questions I had and always received very detailed answers. Our long hours in the cleanroom have certainly shown me how dedicated you guys are. Thank you for your thorough proofreading of my thesis. A few sentences here are not be enough to express how much you have done for me. Thank you!

Gijs de Lange, I always enjoyed the SAG and device meetings. Your hard work in propelling SAG forwards have certainly not gone by unnoticed. Thanks to your efforts we have made a great deal of progress towards making SAG a viable platform.

Leo Kouwenhoven, without your dedication to making topological quantum computing a reality, none of this would exist. Your work has brought so many great people together to work on such an ambitious project. I am grateful for having been able to do my masters thesis project in your group and to have been able to meet so many great people in the process.

Amrita Singh, you are able to handle the fabrication in so many projects simultaneously so well. Thanks to your expertise in developing cleanroom recipes it was possible to make great strides in SAG.

Pavel Aseev and Philippe Caroff, I am impressed by your dedication towards making SAG a success. You guys have great skill and insight in growing our SAG nanowires. I have always enjoyed our conversations and am grateful for your detailed answers to my questions.

Nick, Di, Vanessa, Bart, Jaap, your hard work in the SAG team has certainly made an impression on me and I am grateful for the many discussions we had.

I would also like to extend my gratitude to Alexandra for being such a nice office-space neighbor and being so supportive of me. Stefan and Elvedin, thank you for additional proofreading of my thesis. Your suggestions were very welcome. I would also like to thank the committee members for taking the time to read and evaluate my thesis.

I would like to thank all members of topo for their friendliness and helpfulness. You guys are what make working in this group a great experience.

Finally, I want to thank my parents for their care and warmth and for always having supported me.

1

Introduction

Classical computing, using transistors and binary codes, has ushered in a technological revolution that has changed the world. There exist problems in computing, however, that are hard to solve using classical computers, such as simulating quantum mechanical systems [1] or secure key exchange mechanisms for cryptography over public communications channels [2, 3]. Finding solutions to these problems is of great interest to both science and industry. Take for example these two particular cases. The simulation of quantum mechanical systems using a quantum computer would allow us to greatly improve the accuracy and provide the computational power required to study protein folding and the effects of medicine, which are both part of the field of quantum chemistry [4, 5]. Similarly, quantum key exchange is envisioned to become part of the quantum internet [6], where it will perform the task of initiating secure channels for the communications between collaborating parties. Many other computational problems can be solved using quantum algorithms, a comprehensive list of which is being kept by the National Institute of Standards and Technology (NIST) [7]. Quantum computing thus offers solutions to these problems and has been vigorously pursued over the past few decades [8, 9].

Quantum computers use so called quantum bits (qubits) to perform calculations. These qubits can be manipulated using the rules of quantum mechanics, allowing them to become entangled with one another and be in a superposition of quantum states. These special rules of quantum mechanics allow the quantum computer to achieve a considerable speedup compared to classical computers in cases where a suitable quantum algorithm has been found [10].

A common concern in quantum computing is decoherence, where the quantum state of the qubits suddenly changes and no longer represents the problem that is to be solved. Such decoherence can happen at random, but is often described by an expectation value of the coherence time. This is where topological quantum computation offers a unique solution. By using non-abelian anyons, which follow different exchange statistics from bosons and fermions, quantum states can be encoded and protected thanks to topology. To understand the role of topology, let us first consider braiding. Braiding is the operation of exchanging any two of these anyons. This exchange, when viewed from the point of view of knot theory [11], will look like a braid, where each exchange will move the 'world lines' of the anyons around one another [12, 13]. Because the quantum information is stored and manipulated by exchanging the anyons, small perturbations do not affect the stored quantum information, because small perturbations will not move the anyons back around one another. This protection is analogous to the topology of objects in mathematics, where continuous deformations (hemeomorphisms) of objects do not change their topological space [14]. In the case of this work, the non-abelian anyons are Majorana bound states. This work focuses on the transport characteristics of a recently developed growth method for nanowires in which these Majoranas are predicted to appear, particularly selective area growth of large spin-orbit interaction semiconductor nanowires using molecular beam epitaxy.

Chapter 2 will outline the basics of Majorana physics. Starting from the Kitaev chain, the ingredients for finding Majoranas in nanowires will be discussed. The physics related to the classical and quantum transport will be explained, which will be used to explain the transport measurements of the nanowires.

Chapter 3 will explain the cryogenics and measurement methods used to perform the measurements.

Chapter 4 will discuss the growth of nanowires and the fabrication of devices. Cleanroom procedures used will be discussed and the recipes used for fabrication are outlined.

Scalability is essential if a topological quantum computer is to be realized. Chapter 5 discusses the requirements of scalability and some of the progress made towards it, both in the context of scalable design as well as scalable fabrication.

Lastly, in chapter 6 the transport results will be discussed, showing the results of the measurements performed for this work.

2

Theoretical background

To understand the results presented in this work, it is important to first understand the underlying physics, which will be presented in this chapter. In section 2.1, the basics of Majorana physics and formalism will be explained. Starting from the Kitaev chain toy model, we will shift our thinking towards fundamental (cosmic) particles as quasiparticle excitations in condensed matter. The physical requirements for finding Majorana fermions in one-dimensional structures is then outlined, followed by sections 2.2, 2.3 and 2.4 which will explain each component (superconductivity, Zeeman effect and spin-orbit interaction, respectively) in this recipe. The resulting topological gap will be discussed in section 2.5 and its importance for topological protected quantum computation will be outlined. Electronic transport, both classical and quantum, will be discussed in sections 2.6 and 2.7.

2.1. Majorana fermions

In 1937, Italian physicist Ettore Majorana published his paper [15] predicting the existence of a fermionic particle which is its own anti-particle, and found them as real solutions to the Dirac equation. This property of Majoranas, written in second quantization language as $\hat{\gamma}^\dagger = \hat{\gamma}$, restricts several properties a Majorana particle can have. Electric charge, for instance, must be zero, otherwise the Hermitian conjugate of the Majorana annihilation operator $\hat{\gamma}$ would be required to have opposite charge to the creation operator $\hat{\gamma}^\dagger$ in order not to violate charge conservation, but this would then violate the equality of both operators. Ongoing particle physics research [16, 17] studies neutrinos produced in neutrino-less double beta ($0\nu\beta\beta$) decay to probe whether neutrinos are cosmological Majoranas. Instead of looking for cosmological Majoranas, systems of many particles collectively behaving as fundamental particles can be found in condensed matter as the collective behavior of electrons, so called quasiparticle states. Possibly the most famous is the electron-hole, where the absence of an electron leaves a void (or hole), which behaves as if it is a positron, the anti-electron, albeit with modified parameters such as effective mass and mobility. Similarly, collective electron behavior can lead to Majorana quasiparticles.

2.1.1. Kitaev chain

The Hamiltonian of a spinless p-wave superconductor with tight-binding is given by [13]

$$\mathscr{H}_{\text{chain}} = -\mu \sum_{j=1}^{N} \hat{n}_j - \sum_{j=1}^{N-1} (t\hat{c}_j^\dagger \hat{c}_{j+1} + \Delta \hat{c}_j \hat{c}_{j+1} + \text{h.c.}) \tag{2.1}$$

where μ is the chemical potential, $\hat{n}_j = \hat{c}_j^\dagger \hat{c}_j$ the number operator, t the hopping amplitude, $\Delta = |\Delta|$ the superconducting order parameter and h.c. indicates the Hermitian conjugate of the preceding terms. If we consider an electron be composed of a real and imaginary part, the electron can be seen as being composed of two Majorana particles. We can thus write the electron annihilation and creation operators for an electron at site j as

$$\hat{c}_j = \frac{\hat{\gamma}_{j,1} + i\hat{\gamma}_{j,2}}{2} \qquad \text{and} \qquad \hat{c}_j^\dagger = \frac{\hat{\gamma}_{j,1} - i\hat{\gamma}_{j,2}}{2} \tag{2.2}$$

where $\gamma_{j,n}$ represents the n-th Majorana of fermion j. From this formalism, the expressions for the Majorana operators can be represented in fermionic operators as

$$\hat{\gamma}_{j,1} = \hat{c}_j^\dagger + \hat{c}_j \qquad \text{and} \qquad \hat{\gamma}_{j,2} = i(\hat{c}_j^\dagger - \hat{c}_j) \tag{2.3}$$

This type of pairing, that pairs two Majoranas originating from the same fermion, is shown in figure 2.1 top panel. The Majoranas (black dots) making up in the same fermion (lightblue) are paired up (solid line) such that the pairing between $\gamma_{j,1}$ and $\gamma_{j,2}$ resides entirely inside the *same* fermion c_j.

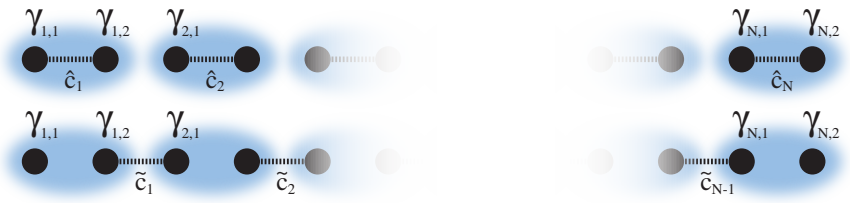

Figure 2.1: Kitaev's toy model. **Top panel**: Majoranas (black circles) at the same site j pair-up (line); **bottom panel**: two Majoranas from adjacent sites j and $j+1$ pair up. A delocalized state is formed at the extremities of the chain.

Another type of pairing where the Majoranas of *neighboring* sites j and $j+1$ pair up was proposed by Kitaev in 2001 [18] and is shown in figure 2.1 bottom panel. This second type of pairing can be derived from equations 2.1 and 2.2. To arrive at this situation, assume $\mu = 0,\ t = \Delta > 0$. In this regime, the Hamiltonian from equation 2.1 reduces to

$$\mathscr{H}_{\text{chain}} = -it \sum_{j=1}^{N-1} \hat{\gamma}_{j,2}\hat{\gamma}_{j+1,1} = 2t \sum_{j=1}^{N-1} \tilde{c}_j^{\dagger}\tilde{c}_j \tag{2.4}$$

where now the new fermionic operators are

$$\tilde{c}_j = \frac{\hat{\gamma}_{j+1,1} + i\hat{\gamma}_{j,2}}{2} \qquad \text{and} \qquad \tilde{c}_j^{\dagger} = \frac{\hat{\gamma}_{j+1,1} - i\hat{\gamma}_{j,2}}{2} \tag{2.5}$$

The tilde on the operators indicates that these fermionic operators act non-locally, that is to say, they do not operate on a fermion at site j, rather the fermion they operate on is spread out over the two nearest-neighbor sites at j and $j+1$. An important aspect of equation 2.4 is that the two Majoranas at $j = 0$ and $j = N$ are *excluded* from the Hamiltonian. This means that there is an additional state

$$\tilde{c}_M = \frac{\hat{\gamma}_{N,2} + i\hat{\gamma}_{1,1}}{2} \tag{2.6}$$

at $E = 0$ comprised of the unpaired Majoranas at the extremities of the chain. This state is highly non-local due to the distance between the Majorana sites. The eigenvalue of the Majorana number operator

$$\tilde{n}_M = \tilde{c}_M^{\dagger}\tilde{c}_M = 0 \text{ or } 1 \tag{2.7}$$

depends on whether the Majorana bound state (MBS) is actually occupied, which would correspond to an extra electron being present in the now degenerate ground state of the p-wave superconductor. This eigenvalue is also called parity, with 0 corresponding to *even* parity (no electron occupies the MBS) and 1 to *odd* parity (MBS is occupied)[1]. Furthermore, when we take a look at some of the properties of the Majorana operators it can be found that

$$\hat{\gamma}_i\hat{\gamma}_j = \hat{\gamma}_i^{\dagger}\hat{\gamma}_j = \delta_{ij} \tag{2.8}$$

$$\{\hat{\gamma}_i, \hat{\gamma}_j\} = 2\delta_{ij} \tag{2.9}$$

This toy model provides a model for MBSs in condensed matter systems. Proposals have been made to engineer such systems as will be described in the next section.

[1] The definition of even or odd parity being either 0 or 1 might as well be vice versa, after all it is just a label.

2.1.2. Recipe for Majoranas in one-dimensional systems

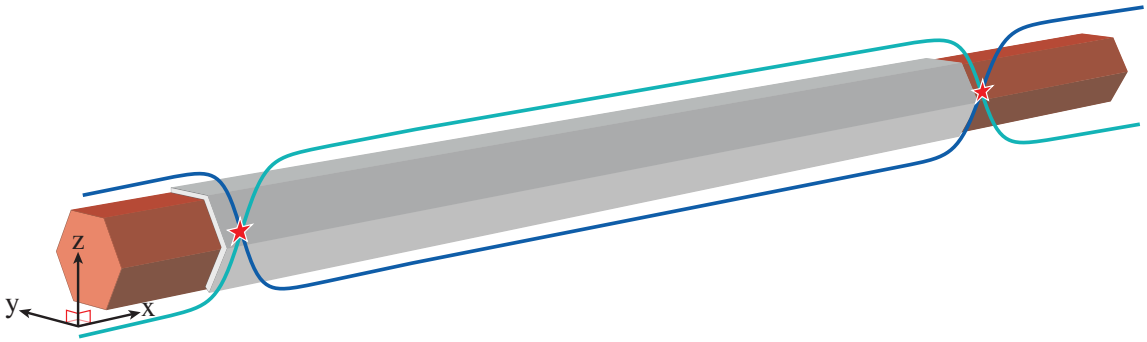

Figure 2.2: Illustration of a proximitized nanowire with strong spin-orbit coupling. Nanowire in red. A layer of s-wave superconductor is shown in grey. Note that the nanowire is elongated in the x-direction. Illustrative gap dispersion shown in dark- and lightblue traces. Crossing of these traces indicates the trivial-topological transition. The locations where Majoranas are predicted to appear are indicated by stars.

Fu and Kane in 2008 [19] proposed a method of creating MBSs by inducing $p_x + ip_y$-type superconductivity. Proximitizing a material with strong spin-orbit coupling with an s-wave superconductor would lead to the formation of such a 2D system, where Majoranas are predicted to arise in vortices. Building upon these ideas, two research groups, Lutchyn *et al.* [20] and Oreg *et al.* [21], independently proposed using nanowires as a 1D system to obtain MBSs in 2010. To achieve this, the following criteria would need to be met:

- nanowire made of a semiconducting material with strong Rashba spin-orbit interaction and large g-factor
- s-wave superconductor proximitizing the nanowire
- external magnetic field

This model is commonly referred to as the *Lutchyn-Oreg model*. All of these ingredients will be further explained in the following sections, however it is useful to briefly introduce them here. The nanowire can be regarded as a 1D system in the sense that it is stretched in a single dimension (say, $\hat{x}$), and confined in the other two dimensions ($\hat{y}$, $\hat{z}$), see figure 2.2. From the perspective of the electrons in the wire, the $\hat{x}$-direction allows for modes with a much longer wavelength, and thus a much lower energy, compared to the other two directions. Therefore, for sufficiently low energies, the occupation of these higher energy modes will be zero, and only the modes in the $\hat{x}$-direction will be excited, thus creating a one-dimensional electronic system in this low-energy regime. To reach this low-energy regime, the system is cooled down as to disallow thermal excitations on the order of $k_B T$ to excite these higher energy modes [22, 23].

The spin-orbit interaction (see section 2.4) will cause the subbands to misalign, causing electrons to polarize their spins depending on their momentum [24]. This SOI is needed to gap out finite-$\vec{k}$ modes. Electrons moving with $\pm k_x$ will be able to lower their energy by aligning their spin ($\leftarrow, \rightarrow$) with their momentum. This will in turn cause the induced superconductivity (section 2.2) by the s-wave superconductor to become spin-polarized, effectively creating a p-wave superconducting phase in the nanowire. This p-wave superconductivity is needed for the Kitaev chain-model to hold, since the Hamiltonian (equation 2.1) Kitaev used assumes a spinless system. If from the perspective of the electrons, there exists only a single spin value, this will effectively create a system in which spin no longers matters, i.e. *spinless*, and this assumption of the Hamiltonian is thus satisfied.

An externally applied magnetic field is required to open up a topological gap (section 2.5). The Zeeman splitting (section 2.3) will shift the subbands, that already are misaligned in momentum due to the SOI, in energy. Looking only at the first subband for simplicity (which we can do given that the higher-order subbands are far away enough in energy), the spin-orbit split subband will develop an anti-crossing due to this magnetic field, lifting the degeneracy and separating the two subbands with opposite spin. By tuning the magnetic field, the system can be tuned from a trivial phase into the topological phase. Because of the requirement for the external magnetic field, a semiconducting material with large g-factor is desired, as this would enhance the effect of an applied external magnetic field on the Zeeman energy splitting of the spin-degenerate subbands, achieving an equivalent splitting at lower fields compared to materials with lower g-factor. The requirement for using lower fields stems from the requirement of having superconductivity, as the superconducting gap will close when the critical value B_c for the magnetic field is reached.

When all these ingredients are combined, the transition point between the trivial and topological phase is where Majoranas are predicted to appear [20, 21]. Because Majoranas always come in pairs, there will be always two Majorana sites in our system.

2.2. Superconductivity

Induced superconductivity plays as crucial role for the creation of Majorana bound states and was first observed as a drop of the electrical resistance to zero as temperature is decreased below a certain critical temperature, T_c. The first material where this phenomenon has been observed was mercury by Kamerlingh Onnes in 1911 [25] during his experiments with liquid helium. Since then, many other materials have been found to show superconductivity, both pure metals as well as compound materials [26]. Many phenomena, such as the Meissner effect, where a superconductor will expell all magnetic fields due to minimization of its free energy according to $\nabla^2\mathbf{H} = \lambda^{-2}\mathbf{H}$, were subsequently discovered pertaining to superconductors which are not simply explainable by a normal conductor with zero resistance: something more mysterious was going on. Bardeen, Cooper and Schrieffer came up with what is now called BCS-theory [27] to explain what was going on in superconductors, and this theory will be covered in subsection 2.2.1. The changes suggested by Dynes to the BCS density of states (DOS) to account for quasiparticle broadening of the superconducting gap will be discussed in subsection 2.2.3.

2.2.1. BCS theory

Superconductivity finds its roots in the interaction between electrons. Normally, two electrons, having the same electrical charge $-e$, will repel one another via the Coulomb interaction. It turns out, as will be discussed soon, that superconductivity requires an attractive force between the electrons. How would two particles that normally repel each other, attract? The Coulomb interaction between two electrons in solid-state systems is screened by the positively charged ion cores of the atoms making up the material, in particular metals. This reduces, but not eliminates, the repulsive Coulomb force between the electrons. Another effect that occurs in such a system is the attraction between the ion cores and the electrons. This will deform the crystal lattice, creating a slightly positively charged area around the electron. This positively charged area will then on its turn attract another electron that happens to pass by, mediating an attractive force between the electrons. In particular, two electrons with opposite momentum, $\vec{k}$ and $-\vec{k}$, and opposite spin, $\uparrow$ and $\downarrow$, will form what is called a Cooper pair. At room temperature (300 K) the thermal vibrations of the lattice (due to phonons) are too energetic and chaotic for these tiny deformations to give rise to any coherent attractive coupling between electrons. At low temperatures however the lattice vibrations due to temperature will be suppressed and the electron-ion interaction becomes dominant, causing some metals to become superconducting below their critical temperature T_c. The coupling described here, between electrons of opposite momenta and spin, is what happens in an *s-wave* superconductor, such as aluminium. There exist other types of coupling however, for example between opposite momenta, but equal spin, which happens in a *p-wave* superconductor.

This energy of such a system can be more quantitatively treated by considering the BCS Hamiltonian under mean-field approximation [26]:

$$\mathscr{H}_{\text{BCS}} = \sum_k k\xi_k\left(c_{k\uparrow}^\dagger c_{k\uparrow} + c_{k\downarrow}^\dagger c_{k\downarrow}\right) + \Delta\left(c_{k\uparrow}^\dagger c_{-k\downarrow}^\dagger + c_{-k\downarrow}c_{k\uparrow}\right) \tag{2.10}$$

where $\xi_k = (\hbar^2k^2/2m) - \mu$ is the energy of an electron in state k with μ being the chemical potential and Δ is the superconducting order parameter. This expression can be simplified by means of the Bogoliubov-Valentin transformation given by

$$\begin{aligned} c_{k\uparrow} &= \quad u_k^\dagger\gamma_{k0} + v_k\gamma_{k1}^\dagger \\ c_{-k\downarrow}^\dagger &= -v_k^\dagger\gamma_{k0} + u_k\gamma_{k1}^\dagger \end{aligned} \tag{2.11}$$

where the coefficients satisfy $|u_k|^2 + |v_k|^2 = 1$. Here, γ_{ki} represent the new fermionic operators under this transformation[2]. The substitution of this equation in the Hamiltonian 2.10 will yield an expression that can be diagonalised if it only contains terms proportional the new occupation number $\gamma_k^\dagger\gamma_k$ and constant terms. The new Hamiltonian can thus be split into two parts: one part which contains undesirable terms, and a second part already in terms of the new occupation numbers. To get rid of the undesirable terms preventing us from diagonalising this new Hamiltonian, the following condition

$$2\xi_k u_k v_k + \Delta_k^\dagger v_k^2 - \Delta_k u_k^2 = 0 \tag{2.12}$$

must be met. This condition can be simplified to

$$\frac{v_k}{u_k}\Delta = E_k - \xi_k \tag{2.13}$$

[2]Not to be confused with the Majorana operators discussed before.

for $E_k = \sqrt{\xi_k^2 + |\Delta_k|^2}$. Solving this expression for the coefficients yields

$$|v_k|^2 = 1 - |u_k|^2 = \frac{1}{2}\left(1 - \frac{\xi_k}{E_k}\right) \tag{2.14}$$

resulting in the new Hamiltonian

$$\mathscr{H}_{\mathrm{BCS}} = \sum_k E_k\left(\gamma_{k0}^\dagger \gamma_{k0} + \gamma_{k1}^\dagger \gamma_{k1}\right) + \sum_k \left(\xi_k - E_k\right) \tag{2.15}$$

From this it can be seen that the groundstate of this Hamiltonian has no quasiparticle excitations (also called *bogoliubons*) and that even when $\xi_k = 0$ the groundstate has an energy cost associated with quasiparticle excitations of $E_k = |\Delta|$. This shows us that quasiparticle states created by the Bogoliubov operators $\gamma_k^\dagger$ must have an energy exceeding the gap energy $|\Delta|$.

The superconducting groundstate thus consists solely of a Cooper pair condensate sitting at zero energy, while any quasiparticle excitation would require at least an energy $|\Delta|$. The density of states can be calculated by noting that there exists a one-to-one correspondence between the quasiparticle operators $\gamma_k^\dagger$ and the fermion operators $c_k^\dagger$, which allows the calculation of the density of states (DOS) via

$$N_s(E)\,\mathrm{d}E = N_n(\xi)\,\mathrm{d}\xi \tag{2.16}$$

where N_s and N_n are the superconducting and normal metal DOS, respectively. Assuming that the DOS of the normal metal close to the Fermi level is constant, that is $N_n(\xi) = N(0)$, the density of states of the superconductor is

$$\frac{N_s(E)}{N(0)} = \frac{\mathrm{d}\xi}{\mathrm{d}E} = \begin{cases} \dfrac{E}{\sqrt{E^2 - |\Delta|^2}} & (E > |\Delta|) \\ 0 & (E < |\Delta|) \end{cases} \tag{2.17}$$

Figure 2.3 shows the BCS DOS using the semiconductor model. The DOS above zero energy are reflected about the zero energy axis and the states below zero are filled with holes as to account for the particle-hole symmetry. The Fermi level E_F now lies in the middle of gap at a distance Δ away from the DOS of the excited states.

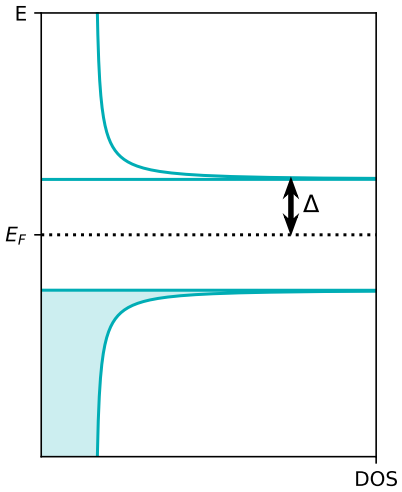

Figure 2.3: BCS density of states is the form of the semiconductor model at $T = 0$. The Fermi level E_F now lies in the middle of the gap.

2.2.2. Tunneling spectroscopy

The density of states in the superconductor can be probed by means of tunneling spectroscopy. Here, a piece of metal that is biased to a chemical potential μ_1 is brought in close (but not direct) contact with the superconductor, which has a chemical mid-gap potential of μ_2. The transport between normal metal and superconductor (N-S) is through a tunnel

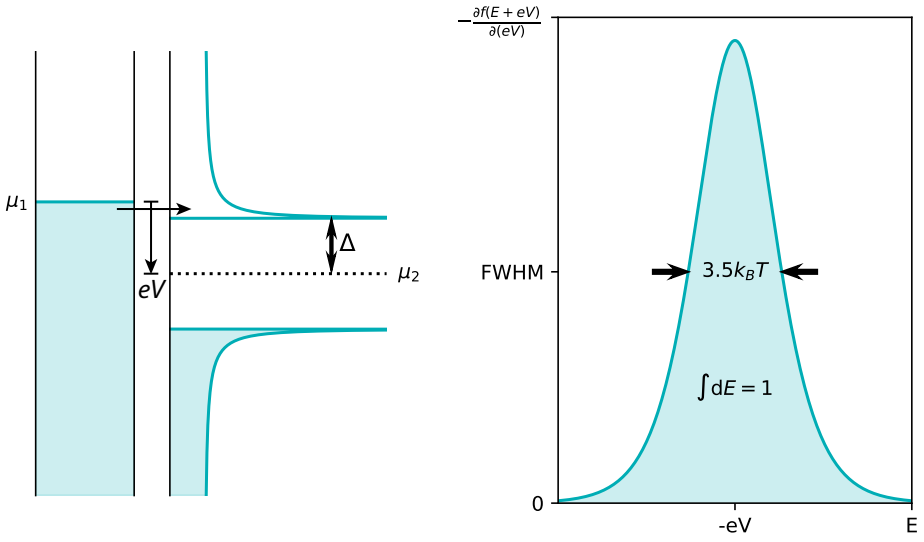

Figure 2.4: **Left:** N-S tunneling at $T = 0$. The minimal energy needed to reach a non-zero DOS in the superconductor is $eV \geqslant \Delta$. **Right:** Plot of $-\partial f(E+eV)/\partial(eV)$ which shows a Bell-shaped curve peaked around $E = -eV$ with a FWHM of $3.5k_BT$. The area under the curve is always equal to unity.

barrier. As we vary the chemical potential in our metallic lead, electrons will tunnel from the lead to the superconductor when μ_1 lines up with available states in the superconductor. The differential conductance $\mathrm{d}I/\mathrm{d}V$ will be proportional with the density of states of the superconductor, allowing us to make a scan of the DOS, see figure 2.4.

Specifically, the net current within the independent-particle approximation is given by [26]

$$I = A|T|^2 \int_{-\infty}^{\infty} N_1(E)N_2(E+eV)[f(E) - f(E+eV)]\,\mathrm{d}E \tag{2.18}$$

where eV is the applied bias in chemical potential with respect to the superconductor, A is a constant, T is the tunneling amplitude, $N_i(E)$ are the density of states of the superconducting and normal leads. $f(E)$ is the Fermi-Dirac distribution. For normal metal-to-metal (N-N) transport, this expression reduces to

$$\begin{aligned} I &= A|T|^2 N_1(0)N_2(0) \int_{-\infty}^{\infty} [f(E) - f(E+eV)]\,\mathrm{d}E \\ &= A|T|^2 N_1(0)N_2(0)eV = G_{nn}V \end{aligned} \tag{2.19}$$

which is an Ohmic result: the current develops linearly as the product of conductance and voltage. In the case of N-S tunneling, we can set $N_1(E) = N_1(0)$ in equation 2.18 as before by assuming normal metal DOS is constant near the Fermi level and setting $N_2(E+eV) = N_{2s}(E)$ for the superconductor DOS, resulting in

$$I_{ns} = A|T|^2 N_1(0) \int_{-\infty}^{\infty} N_{2s}(E)[f(E) - f(E+eV)]\,\mathrm{d}E \tag{2.20}$$

We can see that the term preceding the integral can be replaced by the result obtained for N-N via

$$A|T|^2 N_1(0) = \frac{G_{nn}}{eN_2(0)} \tag{2.21}$$

which leads to

$$I_{ns} = \frac{G_{nn}}{e} \int_{-\infty}^{\infty} \frac{N_{2s}(E)}{N_2(0)}[f(E) - f(E+eV)]\,\mathrm{d}E \tag{2.22}$$

From this result, the conductance G_{ns} can be readily derived by taking the derivative to the voltage as follows

$$G_{ns} = \frac{\mathrm{d}I_{ns}}{\mathrm{d}V} = G_{nn} \int_{-\infty}^{\infty} \frac{N_{2s}(E)}{N_2(0)} \left[-\frac{\partial f(E+eV)}{\partial(eV)}\right] \mathrm{d}E \tag{2.23}$$

This result can be further simplified by noting that the term $-\partial f(E+eV)/\partial(eV)$ is a Bell-like curve with unit area, which becomes a zero-width peak around $E=-eV$ in the low-temperature limit $k_BT \to 0$, that is

$$\lim_{k_BT\to 0}\left[-\frac{\partial f(E+eV)}{\partial(eV)}\right] = \delta(E+eV) \tag{2.24}$$

At very low temperatures then, we can approximate the integral by evaluating it at $T=0$ to obtain

$$G_{ns}\Big|_{T=0} = \frac{\mathrm{d}I_{ns}}{\mathrm{d}V}\Big|_{T=0} = G_{nn}\int_{-\infty}^{\infty}\frac{N_{2s}(E)}{N_2(0)}\delta(E+eV)\,\mathrm{d}E = G_{nn}\frac{N_{2s}(e|V|)}{N_2(0)} \tag{2.25}$$

which is exactly the normal state conductance G_{nn} multiplied by the BCS DOS! This shows that we can use tunnel spectroscopy to directly probe the BCS DOS inside the superconductor as long as we are in a low-temperature regime. This technique will be used later in this work to look at the superconducting gap of thin film aluminium. Keep in mind however that we do work at finite non-zero temperatures, which means there will be a thermal averaging window equal to $3.5k_BT$. If our temperature however is low enough to keep this window small compared to the superconducting gap $|\Delta|$ around which we wish to probe the DOS, then this is not an issue.

2.2.3. Quasiparticle broadening

A hallmark feature of Majorana bound states is that they reside at zero bias inside the gap. This protects these states from decoherence thanks to the superconducting gap Δ, preventing quasiparticles from existing inside the gap. In real world tunnel spectroscopy of the superconducting gap however it can be observed that there remains a finite quasiparticle spectrum inside the gap. To account for this, one possible explanation was given by Dynes [28]. He suggested transforming the BCS DOS via

$$E \to E - i\Gamma \tag{2.26}$$

giving the energy a complex component Γ representing the quasiparticle lifetime broadening. The Dynes DOS is then expressed as

$$\frac{N_D(E,\Gamma)}{N(0)} = \left|\mathrm{Re}\frac{E-i\Gamma}{\left[(E-i\Gamma)^2-\Delta^2\right]^{1/2}}\right| \tag{2.27}$$

If the quasiparticle lifetime broadening parameter Γ is negligible the Dynes DOS will revert back to the BCS DOS. Increasing Γ will increase the quasiparticle lifetime and smoothen the gap. Whereas the BCS DOS has a diverging DOS at the gap edge, the Dynes DOS does not diverge there if $\Gamma \neq 0$.

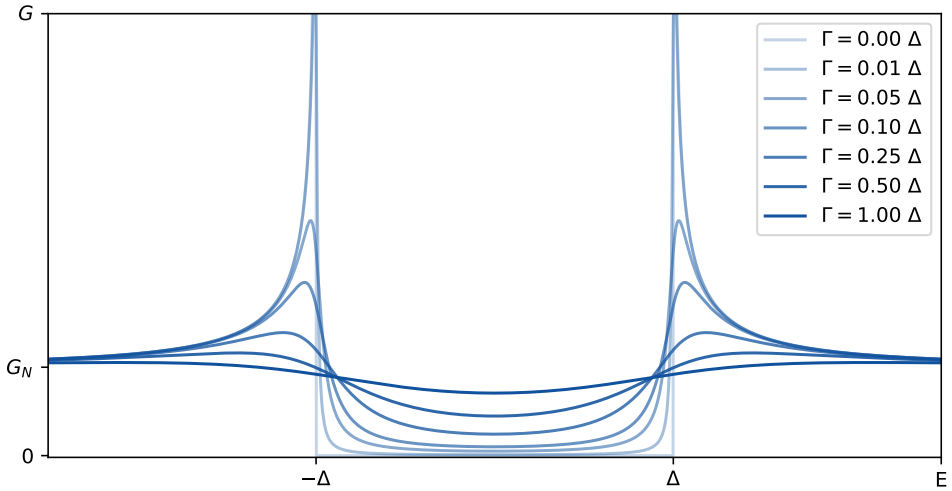

Figure 2.5: Dynes DOS for varying Γ in units of conductance. Plotted here for $-500\mu eV \leqslant E \leqslant 500\mu eV$ and $\Delta = 200\mu eV$. G_N is the out-of-gap conductance.

Figure 2.5 shows the Dynes DOS for several values of Γ in units of Δ. From this figure the effect of the quasiparticle lifetime broadening term Γ becomes apparent. The divergence of the DOS at the gap edge is smoothened out and there

now exists for $\Gamma \neq 0$ a finite non-zero quasiparticle DOS inside the gap. There can be many sources causing broadening of the gap, such as temperature broadening or surface inhomogeneities [29]. The Dynes model tries to incorporate all these sources of broadening in a single parameter and as such is too simple to conclusively say whether there is a hard or a soft gap. It is therefore mostly useful for obtaining a rough idea of the broadening compared to the BCS DOS.

2.3. Zeeman effect

Electrons are spin-1/2 particles and can have one of two spins: up $\uparrow$ or down $\downarrow$. Their spin acts as a magnetic moment and will make them react to magnetic fields. Normally, under no external magnetic field, the electrons from a single subband are spin-degenerate. Spin can be regarded as an magnetic moment which can react to a magnetic field. Consider a spin-degenerate subband, see figure 2.6a for two subbands, one shown in blue with its lowest energy at E_1, the other in red at E_2. The spin states of the electons in both subbands are shown as arrows. When we now apply an external magnetic field, the spin that is aligned with the field direction will have a lower energy compared to the spin direction opposing the field. This will lead to a spin splitting of the subbands as shown in figure 2.6c.

The Hamiltonian of the Zeeman interaction is given by [24]:

$$\mathscr{H}_Z = -\vec{\mu} \cdot \vec{B} = \frac{1}{2} g \mu_B \vec{\sigma} \cdot \vec{B} \tag{2.28}$$

where $\vec{\mu}$ is the dipole moment of the electron, $\vec{B}$ the magnetic field, g the Landé g-factor, μ_B the Bohr magneton and $\vec{\sigma}$ is the vector of Pauli matrices. For an arbitrary magnetic field

$$\vec{B} = B_0 \begin{pmatrix} \sin\theta \cos\phi \\ \sin\theta \sin\phi \\ \cos\phi \end{pmatrix} \tag{2.29}$$

with $\theta \in [0, \pi]$ and $\phi \in [0, 2\pi)$, the eigenvalues of this Hamiltonian are

$$\pm E_Z = \pm \frac{1}{2} g \mu_B B_0 \tag{2.30}$$

with E_Z being the Zeeman energy. The energy difference between the spin-up and spin-down states is then

$$E_{\uparrow\downarrow} = g \mu_B B_0 \tag{2.31}$$

which is the energy between the spin-split subbands shown in figure 2.6c (blue-lightblue, or red-orange).

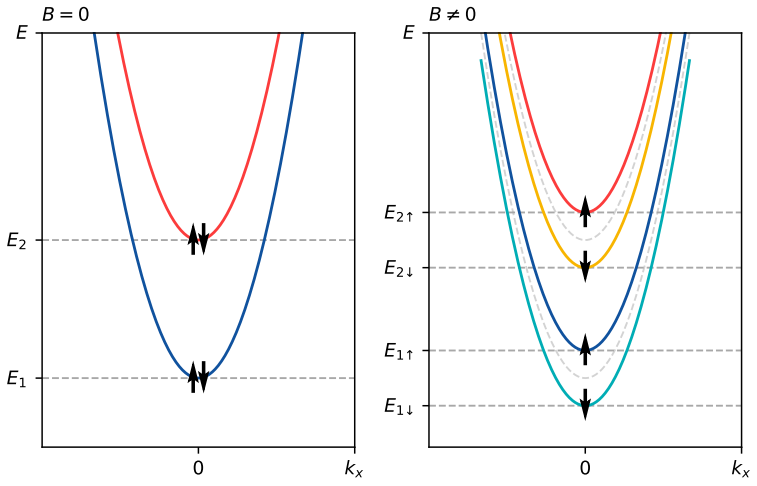

(a) (b)

Figure 2.6: Illustration of the Zeeman effect on spin-degenerate subbands. A non-zero magnetic field B will cause the spin-degenerate subbands to split. The Zeeman-energy is given by $E_{Z,i} = |E_{i,\uparrow} - E_{i,\downarrow}| = |g_i| \mu_B B$.

2.4. Rashba spin-orbit interaction

Spin-orbit interaction (SOI) is the phenomenon where the spin of a particle couples to its momentum $\vec{k}$. Its effects are needed for nanowire Majorana bound states to create two subbands that are shifted with respect of one another in momentum space. This is caused by an effective spin-orbit magnetic field due to relativistic effects in the frame of the electron as it moves in the electric field of the atoms in crystal lattice [30, 31]

$$\vec{B} = -\frac{1}{c^2}\vec{v} \times \vec{E} \tag{2.32}$$

A non-relativistic approximation of the Dirac equation can be used to derive the shift in energy because of this spin-orbit field as [32]

$$\mathscr{H}_{\mathrm{SO}} = -\frac{\hbar}{4m_0^2c^2}\vec{\sigma} \cdot \vec{p} \times \left(\nabla V_0\right) \tag{2.33}$$

Here m_0 is the rest mass of the electron, c the speed of light in vacuum, $\vec{\sigma}$ is the vector of Pauli spin matrices, $\vec{p}$ the momentum and V_0 is the electric potential. For the purposes of this work, only Rashba SOI will be considered. In our nanowire case then for electrons with momentum k_x the effective Rashba spin-orbit Hamiltonian is

$$\mathscr{H}_{\mathrm{R}} = -\alpha_R k_x \sigma_y \tag{2.34}$$

with an induced spin-orbit field

$$\vec{B}_{SO} \propto \alpha_R\left(\vec{k} \times \vec{E}\right) \tag{2.35}$$

which is perpendicular to both the electron momentum and the electric field of the lattice. This coupling between spin and momentum causes, similar to the Zeeman effect, a splitting between subbands. However, whereas the Zeeman effect shifts the subbands in the dispersion plots up or down in energy, Rashba SOI will also shift the subbands in momentum, as can be seen in figure 2.7 left. Here, the splitting between the subbands is shown and from this it can be seen that the spin-orbit splitting scales linearly with momentum. The energy of the Rashba split subbands is lowered by $-E_{\mathrm{SO}}$ and the split subbands now have their minima moved to $k_{\mathrm{SO}} = \pm m\alpha_R/\hbar^2$.

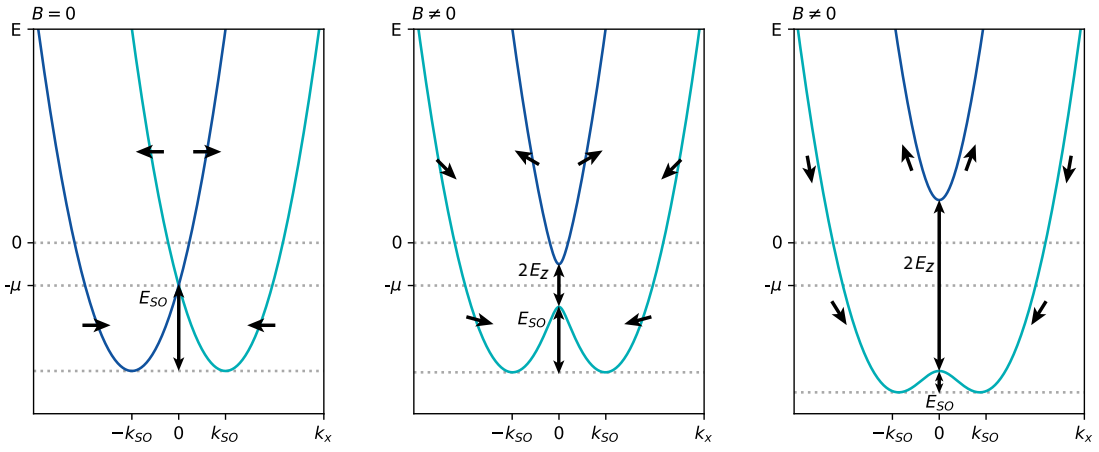

Figure 2.7: Single subband split by spin-orbit interaction. **Left:** The spin of the electrons is aligned with the momentum, leading to a misalignment between the two spin polarizations. Here, $B = 0$, so no Zeeman splitting occurs. **Middle:** Now the magnetic field is turned on. The bands split at what was before the energy degeneracy point located at $-\mu$. Here it is shown for the case $E_{\mathrm{SO}} > 2E_Z$. **Right:** Now, the magnetic field is increased even further. The Zeeman energy $2E_Z$ overtakes the spin-orbit energy E_{SO}. If the Zeeman energy would be increased even further, the spin-orbit energy would become negligible and the lightblue subband would assume an almost parabolic shape.

2.5. Topological gap

When an externally applied magnetic field B is oriented along a nanowire in the x-direction, which is also the direction of the electron momentum k_x, with strong Rashba spin-orbit coupling strength α_R, the Hamiltonian of this system is given by [13]

$$\mathscr{H}_0 = \frac{\hbar^2 k_x^2}{2m} - \mu - \alpha_R k_x \sigma_y + \frac{1}{2} g \mu_B B \sigma_x \tag{2.36}$$

where $\sigma_{x,y}$ are Pauli matrices. This Hamiltonian combines all previously discussed effects, except for induced superconductivity. The eigenvalues of this Hamiltonian are

$$E = \frac{\hbar^2 k_x^2}{2m} - \mu \pm \sqrt{\alpha_R^2 k_x^2 + E_Z^2} \tag{2.37}$$

and are plotted in figure 2.7. When the Zeeman field is turned off, the Hamiltonian reverts back to the Rashba SOI-only case, and thus the left graph in this figure corresponds to this case also. As was mentioned in section 2.1.1, we need to induce a same-spin pairing p-wave superconducting phase in our nanowires. If we can change or manipulate the band structure such that $-\mu$ lies *within* a gap, then only states with a single spin polarization are available for Cooper pairs. In the middle graph, the Zeeman field is turned on. The Zeeman splitting will lift the degeneracy around $-\mu$ and creates an anti-crossing. This will cause the upper band (in darkblue) to become dis-populated and effectively cause a spin selection to take place, causing only states in the lower (lightblue) band to be populated. In this case $2E_Z < E_{\mathrm{SO}}$. Increasing the Zeeman field even further such that $E_Z > \mu$ can be seen in the right graph. Note also that $2E_Z \gg E_{\mathrm{SO}}$, suppressing the SOI energy. The gap that has been opened up is called the *helical gap* [33–35]. Increasing the Zeeman field even further will cause the spin-orbit energy to become negligible in comparison, causing the lightblue band to assume an almost parabolic shape.

Now the time has come to switch on superconductivity. We can use the proximity effect [19, 36] and an s-wave superconductor to induce superconductivity in the nanowire. The Hamiltonian describing s-wave pairing is given by

$$\mathscr{H}_{\mathrm{SC}} = \int_{-\infty}^{\infty} \left[e^{i\phi} \Delta \, \psi_\uparrow(x) \, \psi_\downarrow(x) + \mathrm{h.c.} \right] \mathrm{d}x \tag{2.38}$$

where ϕ is the phase of the superconducting order parameter. Here, Δ refers to the induced gap parameter which does not necessarily equal the bulk gap parameter of the intrinsic superconductor, and $\psi_{\{\uparrow,\downarrow\}}(x)$ are the field operators. Adding this Hamiltonian to the nanowire Hamiltonian yields [37, 38]

$$\mathscr{H} = \mathscr{H}_0 + \mathscr{H}_{\mathrm{SC}} = \int_{-\infty}^{\infty} \left[\vec{\psi}_x^\dagger \left(\frac{\hbar^2 k_x^2}{2m} - \mu - \alpha_R k_x \sigma_y + \frac{1}{2} g \mu_B B \sigma_x \right) \vec{\psi}_x + e^{i\phi} \Delta \, \psi_\uparrow \, \psi_\downarrow + h.c. \right] \mathrm{d}x \tag{2.39}$$

The analytic expression for the eigenenergies of this Hamiltonian is quite complex. However, at $k_x = 0$ the expression for the size of the gap simplifies to

$$E_{\mathrm{gap},k_0} = \sqrt{\Delta^2 + \mu^2} - E_Z \tag{2.40}$$

As shall be demonstrated shortly for a numerical solution to the Hamiltonian, there are two locations in the dispersion where the gap size is at a minimum but $k_x \neq 0$. This is at $k_f = 2k_{\mathrm{SO}}$. If $\mu = 0$ is assumed, another simplification can be made and the gap size at k_f can then be expressed as

$$E_{\mathrm{gap},k_f} = \frac{2\Delta E_{\mathrm{SO}}}{\sqrt{E_{\mathrm{SO}} \left(2E_{\mathrm{SO}} + \sqrt{E_Z^2 + 4E_{\mathrm{SO}}^2} \right)}} \tag{2.41}$$

We can also use the Hamiltonian in Bogoliubov-de Gennes formalism to solve for the eigenenergies numerically. The BdG Hamiltonian is given by [38]

$$\begin{aligned} \mathscr{H}_{\mathrm{BdG}} &= \begin{pmatrix} \mathscr{H}_0 & \Delta \\ \Delta^* & -\mathscr{T}\mathscr{H}_0\mathscr{T}^{-1} \end{pmatrix} & \Delta &= \begin{pmatrix} 0 & e^{i\phi}\Delta \\ -e^{i\phi}\Delta & 0 \end{pmatrix} \\ \mathscr{H}_0 &= \begin{pmatrix} \frac{\hbar^2 k_x^2}{2m} - \mu & E_Z + i\alpha_R k_x \\ E_Z - i\alpha_R k_x & \frac{\hbar^2 k_x^2}{2m} - \mu \end{pmatrix} & -\mathscr{T}\mathscr{H}_0\mathscr{T}^{-1} &= -\mathscr{H}_0 \end{aligned} \tag{2.42}$$

where $\mathscr{T}$ is the time-reversal operator. The result of finding the eigenenergies for various values of E_Z in units of Δ can be seen in figure 2.8. A few important observations can be made from this figure. Firstly, at $E_Z = 0$ there is yet no Zeeman splitting between the darkblue and lightblue subbands and there exists a gap around the Fermi level. This gap corresponds to the normal s-wave superconductivity that is induced via the proximity effect shown in figure 2.8a. As the Zeeman field increases in strength as is shown in figure 2.8b, the gap will begin the close and the two subbands will move away from eachother. There is now predominantly s-wave pairing and a small amount of p-wave pairing. Then, when $E_Z = \sqrt{\Delta^2 + \mu^2}$, the gap will close and the energy will be degenerate at $k_x = 0$, as shown in figure 2.8c

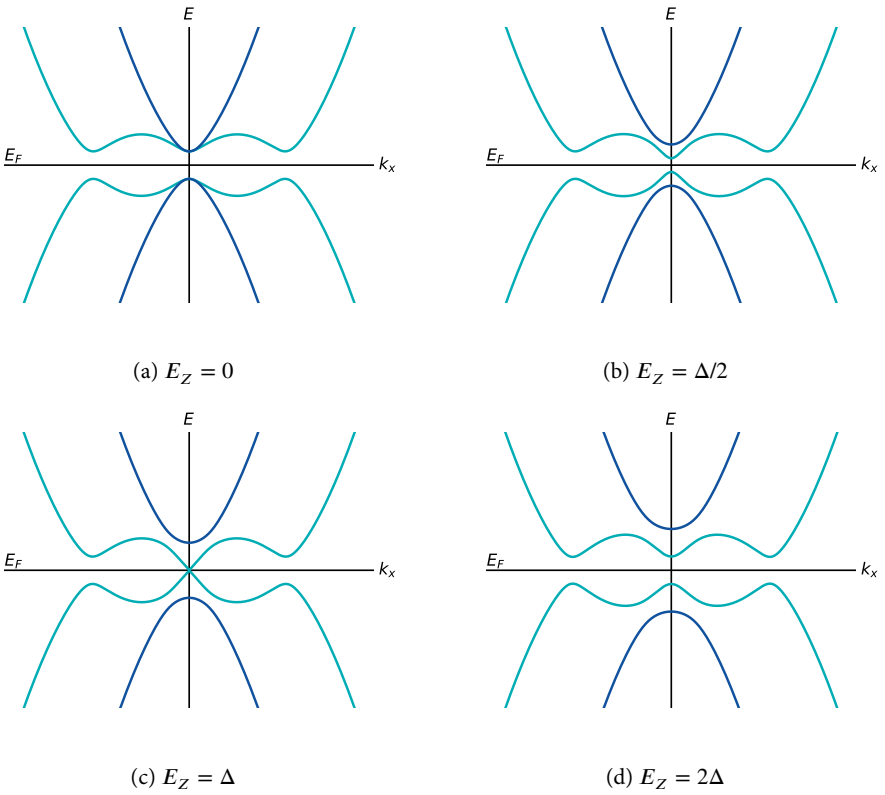

(a) $E_Z = 0$ (b) $E_Z = \Delta/2$

(c) $E_Z = \Delta$ (d) $E_Z = 2\Delta$

Figure 2.8: Numerical solutions to the eigenenergies of the Hamiltonian of equation 2.42. For these plots, $\mu = 0$, $\hbar = m = 1$, $\alpha_R = 2$ and $\Delta = (\alpha_R/2)^2$. **(a)** $E_Z = 0$. No Zeeman splitting occurs. The system has a trivial gap about the Fermi level. Two minima around $k_x = \pm 2k_{\mathrm{SO}}$ can also been seen. **(b)** $0 < E_Z < \Delta$. The trivial gap begins to close. **(c)** $E_Z = \Delta$. The gap is now closed. This is the point of the topological transition. Majoranas are predicted to appear in this regime. **(d)** $E_Z > \Delta$. The trivial gap has closed and reopened. The gap is now a topological gap with the energy of the topological bandgap at $k_x = 0$ given by $2\Delta_{\mathrm{TOPO}}$.

for the case $\mu = 0$. There is now as much s-wave as p-wave pairing. If the field is increased even further, the gap will reopen. This reopened gap is called the *topological gap* (figure 2.8d) and our system is now in the topological regime. Pairing is predominantly p-wave. Majoranas are predicted to appear exactly at the location where the gap closes. In our nanowire model, there will always be a transition between the normal and the topological regime at the ends of the nanowire-superconductor mutual regime and thus Majoranas will appear there.

2.6. Classical transport

2.6.1. Field-effect mobility

To have some gauge as to how well our nanowires perform compared to other growth methods, field-effect mobility (FEM) can be used to characterize the material. This method is commonly used for VLS-grown nanowires since more complicated structures such as Hall bars, discussed in section 2.6.2, are often not available. Other reasons why transconductance measurements prove to be difficult is the uncertainty of the gate capacitance and universal conductance fluctuations, making accurate measurement of the mobility difficult, as was argued by [39]. To determine the FEM then, a model where the nanowire is taken as a field-effect transistor (FET) is therefore suggested. The conductance as function of gate voltage is [40]

$$G(V_g) = \left(R_s + \frac{L^2}{\mu C (V_g - V_{th})} \right)^{-1} \tag{2.43}$$

with R_s being the equivalent resistance in series with the nanowire, μC the product of mobility and total capacitance of the device, L the length of the nanowire, V_g the gate voltage and the threshold voltage V_{th} determining the transition between the wire being in pinch-off or conducting.

To give some idea as to what these conductance pinch-off traces look like, several traces for $G(V_g)$ are shown in figure 2.9 for a variety of gate voltages. Note that all traces are bound by the saturation conduction value $G_{sat} \approx 1/R_s$, since the series resistance will dominate when the nanowire FET resistance drops to negligible values as it is being pinched-on.

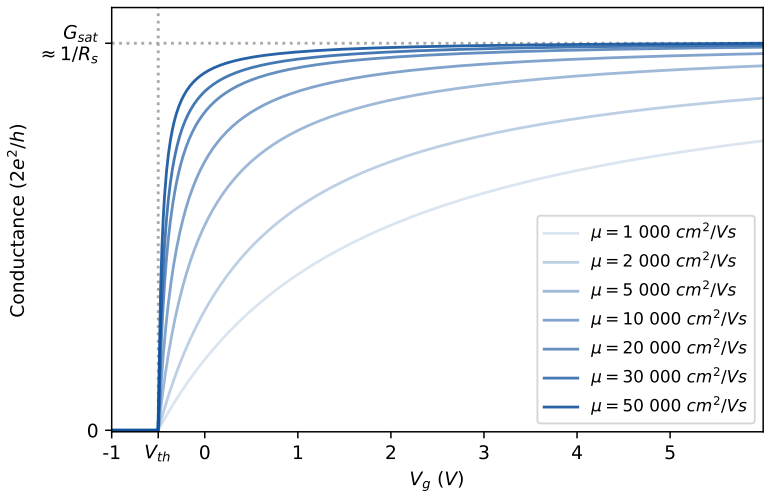

Figure 2.9: Pinch-off curves for several FEM mobilities plotted from theory. Threshold voltage set at slightly below 0 V as indicated by the vertical dotted line. Saturation conductance for all curves shown as the horizontal dotted line. For these curves, $C = 0.5$ fF, $L = 150\ \mu m$, $R_s = 20$ kΩ.

2.6.2. Hall mobility

When an external magnetic field is applied perpendicularly to a Hall bar, a voltage will develop across it. This is called the Hall effect [41]. If also the voltage developing between the two adjacent legs is measured at same time as the Hall voltage is measured, then this measurement is called a 4-point measurement of the Hall bar. An example of a Hall bar with which a 4-point measurement can be done is shown in figure 2.10. Also refer to figure 6.5 for an SEM image with the measurement setup and related geometric quantities inlaid. Let a magnetic field with field strength B_z be applied perpendicularly to the Hall bar and let the Hall bar be current biased with a current I_x. The Hall voltage V_H that develops will be

$$V_H = \frac{I_x B_z}{nte} \tag{2.44}$$

where n is the electron density, t the thickness of the sample and e the electron charge. From this the Hall resistance R_H can be extracted as

$$R_H = \frac{V_H}{I_x} = B_z \frac{1}{nte} \tag{2.45}$$

From the definition of conductivity

$$\sigma = ne\mu \tag{2.46}$$

where μ is the mobility, it can be seen that

$$\mu = \frac{\sigma}{ne} = \sigma t \frac{1}{nte} \tag{2.47}$$

Now, the product σt is called the sheet conductance and can be obtained from the intrinsic resistance R_{xx} between two legs on the same side of the Hall bar and geometric quantities as

$$\sigma t = \frac{L_{xx}}{R_{xx} W} \tag{2.48}$$

where L_{xx} is the distance between the legs and W is the width of the sample. From this, the mobility μ is readily extracted as

$$\mu = \frac{L_{xx}}{R_{xx} W} \frac{1}{nte} \tag{2.49}$$

Here, the factor $1/nte$ can be obtained from fitting the expression for the Hall resistance R_H. An important aspect of this mobility is the fact that the mobility can be obtained without the need of a value for the capacitance C, in contrast to the FEM discussed above, which has to be obtained from simulations and is thus a significant source of error. Thus, in principle, the Hall mobility should yield more reliable results. One objection to using Hall mobility could be that really, the mobility is being measured only near the T-junction across which the Hall voltage is measured. If the nanowires are uniform enough however, this should not be an issue. Also, junctions in general have a higher risk of disorder. Therefore the mobility might be worse when measured in the junction compared to elsewhere in the nanowire Hall bar, giving a lower bound to the mobility.

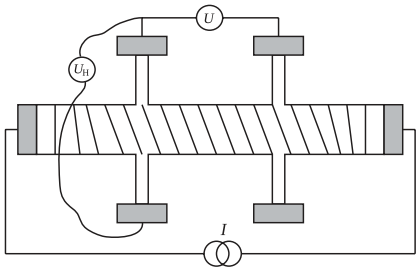

Figure 2.10: Schematic representation of a Hall bar. A current bias can be seen applied at the two Hall bar extremeties. Image from [24]

2.6.3. Coulomb blockade and quantum dots

Electrons can be restricted from movement and essentially trapped by separating a region from the bulk [42]. This can be done using two cutter gates. By tuning the chemical potential of a nanowire such that the local density of states goes to zero and the wire goes into pinchoff, a region in between the cutter gates can be separated from the bulk of the nanowire. If the barriers created by the cutter gates are large enough, electrons will be forbidden from transport through the barriers, effectively trapping them. What has now been created is called a quantum dot. Because there are a certain amount of electrons in this now separated region, the levels will be quantized. The charging energy is inversely proportional to the size of the quantum dot. The levels can be shifted with respect to the source and drain leads by changing the chemical potential in the dot using a capacitively coupled plunger gate. Transport onto a level inside the quantum dot is shown in figure 2.11. Here, the chemical potential is changed from (b) to (c) such that an energy level within the dot lines up with the leads and an electron is able to occupy the state.

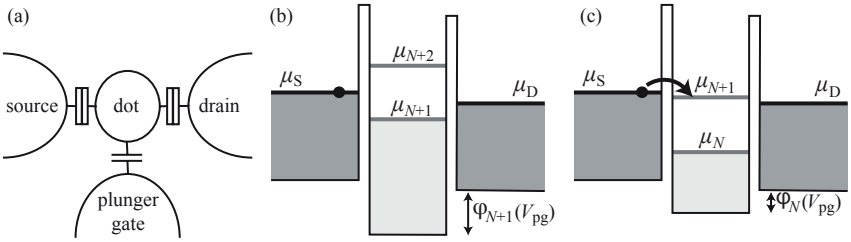

Figure 2.11: Making quantum dots using Coulomb blockade. **(a)** Schematic representation of a quantum dot created using Coulomb blockade. A dot is separated from the bulk using two cutter gates. The chemical potential is tuned by capacitive coupling of the plunger gate to the dot. A bias can be applied by tuning the source and drain leads. **(b)** Transport is prohibited due to Coulomb blockade. All available levels below μ_{N+2} are occupied and this level itself is out of reach from the perspective of the source and drain leads. **(c)** The plunger gate is tuned such that the level μ_{N+1} is aligned with the source and drain leads. Electronic transport to the level is now allowed. Figure from [24]

When a bias voltage is applied between the source and drain leads, an energy window $\Delta E = |eV_{SD}|$ opens up in which electronic transport from source to drain through the dot may take place, which is shown in figure 2.12. Here, the plunger gate can be seen to tune the chemical potential inside the dot, but for the entire range depicted in this figure, electronic transport is allowed regardless of the tuning of the level. If in the chemical potential however would have been slightly increased in (a) or slightly decreased in (c), then the level μ_N would no longer be capable of transport and once again the dot would be in Coulomb blockade.

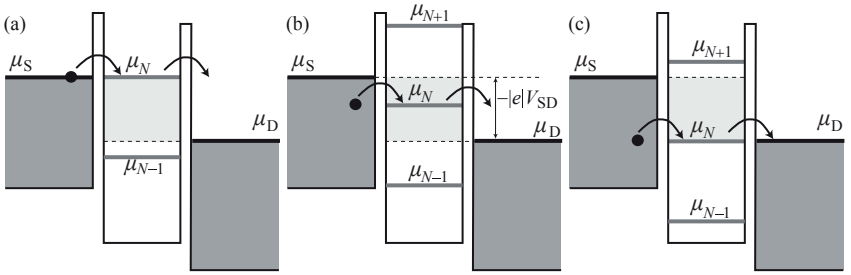

Figure 2.12: Effects of a finite non-zero bias between the the source and drain leads. **(a,b,c)** The finite bias between the source and drain leads opens up a conductance window. For a range of voltages in plunger gate space, conductance through the dot level μ_N is allowed. The energy window is proportional to the bias voltage as $\Delta E = |eV_{SD}|$. Figure from [24]

For N electrons on the dot, the electrostatic energy is given by

$$E_{\text{es}}(N) = \frac{1}{2}\frac{Q^2}{C} = \frac{e^2N^2}{2C} \tag{2.50}$$

with C the capacitance of the dot. The energy spacing of the levels is due to the Coulomb interaction between the electrons on the dot. To place an extra electron on the dot, the charging energy

$$E_c(N+1) = \frac{e^2}{2C}\left((N+1)^2 - N^2\right) = \frac{e^2}{2C}(2N+1) \approx \frac{e^2}{C}N \tag{2.51}$$

would have to be added. Here it is assumed that $N \gg 1$ such that the additional term $e^2/2C$ coming from the constant is negligible. The difference in charging energy is then

$$\Delta E_c = \frac{e^2}{C} \tag{2.52}$$

As a condition for being able to probe the levels inside the quantum dot, the available energy from the environment needs to be small, that is

$$k_B T \ll \Delta E_c \tag{2.53}$$

Otherwise, the electrons would be able to overcome the charging energy by simply absorbing thermal energy, which would make our efforts to control the occupation of the levels futile.

Coulomb diamonds arise when the conductance is measured as the plunger gate and the bias are varied. This can be understood by referring back to figures 2.11 and 2.12. First, imagine there is no bias applied and thus the energy window is zero. When the plunger gate now shifts the dot levels up, conductance is blocked for a range in plunger gate space until the next level is aligned with the reservoirs. Now, the bias is slightly increased and a small energy window opens up. The range in plunger gate space in which there is no conductance is smaller, since there will be some overlap between the energy window and the chemical potential of the reservoirs. If now the bias voltage is increased to at least the level spacing, there will always be conductance, and thus the dot will no longer go in Coulomb blockade. The regions in bias and plunger space where there is no conductance will look like diamonds, since the energy window scales linearly with the bias voltage and the window shifts linearly with the plunger gate voltage.

2.7. Quantum transport

2.7.1. Quantum point contacts

In a clean semiconductor nanowire, ballistic transport can take place if the inelastic scattering lengths is greater than the contact spacing. This ballistic transport will lead to conductance quantization in quantum point contacts (QPCs) [43, 44] according to the Landauer formula

$$G(\mu) = g_s \frac{e^2}{h} \sum_n T_n(\mu) \tag{2.54}$$

where $g_s \in \{1, 2\}$ is the spin degeneracy factor and $T_n(\mu)$ are the transmission eigenvalues, which look like smoothened unit step functions around $E = \mu$. From this it can immediately be seen that the conductance is quantized by

$$G_Q = g_s \frac{e^2}{h} \tag{2.55}$$

In this work, we will define the quantum of conductance as $G_0 = 2e^2/h$ by taking $g_s = 2$, but other works might define it based on a different value of g_s.

To understand quantized conductance through QPCs better, refer to figure 2.13. This figure shows the two plots presented in subsection 2.3, this time accompanied by plots of the conductance as function of chemical potential. For the spin-degenerate case in 2.13a,b, we have $g_s = 2$ and so as the chemical potential is tuned such that the first subband at E_1 is occupied, the conductance will jump to $G = G_0$, and to $G = 2G_0$ when the second subband is reached. Similarly for the case where the Kramers degeneracy is lifted shown in figure 2.13c,d. Here $g_s = 1$ and the conductance becomes $G = 0.5G_0$ when the chemical potential reaches the first subband at $E_{1\downarrow}$, and to $G = 1.0G_0$ for $E_{1\uparrow}$, continuing in this way in increments of $0.5G_0$.

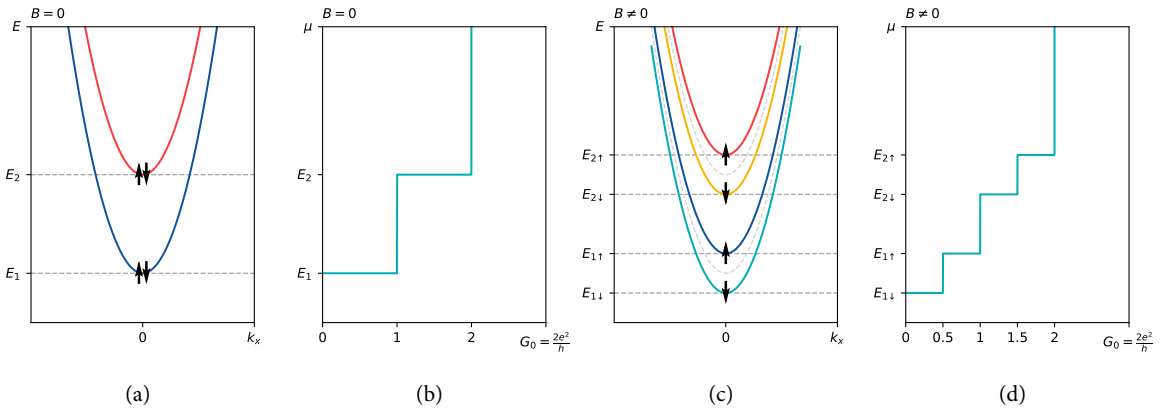

(a) (b) (c) (d)

Figure 2.13: Quantized conductance shows up as conductance steps as the chemical potential μ is aligned with the subband energies. **(a,b)** Spin degenerate subbands will show conductance steps of $G_0 = 2e^2/h$ each time the chemical potential is tuned to an additional subband energy. **(c,d)** When the subbands are Zeeman split, each subband now only contributes half a conductance quantum when μ is aligned, resulting in steps of $0.5G_0 = e^2/h$.

2.7.2. Aharonov-Bohm effect

The Aharonov-Bohm effect occurs when a particle that has a phase coherence length longer than the path length around a loop interferes with itself to form an interference pattern. In this regard, the effect is analogous to the double-slit experiment in that the wave-like behaviour of a particle creates an interference pattern. In the double-slit experiment however the interference pattern was shown on a screen and the phase difference due to the varying path lengths resulted in an interference pattern in space. In mesoscopic structures, such a screen is not available and instead we have to use electrical contacts to measure the interference pattern. To do this, we can use the fact that charged particles obtain a phase as they traverse a path through a vector potential. To understand this better, consider the case depicted in figure 2.14. Here, a magnetic field going into the plane creates a flux through the ring proportional to

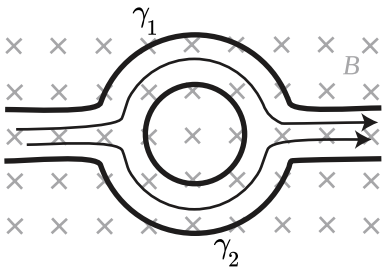

Figure 2.14: Schematic representation of an Aharonov-Bohm loop. A particle enters the loop from the left. γ_1 and γ_2 show the two paths around the loop. The particle exits the loop on the right. A magnetic field pointing into the plane is shown as well [24].

$$\phi = A(\hat{n} \cdot \vec{B}) \tag{2.56}$$

where A is the area of the ring, $\hat{n}$ is the normal vector of the area of the ring and $\vec{B}$ is the magnetic field. As the electron traverses both paths around the ring simultaneously it acquires a phase difference between the two paths. This phase difference is then responsible for the interference pattern we are interested in. If the electron wavefunction interferes constructively before it exits the path around the loop towards the right, a peak in the measured current is observed. Conversely if the wavefunction interferes destructively, a valley is observed. The phase difference can then be adjusted as to sweep through these peaks and valleys to obtain an interference pattern similarly as what would be displayed on the screen in the double-slit experiment. As we adjust the magnetic field, the flux though the area A changes and the electron acquires a phase difference between the paths according to

$$\delta(\phi) = \delta(0) - 2\pi\frac{\phi}{\phi_0} \tag{2.57}$$

where $\phi_0 = h/e$ is the flux quantum. The Aharonov-Bohm oscillations this produces will be periodic with

$$\Delta B = \frac{\phi_0}{kA}, \quad k \in \mathbb{N} \tag{2.58}$$

where k determines the order of the oscillation. This parameter is there because it is possible for the electron to traverse the loop multiple times, creating higher order interference patterns as it does so. In actual experiment, the AB-oscillations will be superimposed onto a background called the universal conductance fluctuations (UCF) [45]. This UCF is due to the freezing in of scattering centers during cooldown. The phase coherence length L_ϕ can be extracted by considering the temperature dependence of the amplitude of the magnetoconductance oscillations as

$$A_{h/e}(T) = A_0 e^{-L/L_\phi(T)} \tag{2.59}$$

where L is the path length around the loop and A_0 is a constant. For $L_\phi(T)$ a suitable model can be used. For this work, the model by [46] pertaining to topological insulator nanoribbons was used, giving a phase coherence length dependence on temperature as

$$L_\phi(T) = \frac{L}{aT^{1/2}} \tag{2.60}$$

where a is a constant of proportionality obtained from fit parameters.

3

Methods

3.1. Cryogenics

Physics at mesoscopic scales is about phenomena with energies much smaller than that of the thermal energy $k_B T$ at room temperature ($\sim$ 26 meV). This causes the effects of interest to be averaged out and thus invisible to our measurements. Therefore we require cooling down of our devices to very low temperatures. This can be achieved in several ways. Samples could submerge in a container of liquid helium, cooling it down to 4.2 K as the helium evaporates, the so called continuous-flow cryostat. One of the main disadvantages of such a cryostat however is the evaporation itself, as ^{4}He is lost to the environment. This can be mitigated by either installing a recovery line which collects the helium gas and condenses it back to liquid form at a recovery station, or by using a closed loop system such as a pulse tube cryostat (cooling to approximately 4 K) or dilution cryostat (20 mK), both of which have been used in this work and will be discussed below.

3.1.1. Pulse tube cryostats

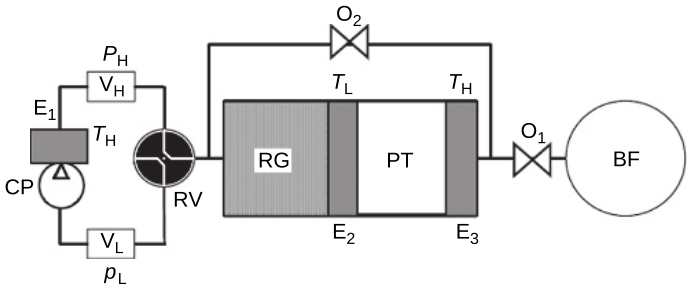

Figure 3.1: Schematic representation of a GM-type pulse tube cryostat. [47]

The Stirling type pulse tube cryostat consists of a long tube filled with a gas, usually ^{4}He, with one end connected to a piston and the other end closed. The piston compresses the gas such that it is forced though a series of heat exchangers and a regenerator. In the case of the more modern GM[1]-type (shown in figure 3.1), the moving piston is replaced by a compressor and a rotary valve. Rotating the rotary valve one way connects the tube to the high pressure end of the compressor, while rotating it the other way connects it to the low pressure end, eliminating the need for a piston and reducing the vibrations imposed on the cryostat. The workings however are the same in both cases. The cooling power is derived from the compression and expansion of the gas inside the pulse tube. This can be understood by following a gas pocket initially located just after the rotary valve (RV). When the RV connects the high pressure side of the compressor (CP) to the regenerator (RG), the gas pocket is compressed while the orifice (O_1) is closed, meaning the gas pocket is now both high pressure and high temperature due to the compression. The walls of the tube can be considered perfect isolators. Now, O_1 is opened and the compressed gas pocket is allowed to flow into the buffer volume BF. The RG is made of a material with high thermal capacity, meaning that the gas pocket will pay energy to the RG material until their temperatures equilibriate. After the RG the gas pocket is now high pressure, but low temperature. The RV is now

[1] Named after Gifford and McMahon (1960) [48]

switched to connect the tube to the low pressure side of the CP while O_1 is closed again. This will decrease the pressure in the tube to the low pressure at the inlet of the CP, causing the gas to expand and to cool down even further, below the temperature T_L. O_1 is opened again and the gas pocket now passes through the heat exchanger E_2 once more. The difference in temperature between the gas and the heat exchanger constitutes the cooling power, as the gas pocket will take up heat energy from it and cools it.

From figure 3.1 it can be seen that the place where the cooling power is generated is in the middle of the tube. For this reason, many pulse tube cryostats will have two tubes connected to a cold head, one for the leftmost part of the "whole" tube, and the other for the rightmost part. The cold head then delivers the cooling power to a sample located inside a vacuum chamber via direct contact conduction.

The pulse tube cryostat used in this work is a "Dry Ice" 4K Benchtop model by ICEoxford Cryogenics.

3.1.2. Dilution cryostat

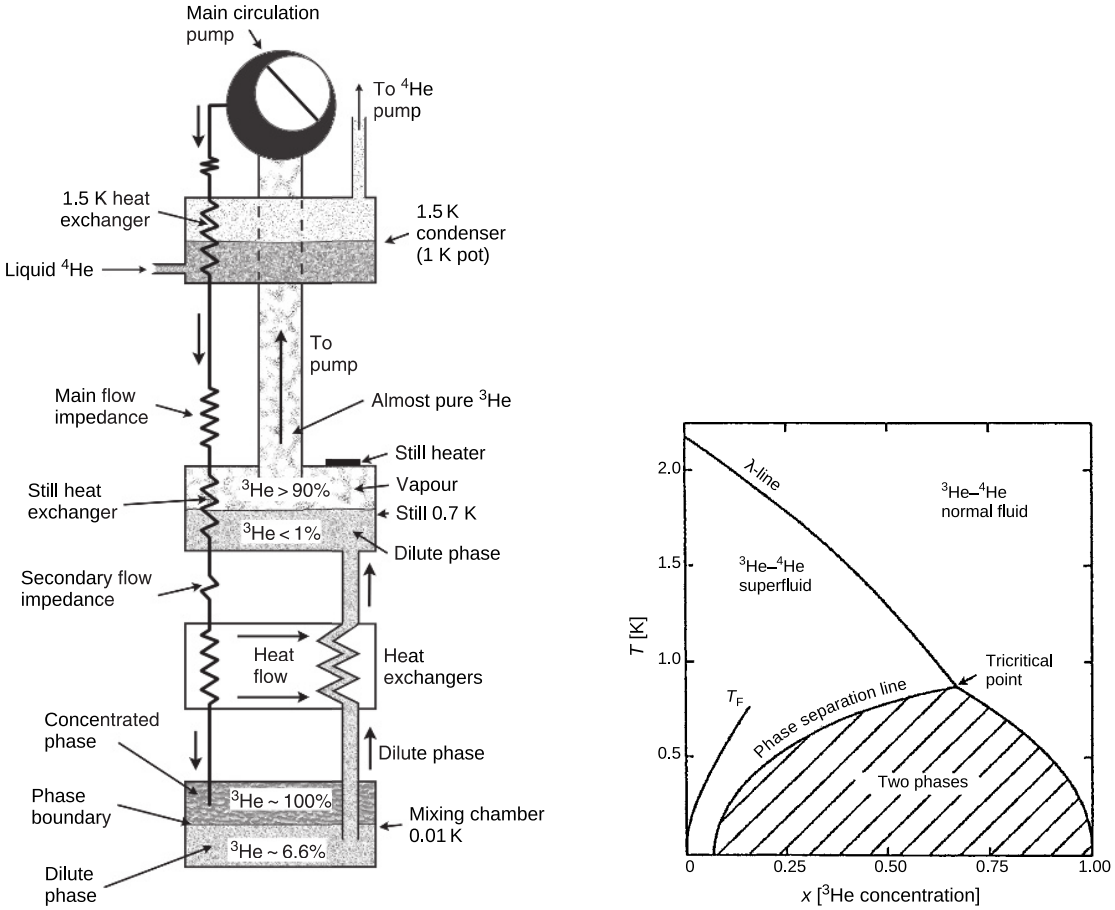

Figure 3.2: **(a)** Schematic representation of a dilution cryostat. [47]; **(b)** Phase diagram of ^{3}He–^{4}He mixture. [49]

To reach temperatures much lower than that of the pulse tube cryostat, we need to use another type, the dilution cryostat. This type of cryostat can reach temperatures of several millikelvin. To understand how this cryostat works, let us look at the mixing chamber in figure 3.2a. At temperatures below the tricritical point at 0.867 K (see figure 3.2b) the mixture will spontaneously separate into two distinct phases, namely a ^{3}He-rich phase and a ^{4}He-rich phase[2], also called the dilute phase. At any given temperature the mixture can only exist in either one of the two phases with their corresponding concentrations of ^{3}He, following the two lines emanating from the tricritical point. The dashed region below the phase separation line is inaccessible by the two phases. It must be noted that the phase transition of the ^{4}He-rich phase is incomplete: at 0 K the concentration of ^{3}He is approximately 6.6%. This fact can be used to cool down to very low temperatures. Since the liquid ^{3}He-rich phase is lighter than the superfluidic ^{4}He-rich phase, the former will

[2] As long as the overall ^{3}He concentration is at least 6.6%. Otherwise the mixture will remain in the mixed superfluidic phase.

float on top of the latter. Consider now the situation where some of the dilute phase is removed and some (almost pure) ^{4}He is added. Now, the concentration of ^{3}He in the dilute phase is lowered and there will be an osmotic driving force for the ^{3}He-atoms in the ^{3}He-rich phase to enter the dilute phase, since the enthalpy of an ^{3}He atom in the dilute phase is lower. This is in fact very analogous to the ^{3}He "evaporating" into the dilute phase, and this will cause the ^{3}He atoms to absorb heat, cooling down the entire mixture and providing the cooling power.

The rest of the dilution cryostat serves to separate the two isotopes at higher temperatures and to reinject them into the mixing chamber at low temperatures as not to negate the cooling power that was just provided. To this end, heat exchangers between stages play a crucial role, because the cooling power alone is not enough to bring the reinserted helium to the same temperature as the mixing chamber.

The dilution cryostat used is made by BlueFors Cryogenics.

3.2. Measurement setup

Because the physics at the scale of interest is about very small energies, it follows that the voltages and currents that have to be measured are very small, on the order of several microvolts and nanoamperes. Thus to properly measure our samples requires measurement devices that are very precise and introduce as little noise into the system as possible. The two most important measurement devices used for this are the IVVI and the lock-in amplifier, which are discussed below.

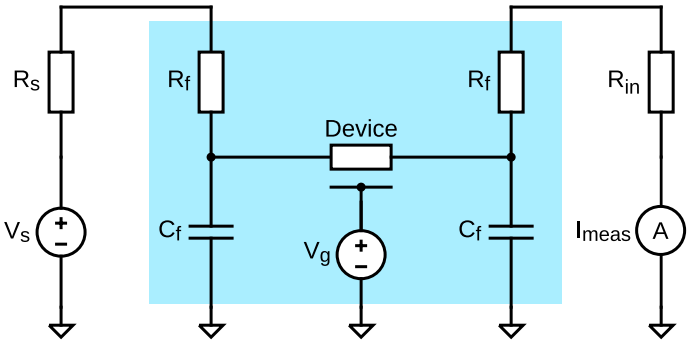

Figure 3.3: Simplified circuit diagram of the measurement setup. The voltage source V_s applies a bias voltage, R_s is the output impedance of the source, R_f are filter resistances, C_f are filter capacitors and R_{in} is the input impedance of the current meter. The chemical potential of the device can be adjusted by the gate voltage V_g. The lightblue region indicates the part of the circuit that is inside the cryostat.

3.2.1. IVVI

The IVVI is a DC measurement device developed in-house by the TU Delft [50]. It consists of a single large bus in the back whereto modules inserted in the front connect. Which modules are used is user configurable and the modules themselves often allow for internal configuration as well. The main purpose of the IVVI is to provide a way to excite a system and measure its response while keeping the introduced noise as low as possible. Because of this the IVVI is electrically isolated from the 50 Hz power grid by using battery power only. An optical cable is used to connect the IVVI DAC to a computer for power grid isolation. To provide the excitation to a sample, the IVVI can either generate its own voltages by means of the DAC or an external source can be used. The voltage signal is then attenuated, amplified or converted to a current by several other modules before being injected into the fridgeline, where it passes through the circuit depicted in 3.3. The two low-pass filters in this circuit have a cutoff frequency of around 100 Hz, making sure no high-frequency noise makes it either in or out of the system. The applied voltage will result in a current via Ohm's law as

$$I_{\text{meas}}(V_s) = \frac{V_s}{R_s + R_{\text{in}} + 2R_f + R_{\text{device}}} \tag{3.1}$$

The resulting signal is measured by the IVVI and sent to a computer for data acquisition and analysis. From this the voltage drop over the device can be readily extracted by subtracting the voltage drops over the other resistances, resulting in

$$V_{\text{device}} = V_s - I_{\text{meas}} \sum_i R_i = V_s - I_{\text{meas}} \left[R_s + R_{\text{in}} + 2R_f\right] \tag{3.2}$$

3.2.2. Lock-in amplifier

The lock-in amplifier works in a different way compared to the IVVI to reduce the noise and increase its sensitivity to small signals. It applies an AC excitation of a user specified frequency ω_0, ideally a non-integer multiple of the powergrid frequency, at the input of the sample, in our setup usually on the order of a few microvolts peak-to-peak. It then measures the response and mixes it with a copy of the signal that it applied at the input of the fridgeline. By doing this mixing step, the signal after the mixer contains the information of the signal from our device at two distinct points in frequency space: one at 0 Hz and the other at $2\omega_0$. This can be derived as follows. Take as the input signal $V_s = v_0 \sin \omega_0 t$. The signal will travel through the same circuit as in figure 3.3 and consequently the signal measured by the lock-in amplifier will have a new amplitude v_1 and will differ from V_s by some phase ϕ. Since mixing is essentially multiplying the measured signal with a reference signal we get at the output of the mixer

$$V_{\text{mix}} = v_1 \big[\sin(\omega_0 t)\big]\big[\sin(\omega_0 t + \phi)\big] = v_1 \frac{1}{2}\big[\cos(\phi) - \cos(2\omega_0 t + \phi)\big] \overset{\text{LP filter}}{=} \frac{v_1}{2}\cos\phi \tag{3.3}$$

where it was assumed that the reference signal had unity peak-to-peak voltage amplitude. By now passing this signal through a low-pass filter, we can remove the component at $2\omega_0$ and be left with the signal at 0 Hz only. Noise and other signals at different frequencies are either filtered as well or are removed by the powergrid cycle time averaging of the lock-in. Another way of looking at this is from the current point of view. Consider the expression from 3.1 and insert the expression $V_0 + V_s$, where V_0 is a bias voltage. We obtain by Taylor expansion about the offset voltage V_0

$$I_{\text{meas}}(V_0 + v_0 \sin \omega_0 t) = I(V_0) + \left.\frac{\mathrm{d}I}{\mathrm{d}V}\right|_{V_0} v_0 \sin \omega_0 t + (\text{h.o.}) \tag{3.4}$$

at the input of the mixer. It now follows that after the mixer, by similar method as done to obtain the voltage V_{mix}, the signal that survives will be

$$I_{\text{mix}} \overset{\text{LP filter}}{=} \left.\frac{\mathrm{d}I}{\mathrm{d}V}\right|_{V_0} v_0 \tag{3.5}$$

This result is fundamental in understanding that the lock-in amplifier measures the differential conductance $\mathrm{d}I/\mathrm{d}V$ at the voltage V_0, which can still have non-zero values even when zero bias is applied.

The lock-in amplifier used is a Stanford Research Systems SRS860.

4

Fabrication

4.1. Growth

In order to study the physics discussed in the previous chapter, nanowires need to be grown. While previous works used nanowires grown using for example the Vapor-Liquid-Solid (VLS) method [51–55], this work focuses on nanowires grown using Selective Area Growth (SAG) [56–60] using Molecular Beam Epitaxy (MBE). Before going into detail on the specific way the nanowires are grown, it is helpful to first give an overview of the growth steps involved, so that subsequent subsections can serve to fill in the details while the bigger picture is already in view.

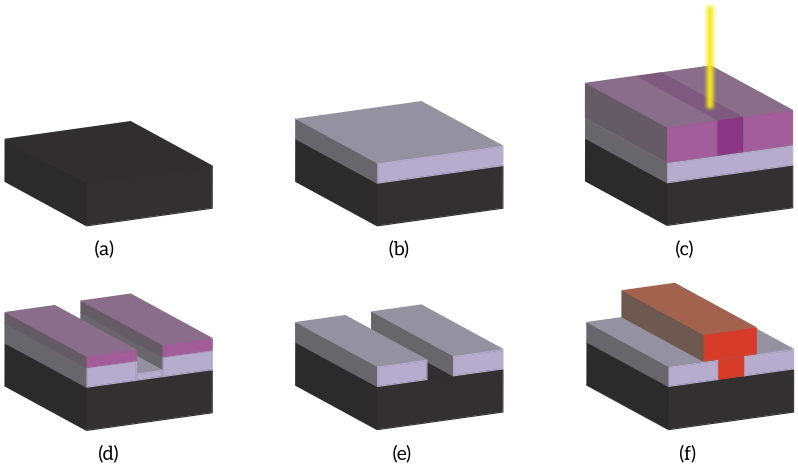

Figure 4.1: Schematic view of the substrate preparation process and the subsequent selective area growth of nanowires. (a) Start with a bare substrate. (b) Deposition of a global mask layer via PECVD (grey). (c) A layer of e-beam resist (purple) is spun over the mask layer and subsequently written (deep purple) via e-beam lithography (yellow). (d) The written area of the resist is removed and etching of mask is in progress. (e) Etching is complete and the remaining resist is removed. Trenches have formed in the mask according to the pattern defined by our mask design which was written in step (c) by the e-beam. (f) After etching, the nanowires (red) are selectively grown in the resulting trenches.

Figure 4.1 serves to illustrate the growth process. In figure 4.1a-b, a bare substrate is shown to be covered by a layer which will be used as a mask. Examples of substrates used are GaAs and InP. The mask material used is SiO_x or Si_3N_4. The mask is deposited globally across the entire wafer by Plasma-enhanced chemical vapor deposition (PECVD) which results in a conformal layer.

Next, figure 4.1c shows a layer of electron-beam resist being written by an electron-beam. The e-beam resist used was PMMA, but other types of resist are commercially available. PMMA is a polymer, having many chains of the same molecule *methyl methacrylate* linked together. PMMA used in this work was designated PMMA-950K, meaning the average chain length of this type is 950 thousand units of aforementioned molecule. These polymers are dissolved in an organic solvent, typically Anisol [61] in a concentration denoted by A*n*, where *n* denotes the concentration of polymer in solution by weight in percent. As an example, PMMA-950A6 has on average 950 thousand units of the monomer per

chain and is in a 6 percent solution by weight with Anisol. As the e-beam scans across the surface covered with resist, the resist polymers undergo an electrochemical reaction. Depending on the type of features that should be created in subsequent steps, positive or negative resist can be chosen. Positive resist will undergo a reaction where the long chains are broken up into smaller ones when they are exposed to the e-beam. These sections are then more easily dissolved in a developer solution, in our case exclusively a solution consisting of 1:3 parts MIBK:IPA. Thus, for this type of resist the area written is the area removed. This is in contrast to negative resist, where e-beam exposure causes the chains to become longer in a process called crosslinking. The resulting polymer chains are more difficult to dissolve and therefore the unwritten area will be dissolved more easily during developing. The resist is spread uniformly by spin-coating. The thickness of the PMMA layer depends both on the concentration in solution and the speed at which it is spin-coated, typical rotational speeds being 4000 rpm. Charts from the manufacturer [61] are used to determine the desired concentration and speed, based on the desired thickness.

After developing the resist, the resulting trenches serve as an etch mask, illustrated in figure 4.1d. When etching, the resist layer that is still on the mask will protect the underlying material, whilst the material that is now uncovered by the development step will be exposed to the etchant and is subsequently removed by it. Depending on the type of etching the resist layer itself is etched as well. Therefore it is important to spin a layer of resist thick enough such that the bottom of the hard mask can be reached by the etchant before all resist is removed. After etching is complete, the remaining resist can be removed by dissolving it in an organic solvent such as acetone. The result after etching is shown in figure 4.1e. This is the state in which the wafer will be just before being inserted into the MBE for growth, which will be discussed in section 4.1.1. The end result is shown in figure 4.1f, where a nanowire can be seen to have grown selectively in the trench.

4.1.1. Molecular Beam Epitaxy

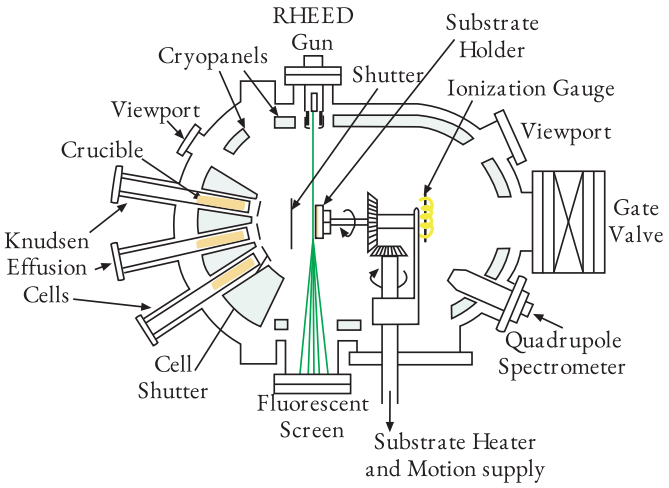

Figure 4.2: Illustration of an MBE growth chamber. Image taken from [62].

Molecular Beam Epitaxy (MBE) is a technique to epitaxially grow layers of a material onto a sample. An illustration of an MBE growth chamber is shown in figure 4.2. To ensure high growth quality with as little contamination as possible, the main chamber is under high vacuum and is baked during assembly or after maintenance to remove water adhering to the inner surfaces of the chamber. Samples can be introduced into the chamber via the load lock which is a separate chamber closed off via the gate valve. The stage on which the sample rests can be rotated both axially, to promote conformal deposition, as well as with respect to the sources to deposit under an angle, allowing for shadow evaporation. Knudsen effusion cells are mounted opposite of the sample. These contain source crucibles with high-purity elemental sources. Heaters will cause these sources to heat up and start emitting atoms. Due to the length of the tube connecting the cells to the main chamber and the high vacuum in the main chamber, the atoms will be collimated and will ballistically move towards the sample. Shutters control the flow of these streams of atoms towards the sample, allowing for quick enabling and disabling of the beam. Multiple sources can be enabled at the same time, allowing for compound materials to be grown. For the purposes performed in this work, notable compound materials are InAs and InSb, the semiconducting materials used for the nanowires.

As is in the name of the technique, the growth is epitaxial, meaning that layers grow on top of previous layers [65], which is shown in figure 4.3. The first columns of this figure displays an illustration of the progression of the growth as the current layer nears completion. As particles land on the surface of the sample, they will migrate due to the

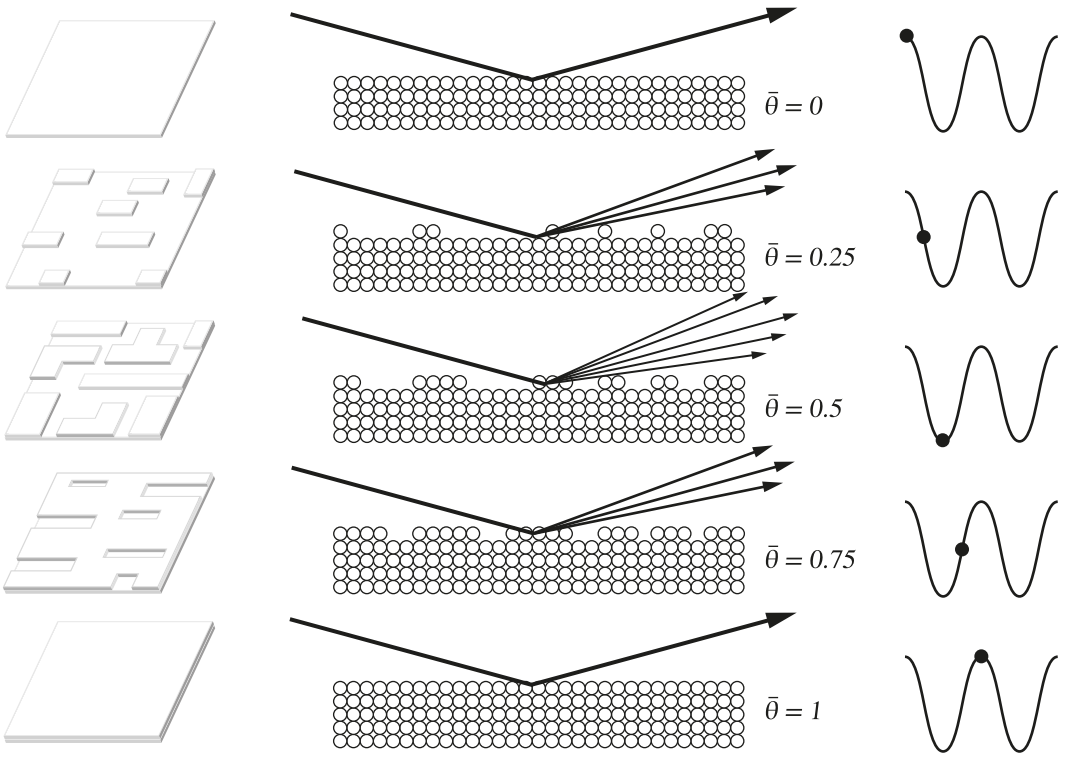

Figure 4.3: Epitaxial growth and the corresponding RHEED gun signal as function of the thickness parameter $\bar{\theta}$. Image inspired by [63, 64].

elevated temperature and coalesce when they meet other particles. This will cause the coalescing particles to grown in size and clump together. If these clumps grow large enough, they will become immobile. As more and more particles join these clumps, the clumps will grown into one another forming a single layer. Growth can be monitored by means of a Reflection High-Energy Electron Diffraction (RHEED) gun. This device shoots a beam of electrons onto a sample and a fluorescent screen on the opposite side of the growth chamber can be used to monitor the reflection of the beam on the sample. Depending on the stage of the growth of the current layer, the signal will oscillate as growth progresses, until the current layer is complete and the cycle continues, shown in the second and third columns of figure 4.3, where the growth parameter $\bar{\theta}$ is a way of indicating the growth progression. The third column shows the RHEED signal as an oscillating signal depending on $\bar{\theta}$, returning to its maximum value when the layer is complete.

4.1.2. Selective Area Growth

The growth of the nanowires is done by the growers in our group, Pavel Aseev *et al.* Because the growth was not performed by author for this work, it will not be discussed in great detail. The SAG method of growth relies on the nucleation of particles in a trench formed in a hard mask on the substrate. This trench will open up the substrate for the incoming flux op particles. Because the hard mask is amorphous, in our case SiO_x, and the substrate is crystalline, the particles arriving on the mask will start to migrate over the surface due to the elevated temperature in the MBE growth chamber. When they fall into a trench, they can lower their binding energy by aligning with the substrate crystal surface and binding with eachother, forming a crystalline structure in the shape of the trench. For the best results, the trench should be designed such that it lies along a crystal direction relative to the substrate direction. Ideally, the growth mode is Frank-van der Merwe [66, 67], meaning the growth progresses layer-by-layer. This process leads to the formation of very clean single crystalline nanowires in exactly the shapes defined in the mask. It is notable that a good SAG growth method for InSb in MBE was not available before the start of this project, something which our growers have made great strides towards as evidenced by the ballistic and phase coherent transport of the InSb SAG discussed in the results.

4.1.3. Thermal budget

When aluminium comes into contact with the InSb nanowires, it will undergo a reaction where it will diffuse into the crystal and replace one of the atoms from it. This is unwanted as the resulting compound will be different from the material we want. Wet-etching on the wire will also become more difficult as the aluminum will be taken from the compound and be dissolved in the etchant, leaving holes in the nanowire. This is most apparent when the sample has

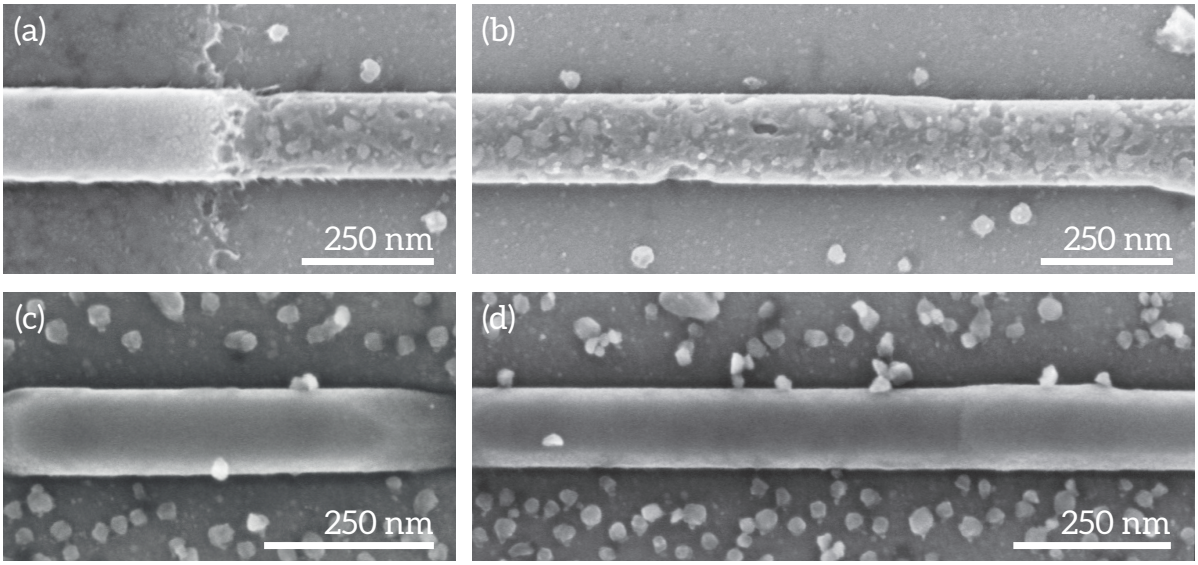

Figure 4.4: SEM images comparing wet-etch results on InSb nanowires. **(a,b)** Sample of several months of age after wet-etch. In **(a)**, also the wire protected from the etching can be seen underneath the mask (left side of image), which is still looks pristine from inspection by eye. **(b)** shows the etched wire. Many defects are introduced as the aluminium that has diffused into the nanowire has been etched away. **(c,d)** Sample of only a few days of age after wet-etch. The difference with the older sample can be seen, where here the newer wire still looks pristine after etching.

aged in room temperature, a comparison of which can be seen in figure 4.4. Here, a nanowire which is only a few days old and a nanowire which has been stored in a desiccator over the course of several months have been wet-etched under similar conditions. The older sample displays significant damage, which can be attributed to the aluminium having replaced some of the atoms up until a certain penetration depth.

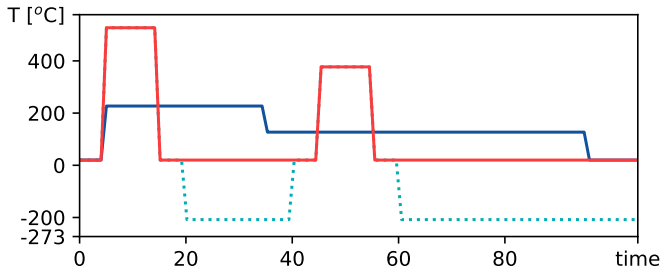

Figure 4.5: Temperature curves of three fictional processes. The processes with blue and orange colors have used approximately the same thermal budget, while the cyan curve has used significantly less thermal budget.

This degradation over time can be understood by considering the thermal budget. The time a sample is at a certain temperature determines the progression of some chemical processes. Such a process at some low temperature T_L needs more time compared to the same process that is performed at a higher temperature T_H. As an approximation, the two processes can be regarded as having progressed by the same amount when the integral of their temperature to time is the same,

$$B = \int_{t_0}^{t_1} T_L(t)\,\mathrm{d}t = \int_{t_0'}^{t_1'} T_H(t)\,\mathrm{d}t \tag{4.1}$$

Figure 4.5 shows the temperature of three fictional processes. Consider first the blue curve. This process has two steps at two distinct temperatures, then returns to room temperature. Another process, shown as the orange curve, can be seen as having roughly the same thermal budget B as the blue curve, even though the reactions happen at much more elevated temperatures. The used thermal budget can be reduced by either decreasing the time spent at higher temperatures or by cooling down the sample when it is not being processed, shown in the dotted cyan curve.

The thermal budget is important when we consider the sample degradation over time, both because of the aluminium attacking the nanowires, as well as the oxidation of the aluminium itself. Exposure to oxygen will cause a native oxide layer to form on the aluminium. Because the aluminium is very thin, this has the potential to completely convert the

thin layer into aluminium oxide, which is non-superconducting. A better understanding of the allowed thermal budget will tell us how much time can be spent at elevated temperatures when processing the samples.

4.2. Devices

To measure the electronic properties of the nanowires we need to make devices out of them. The following chapter will go over the cleanroom techniques involved when fabricating devices.

4.2.1. Electron-beam lithograpy

Electron-Beam Lithography (EBL) is used to transcribe the designed structures onto our samples. We first design structures using Computer-Aided Design (CAD) and convert these drawings into a format that can be understood by the Electron-Beam Pattern Generator (EBPG). The EBPG then accelerates electrons and shoots them at our sample, creating the designed pattern in the e-beam resist layer. The quality of the written area depends on factors such as acceleration voltage, dose, type of resist and backscattering. Because of these varying results, dose tests must be performed in order to find out an acceptable range of doses and beam currents.

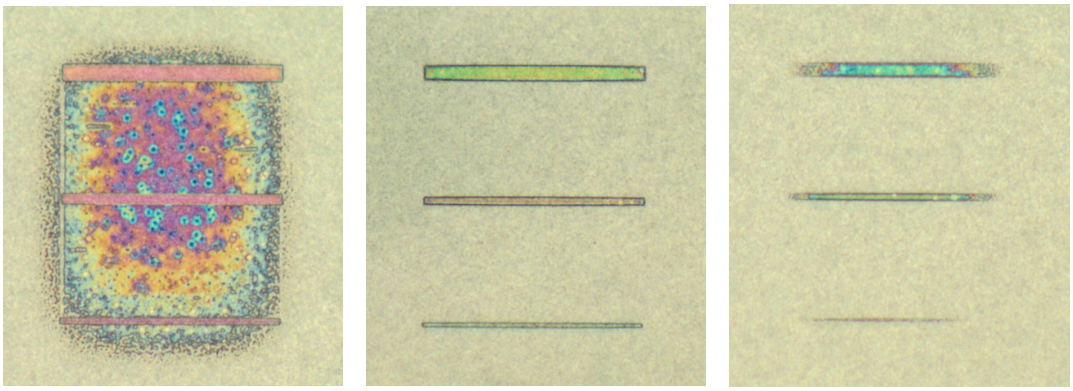

(a) (b) (c)

Figure 4.6: Images comparing doses. Three bars should be visible and consist of remaining e-beam resist. Outside area should have been exposed and subsequently removed during development. **(a)** Underdosing, which can be seen from the remaining resist in between the bars. **(b)** Good dose, all three bars are visible with all resist in between and around the structures gone. **(c)** Overdose, judging from the extremities of the bars being exposed when they should not have been exposed. Note also the bottom bar which is almost gone.

Figure 4.6 shows three distinct types of dosage. Underdosing, shown in figure 4.6a, occurs when the dose is not enough to expose all the resist in the written area. Here, only some of the resist underwent the electrochemical reaction where the polymer chains have broken into smaller parts (positive resist). Figure 4.6b shows a good dose, where all structures are written as intended, and figure 4.6c showcases an overdose. Here, the bars of resist have started to disappear due to exposure from backscattering. Resist doses can be characterized by their dose-to-clear parameter, the minimum dose required to completely expose a layer of resist of a certain thickness in an area unobstructed by structures, values of can be found by performing dose tests, but can sometimes also be found in literature [68].

4.2.2. Metal deposition

The contacts and gates are made of gold (thickness of roughly 150 nm) with a thin layer of titanium (10 nm) acting as a sticking layer between the underlying material (wire and substrate) and the gold. The reason titanium is used as such is its affinity to oxygen, causing it to be attracted to native oxide layer of the substrate. Furthermore, titanium and gold form an alloy on their mutual boundary. These two effects make titanium to be a widely used metal for adhesion [69, 70]. Metals are evaporated using Electron-Beam Physical Vapor Deposition (EB-PVD), show in figure 4.7. This technique uses an electron-beam to heat up a target. Metal atoms will then evaporate from the target and, due to the high-vacuum, travel ballistically towards the sample. The distance to the sample and the diameter of the tube connecting the target to the main chamber will collimate the flux of atoms, which will make this type of deposition very directional.

The nanowire also has a unwanted native oxide layer. The formation of this native oxide is uncontrolled and forms as strong barrier which will dominate transport processes. To get rid of this native oxide, sulfur passivation can be used to remove it [71] or the wire can be argon-milled. Another surface contaminant to take into consideration is leftover resist after development. Although ideally all of the exposed (positive) resist is dissolved into the developer solution, there still could be residues left on the sample, caused for example by slight underdose, deviations in developer mixture

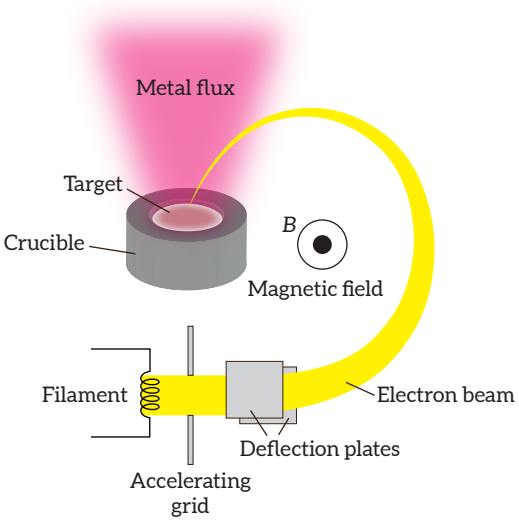

Figure 4.7: Illustration of a EB-PVD setup. Electrons are boiled off a tungsten filament, are subsequently accelerated and deflected and hit a metallic target inside a crucible. The electrons release their energy inside the target and this causes the target to heat up.

ratios or imprecise development timing. To get rid of this residue, the sample is briefly exposed to an oxygen plasma, which oxidizes the resist and takes away the reaction products.

4.2.3. Dielectric deposition

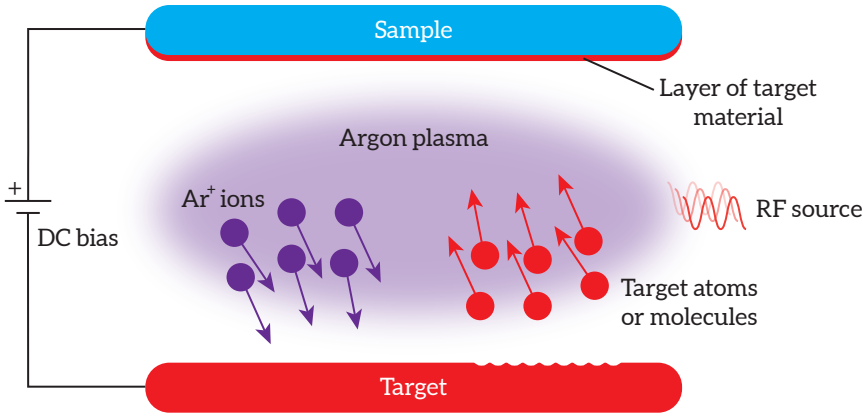

Figure 4.8: Illustration of the principle behind sputtering.

To isolate the nanowire from the gates a dielectric, in our case silicon-nitride (Si_3N_4), is sputtered globally on the sample. Sputtering is the process by which ions from a plasma bombard a target material, disjoining molecules from the target causing them to travel towards the sample. This is shown in figure 4.8. Here, an argon plasma is ignited and powered by an Radio-Frequency (RF) source. Due to the DC bias voltage between the sample and the target, Ar^+-ions will be accelerated towards the target at high velocities. Upon collision, the ions can dislodge atoms or molecules from the target material and send them flying towards the sample, forming a layer of the target material on the sample.

4.2.4. Fabrication recipes

The following recipe was developed to fabricate the devices on InSb nanowires grown on InP substrates with global aluminium deposited in-situ from the MBE.

- Spincoat PMMA-950A6 at 4k rpm
- Vacuum dry in a high vacuum environment for at least three hours. Resist resolution scales with time spent in high vacuum conditions, overnight is preferable.
- Write etch windows with EBPG. Beams and doses for the Raith EBPG 5200+ are as follows:

Class	**Pattern resolution**	**Beam**	**Dose** ($\mu C/cm^2$)
Fine	5 nm	18NM 8072PA 400UM	1000
Coarse	85 nm	128NM 309NA 400UM	1300

  Note: beams indicated are just labels, actual calibrated parameters may be different and do not carry to similar machines.

- Etching of aluminium can be done either using reactive ion etching or by wet etching. Etching recipes developed by Amrita Singh.
  - Reactive ion etching: temperature 0 °C, 10 seconds oxide breakthrough + 45 seconds aluminium etching. Bias voltage 280 V and 320 V respectively.
  - Wet etching: sample is dipped briefly in IPA, then briefly in water, followed by MF321 at 21 °C for 60 seconds. Etching stopped by dipping in three successive beakers of water followed by IPA. Blow dry with gaseous nitrogen.
- PMMA stripped with acetone bath for at least 15 minutes at room temperature
- Spincoat and vacuum dry PMMA as before
- Write contact patterns with EBPG. Beams and doses for the Raith EBPG 5200+ are as follows:

Class	**Pattern resolution**	**Beam**	**Dose** ($\mu C/cm^2$)
Fine	2 nm	16NM 1205PA 400UM	2050
Mid	20 nm	35NM 79PA 400UM	1700
Coarse	90 nm	99NM 260NA 400UM	1050

  Contacts and gates written with the same doses.

- Develop with 1:3 MIBK:IPA mixture for 1 minute, rinse in IPA for 1 minute, blow dry with gaseous nitrogen
- Oxygen plasma to remove PMMA residues, flow 400 ml/min, power 100 W, time 30 seconds
- Sulfur passivation at 60 °C for 30 min, water transfer
- Argon milling before deposition 20 seconds
- Deposition of metal contacts, 10 nm Ti or Cr sticking layer, followed by 150 nm Au
- Liftoff in acetone at RT
- Si_3N_4sputtering, thickness 40 nm
- Proceed for the gates with PMMA, EBPG and metal deposition as described above for the contacts

5

Scalability

The computational power of a quantum computer scales exponentially with the number of qubits, as the number of states that can be simultaneously encoded via superposition is 2^n, where n is the number of qubits. In the case of topological quantum computation with Majoranas, we need two pairs of Majorana Bound States to form a single qubit since we need to be able to perform all three Pauli gates $\sigma_x, \sigma_y, \sigma_z$ via braiding to make an actual qubit out of the MBSs. All of these nanowires need to be connected to one another in a configuration such as the Majorana box qubit [72] or the so called hexon or tetron structures [73], both shown in figure 5.1.

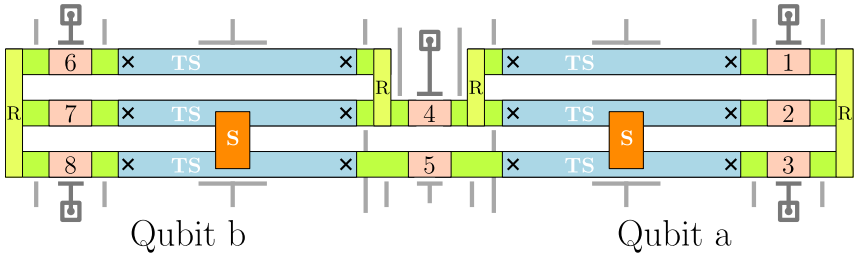

(a)

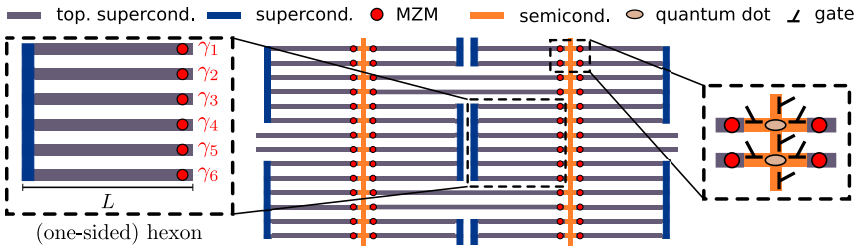

(b)

Figure 5.1: Two examples of Majorana qubit proposals. **(a)** Majorana Box Qubit (MBQ) proposal by Plugge *et al.* [72], here shown with two qubits a and b connected via two quantum dots indicated by 4 and 5. **(b)** Majorana hexon qubit proposal by Karzig *et al.* [73]. The left inset shows the hexon structure with one qubit and one ancilla Majorana pair.

With these proposals on the horizon, practical application begs the question: how would would we use nanowires to create a scalable platform for topological quantum computation with Majoranas? Previous results that found signatures of Majoranas [74–76] were performed with Vapor-Liquid-Solid (VLS) grown nanowires [40]. This method however is clearly not very scalable, as these nanowires need to be manually placed. When considering a qubit system on the order of 100 qubits, placing individual VLS nanowires very quickly becomes cumbersome and time consuming. Reproducible placement of VLS nanowires is also difficult to achieve owing to the random nature of the VLS nanowire deposition on the chip after growth and the resulting manual labor needed to displace the nanowires to the desired locations on the chip. This is where SAG comes in. Using the SAG technique, described in more detail in section 4.1.2, the location of the nanowires can be designed beforehand, after which a growth process will deposit semiconducting material in these locations to form nanowires. For this work, the growth process was performed by MBE. Such a method is, in contrast to

VLS, highly scalable and highly reproducible, ideally resulting in the ability to mass-produce chips containing identical nanowires in exactly the same locations.

This chapter is devoted to outlining the requirements for scalability, the hurdles that have to be overcome and to propose several solutions. Firstly, it is necessary to establish what is meant when talking about scalability. A scalable platform for topological quantum computation would have to

- have many Majorana qubit devices
- produced with a high yield
- fabricated simultaneously on the same chip
- be ready for performing braiding operations straight out of fab

The first of these points will be discussed in section 5.1, where the use of a mask to grow nanowires using SAG will be outlined. Secondly, the yield of the growth will be discussed in section 5.2. Autorouting will be discussed in section 5.3, which will discuss the issue of correctly and efficiently routing the leads from the devices to the bondpads. Finally, some post-fab issues pertaining to bonding and getting signals in and out of the fridges will be discussed in section 5.4.

5.1. SAG mask

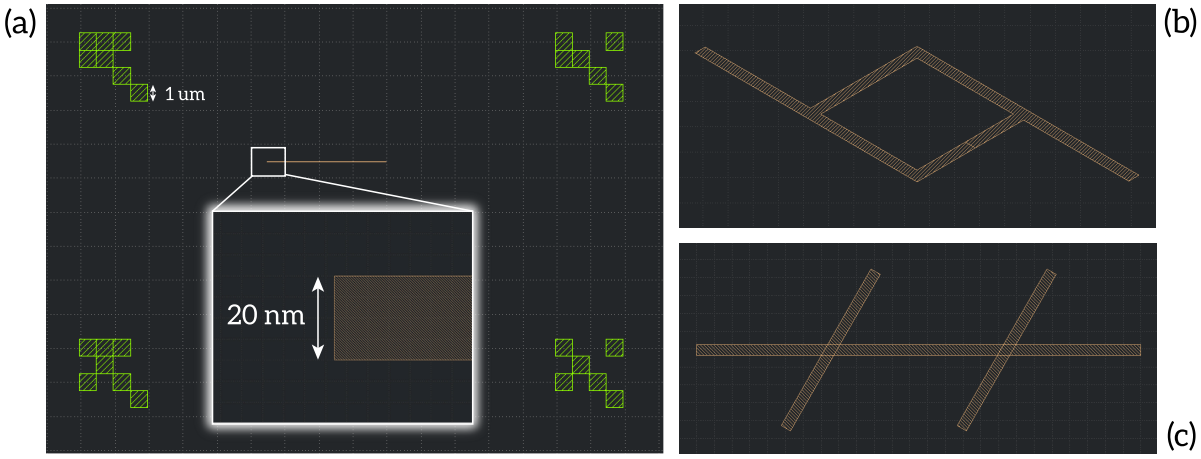

Figure 5.2: Images taken from the CAD drawing program displaying the design of SAG mask openings. The nanowires are shown in orange. **(a)** This particular wire has a width of 20 nm (inset), but varying sizes from 20 nm to 200 nm have been designed as well. Bitmarkers are shown in green with a sidelength per square of 1 micron. **(b)** An loop structure meant for measuring Aharonov-Bohm oscillations. **(c)** Hall-bar structure.

The need to have many Majorana qubit devices is one that will remain regardless of what platform (SAG, VLS, 2DEG, etc.) will eventually become the standard. Many qubits are needed to eventually perform useful quantum computations and for each qubit we need multiple pairs of MBSs. The choice for nanowires grown using SAG then quite naturally leads to the use of a mask, in which openings are etched to promote the growth of semiconductor material in the resulting trenches. Figure 5.2 shows several designs of mask opening. Wires can be grown in a variety of thicknesses, ranging from 20 nm to 200 nm in our case. In figure 5.2a the design of such a straigt nanowire is shown, with a close-up in the inset. Figure 5.2b-c show two structures that would be very difficult to grow using VLS wires, although people have been able to grow such structures in VLS by devising clever ways of growing on sloped surfaces [77, 78]. SAG however offers arbitrary structure growth with the only restriction being the angles of intersections, which have to correspond to the crystal symmetries. These symmetries are determined by the substrate directions and the semiconductor crystal orientations, since the nanowires will nucleate directly on the substrate through the mask openings. The substrate orientations used for this work are [100] (45° rotational symmetry) and [111] (60° rotational symmetry with 30° offset, i.e. rotationally symmetric by $30^\circ x + 60^\circ k$, $k \in \mathbb{Z}$, where $x \in \{0, 1\}$ determines the offset). The ability to create arbitrary structures is of great importance when the proposals shown in figure 5.1 are kept in mind. Once a good growth recipe has been developed, any structure can be grown and very little additional work needs to be done, making SAG an ideal platform for topological quantum computation.

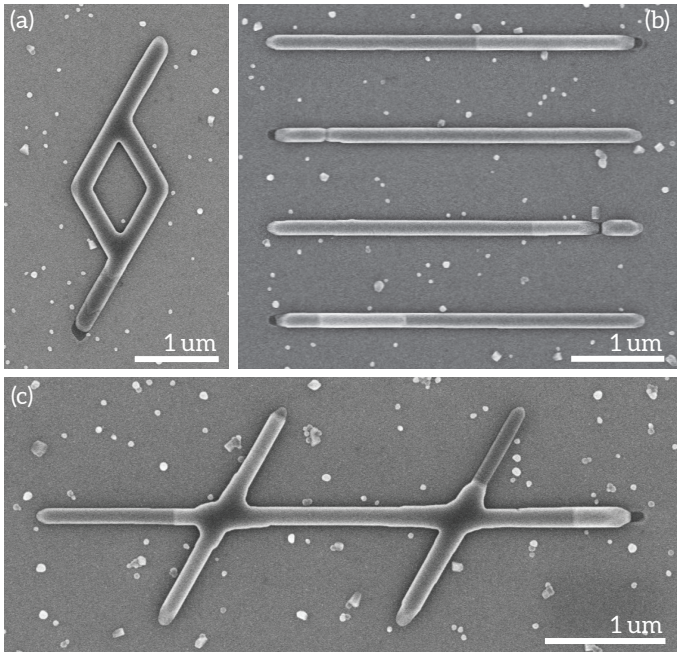

Figure 5.3: Several SEM images showing different growth qualities. In all images, parasitic growth can be seen. **(a)** Aharonov-Bohm loop. The SAG growth looks overall pristine, with the only blemish being some uneven step coverage in the bottom area of the wire. **(b)** Four straight nanowires. Step coverage is visible by the difference in grey shade. Breaks in the nanowires can also be seen. **(c)** Hall bar with step coverage differences clearly visible. At the intersections, the wire thickness is not uniform. Bad growth has occurred in the top-right appendage of the Hall bar.

5.2. Growth

A consistent growth method is needed for InSb SAG to become a viable platform for topological quantum computing. To illustrate the variety of growth that can be obtained, refer to figure 5.3, which shows three examples of different growth qualities. In figure 5.3a, an AB-loop can be seen. The quality of the SAG growth is here pristine, which can be judged from the uniform step coverage and smooth edges. The only irregularity can be found in the bottom extremity of the loop, where an uneven step coverage can be seen. This is however not an issue since we can design the leads of the contacts such that they contact just after this uneven region. Figure 5.3b shows four straight nanowires. Uneven step coverage is most clearly visible in the top and bottom wires, where the difference in grey shade is indicative of a step coverage mismatch. Breaks in the wires can be seen in the remaining two wires. Figure 5.3c shows a Hall bar which suffers from uneven step coverage, uneven growth and uneven thickness. Step coverage mismatches and non-uniform thickness results in an increase of disorder in the wires. Breaks will cause the wire not to conduct across the junction, rendering that part of the wire useless. Parasitic growth can be see in all three images as dots surrounding the nanowires. This parasitic growth is InSb that has nucleated outside the trenches. This parasitic growth is not an issue as long as it does not touch the wire. If it touches, the resulting blob could lead to an increase in disorder as it would become a scattering center near the surface.

5.3. Autorouting

When devices are fabricated, the leads on the nanowires (500 nm) need to fan out towards larger bondpads (100 x 150 micron) so they can be bonded to a PCB. This process is quite labor intensive for many devices and can become a bottleneck when scaling up. Therefore, a better method would be to automate this design step. Progress has been made towards this during this work. A package, gds_tools, was developed[1] by author aiding in designing structures using the scripting language Python in conjunction with the gdspy-package[2] which creates layouts in the GDSII file format, allowing for the design of structures through a programming interface. This package implements the creation of device primitives according to a set of user parameters. Examples include SQUIDs[3], resonators and waveguides. An example script is shown in codeblock 5.1.

[1] `https://github.com/kouwenhovenlab/gds_tools`
[2] `https://pypi.org/project/gdspy/`
[3] Superconducting Quantum Interference Device

```python
#!/usr/bin/python3
import numpy as np
import gdspy as gd
import gds_tools as gtools

squid_1 = gtools.squids.square(1, 20, 1, 1, 10)
squid_2 = squid_1.copy().rot(-np.pi/2).con('SQUID_A', squid_1, 'SQUID_B').heal('SQUID_A')

squids = [squid_1, squid_2]

c = gd.Cell('DEV')
gtools.add(c, squids)

gtools.save(c, 'squid_example.gds')
gd.LayoutViewer()
```

Codeblock 5.1: Example of scripted CAD using Python, gdspy and gds_tools.

In this example, two SQUID structures are created. On line 6, the first SQUID is initialized with some geometric parameters (they are not particularly important, but what each positional argument represents can be found as comments documented in the source code). Then on line 7, a second SQUID is created by making a copy of the first one and is rotated by $-\pi/2$ using the `.rot()` method. It is then connected to the first SQUID using the endpoint names of both structures via `.con()`. The two SQUIDs are now positioned such that their extremities overlap. The class instances of both SQUID structures will keep track of the fact that they are now connected via a doubly linked list. This allows for other methods such as `.mov()` and `.rot()` to traverse the linked list in both directions and move or rotate all other connected structures when only one of the structures is instructed to perform such a transformation, causing the chain of structures to move as one, even though they technically are still individual class instances. Lastly on this line, a healer function `.heal()` will ensure proper overlap between the endpoints of the SQUID structures. On line 11, a GDSII cell is created named `'DEV'` using a built-in function of gdspy, to which on line 12 the SQUIDs are added. Line 14 saves the cell to a file and line 15 displays the layout from memory. The output of this block of code is shown in figure 5.4.

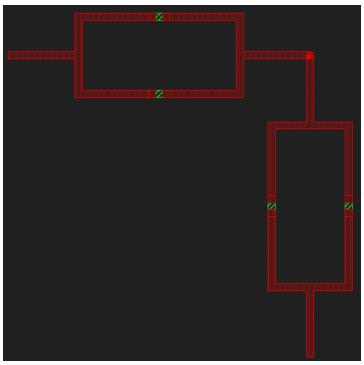

Figure 5.4: Output of codeblock 5.1. Two connected SQUIDs can be seen made via scripted CAD.

This was a relatively simple example, yet it shows that with only a few lines of code, layouts can quickly be designed and adjusted by simply specifying a few parameters. When scaled up to large designs, this approach will be easier to work with, since all manual labor is expedited to the computer. Ideally, in the long run, this would lead to a designer only having to specify how many qubits they want, entering parameters such as spacing between Majorana sites, nanowire thickness, etc. without having to bother with the specific placement of structures, only how they should be connected. This is analogous to how SPICE-like programs are used in the field of Electrical Engineering to build and simulate electronic circuits, where a user only has to define a netlist after which the program will assemble the resulting circuit. Of course, the work presented here is on a lower level than conventional SPICE-like programs, since we are working at the level of the individual quantum circuit structures ((super)conductor, semiconductor and insulator geometries), rather than simply connecting already existing electrical circuit components (resistors, transistors, etc.), but the idea is essentially the same.

Building upon these ideas, autorouting has been developed as well to alleviate the process of wiring up the devices. Autorouting is the process by which a program connects the devices to the bondpads, however it can perform routing between two arbitrary points, and thus is not limited to only the bondpad usecase. Autorouting is an NP-hard[4] problem (time complexity $\mathcal{O}(MN)$ for an M×N grid) [80]. The algorithm employed is the Lee algorithm, which is a classic maze-runner algorithm [81, 82].

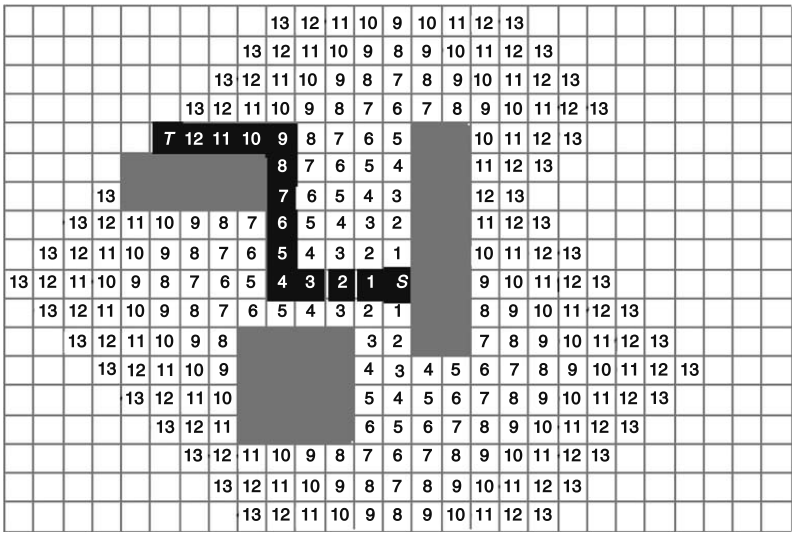

Figure 5.5: Labeling of the cells by the Lee algorithm. The wave-like expansion from the source S (label 0) to the target T (label 13). Obstacles in grey. Found route shown with black background. Image from [82].

The result of a successful run of the Lee algorithm is shown in 5.5. First, the entire area to be routed is divided into cells. Then, the algorithm starts at a source cell S and labels it with an index i. It then looks at all neighboring cells in a square grid-like fashion (no diagonals) and labels them with an index $i + 1$. It continues with these newly indexed cells, labeling all next neighbor cells with an index $i + 2$ etc., resulting in an overall labeling for an arbitrary cell of $i + k$, with k being the Manhattan distance of the cells with respect to S. If a neighboring cell is found to lie inside an obstacle, shown in figure 5.5 in grey, the cell is marked with a special number (for example, -1) and no further steps are done for this cell. Because structures are not guaranteed to be aligned with the grid of cells, detection of obstacles is done with a boolean check of a cell being within a small radius ϵ of another structure. The resulting pattern of labels as their numbers increase can be seen as expanding in a wave-like fashion, emanating from the cell S and bending around obstacles. Once the target cell T is found, the algorithm is finished and backtracks the path in order of descending index, carving a path in the grid. This path is guaranteed to be the shortest path on the grid if a solution is found, however a solution cannot be guaranteed beforehand. Also note that the path backtracked is not necessarily unique, as there will be multiple shortest paths available in Manhattan distance. A preference then can be specified between choosing paths, for example by letting the algorithm always choose the path that goes in the y-direction if it has the ability to choose.

A complete chip design that has been autorouted can be seen in figure 5.6. Here, a mask design was imported in Python and bondpads placed by gds_tools. Bondpads are grouped per six such that they can be more compactly be addressed by the user. Nanowires are grouped in cells, each cell containing six nanowires in various orientations. The locations of these wires are imported from a file generated with the mask design. A user specified mapping between bondpad groups and nanowire groups is then supplied to the script, which will then place the contacts and gates over the nanowires (figure 5.6b-c) and perform the autorouting.

Although the Lee algorithm produces usable results, it is not the most efficient algorithm. More efficient algorithms such as the A* algorithm [83] could be employed. Routing is also restricted by the order of placing routes, as routes are not allowed to cross. Thus conditions often arise where a path already routed blocks off a viable route for the next pair of nodes to be routed. This could perhaps be overcome by changing the order of generating neighboring routes if a route fails, dynamically rerouting to try to obtain a viable path for all of the node-pairs. The script used to do the autorouting in this particular case can be found in appendix A.

[4] Interestingly, the maze-runner problem can be converted into a search problem which is solvable by a quantum algorithm [79] albeit with some restrictions on the maze.

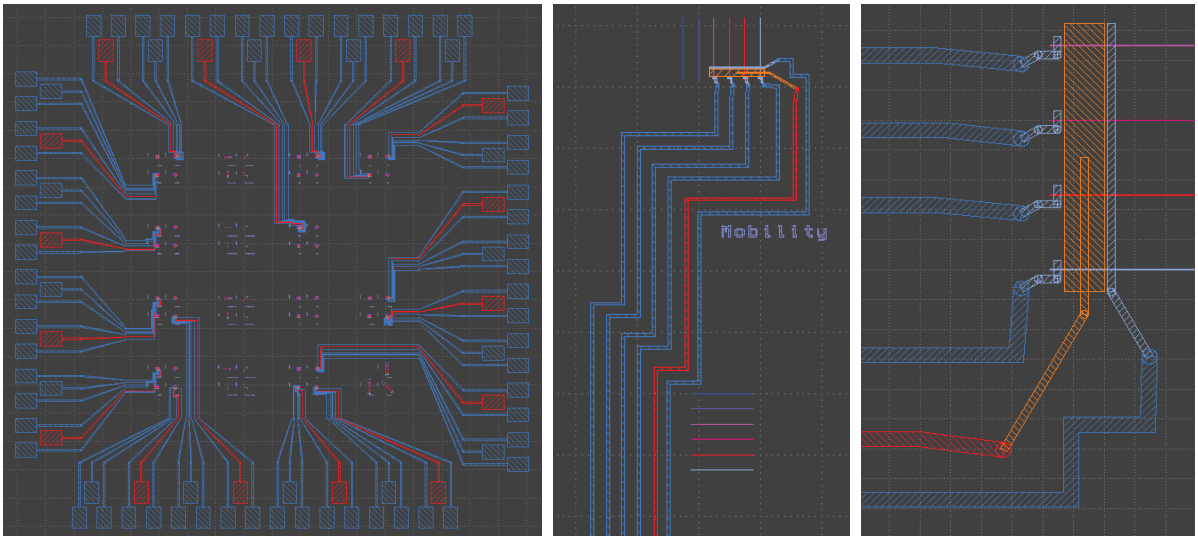

Figure 5.6: Autorouted design. **(a)** Paths have been drawn from the devices (nanowires) towards nodes close to the bondpads, after which these nodes and bondpads are connected by a straight line. Contacts leads in blue, gate leads in red. **(b, c)** Close-up of a wired up device. Both the contacts and the gates on top of the wires are automatically placed according to the user specification of the group of wires to be wired up. On-wire contacts in lightblue and gate in orange.

5.4. Autobonding

As the number of devices grow when scaling up, wire bonding will also become a concern. Wire bonding is the process by which a small wire with a diameter of several micron is pressed on a piece of metal and subsequently heated by ultrasound. The high frequency of the ultrasound will cause the wire to vibrate, heating it up due to friction and in effect soldering it to the metal surface [84]. Conventional bonding is manual labor and as such will take a considerable amount of time when a large number of devices need to be bonded. Not only for qubits but also for the purpose of mass characterization of the growth we need a high number of bonds. Our current designs already have on the order of 100 leads that need to be bonded and with the proposals discussed at the beginning of the chapter this number is very likely going to increase. The binding is also for a large part dependent on the surface that is being bonded to. In our case, bonding on Ti/Au surfaces. In some cases however, the bonding would fail due to the wire not sticking to the bondpad or the wire being pushed through the bondpad completely. Changing parameters such as force, US power or time had little effect in these cases, only would only switch between the two extremes. A destroyed bondpad renders a device partly or completely non-measurable. To increase yield, we have also used NbTiN as the last layer on top the Ti/Au. NbTiN is a much harder material than gold and bonding on NbTiN shows much more consistent and successful results. The bonder used for this work is made by F&S Bondtec GmbH. This bonder is capable of doing automatic bonding (autobonding), which has the potential of increasing throughput considerably, although autobonding was not used for this project. The high number of connections needed are not only a concern when it comes to routing or bonding however. The large number of fridge lines exposing the leads of our devices to the measurement setup are also a concern. The fridges used in this work have 96 fridge lines, however this might become a bottleneck in the future as the number of qubits is scaled up. A possible solution to this could be using RF measurements, using resonators at different frequencies to modulate the response of our devices in frequency space, reducing the number of fridge lines.

6

Nanowire quality

With the previous chapters outlining the need for a scalable platform for topological quantum computation with Majoranas and with SAG being proposed as a viable contender for forming the basis of this platform, it is now time to take a look at the actual performance of SAG InSb nanowires. First, we will take a look at InAs nanowires grown before InSb was available from the MBE in section 6.1. We will discuss the field-effect mobility (FEM) of these wires and inspect some pinch-off curves. In section 6.2 we will discuss the results obtained with InSb nanowire growth in MBE. Again, FEM will be discussed, as well as an alternative way of measuring the mobility using Hall bars. Ballistic transport results in QPCs and phase coherent transport in Aharonov-Bohm loops will be shown, as well as Coulomb blockade in nanowire islands. The first results of superconductivity will be shown in section 6.3, where preliminary results of the superconducting thin aluminium film will be discussed.

6.1. Indium-Arsenide

Before the availability of InSb in the MBE growth chamber, InAs SAG was grown. InAs has a large g-factor just like InSb and so would also be a candidate material for fabricating devices that exhibit MBSs. InAs was grown on a [111] and [100] GaAs substrates. For this work, only FEM measurements for InAs samples using the [100] GaAs substrate were performed.

6.1.1. Field-effect mobility

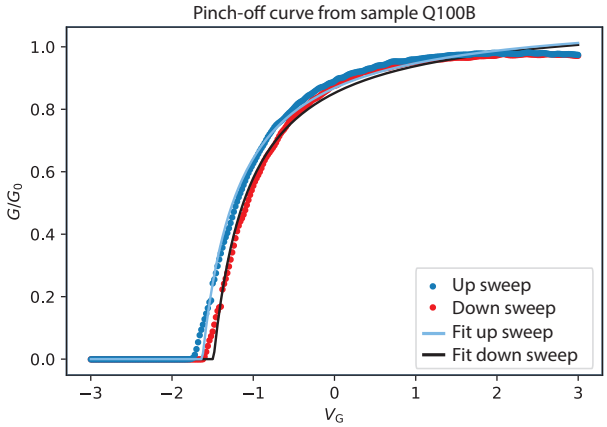

Figure 6.1: Pinch-off curves for an InAs nanowire. Two pairs of traces can be seen, one while sweeping the gate voltage V_g from negative to positive, the other from positive to negative, both accompanied by fits. Hysteresis is observed as a shift in V_g between the sweeps.

Field-effect mobility has been measured in InAs nanowires grown in MBE using a pulse-tube cryostat at a base temperature of 4 K. Pinch-off curves have been taken by depleting the local density of states in the nanowires directly below the gates by sweeping the gate voltage and measuring the conductance at 10 mV bias. Such a pinch-off curve if shown in figure 6.1.

Here, two traces in opposite sweeping directions of V_g can be seen. Equation 2.43 has been used to fit the data, with fitting parameters R_s, μC and V_{th}. The series resistance coincides with the sum of the resistance of the bondpads on the PCB to which the chip is bonded (which have a built in resistance of 5 kΩ or 10 kΩ depending on the bondpad), the resistance of the source and meter (3 kΩ) and the contact resistance of the leads contacting the nanowire (varies per device). To extract the mobility from the product μC, the capacitance C is obtained from simulation using a 3D electrostatic metallic model. The parameters are then fitted and the mobility μ is extracted. Because of this, the value of μ is highly dependent on the simulation quality. As the metallic model will overestimate the capacitance, the mobility will be underestimated. An over- or underestimation of the capacitance affects the mobility greatly. Another observation that can be made from these pinch-off curves is that the fitting quality is best where the slope is steepest, with relatively bad fitting near saturation. This might be caused by the assumption of the mobility being constant as a function of gate voltage, while this might not be the case. An explanation of this non-constant mobility could be explained by the lower carrier density near pinch-off. This would screen atomic impurities to a lesser degree, causing slightly more localization of the electrons near these impurities and thus reducing the mobility [85] in the near pinch-off regime.

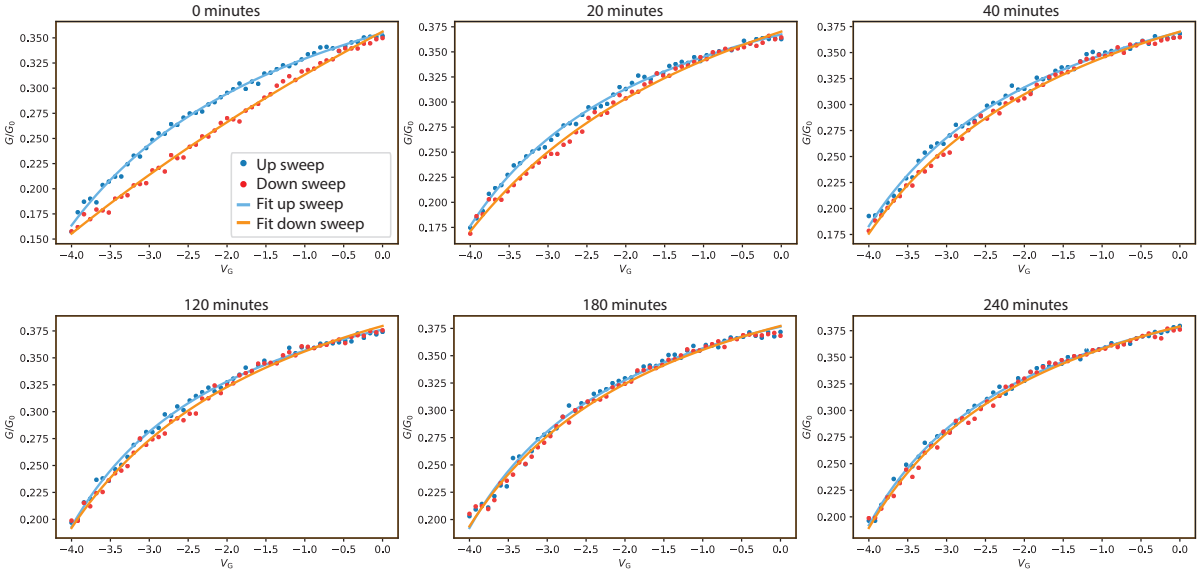

Figure 6.2: Pinchoff curves as a function of time spent at elevated temperatures. The hysteresis between the up and down sweeps disappears at prolonged heating times.

Hysteresis in the pinch-off curves can be attributed to water being adsorbed onto sample [86, 87]. Water is a polar molecule, causing it to orient itself in the direction of the field when we sweep the gate voltage. This polarization of the water molecules will contribute to the effective field at the nanowire, causing a shift in the chemical potential and thus the local density of states. As the gate voltage is swept back in the opposite direction immediately after a previous sweep, this polarization will influence the onset of pinch-off, causing a hysteresis effect. As was mentioned by [40], prolonged pumping down of the sample will cause the water to evaporate and thus desorb from the surface of the sample, reducing the hysteresis. In this work, the desorption has been attempted by heating the outside of the pulse tube cryostat with a heating blanket at 85 °C prior to cooldown at atmospheric pressure. The results of these tests is shown in figure 6.2. These tests show that heating for at least 3 hours is enough to get rid of the polar contaminant, suspected to be water, causing the hysteresis.

A typical mobility device on the Q100B sample can be seen in figure 6.3a. The four wires are connected to a common drain, but are individually connected to a source lead. The gate is shared among all four wires. This way of wiring will consume less bondpads and is less labor intensive for the designer drawing the leads, however it has an increased risk of device failure, since if the shared leads fail to be fabricated properly, four wires instead of only one will be wasted. Parasitic growth can be observed near the nanowires. Figure 6.3b shows the FEM of the InAs sample Q100B. Combining these results, the average mobility of all measured wires is $1.36 \cdot 10^3 \pm 0.20 \cdot 10^3$ cm^2/(Vs). The average mobility of all 0° wires is $1.28 \cdot 10^3 \pm 0.14 \cdot 10^3$ cm^2/(Vs) and for −45° this is $1.48 \cdot 10^3 \pm 0.24 \cdot 10^3$ cm^2/(Vs). Because these values lie within eachothers error ranges, no clear conclusion can be drawn about which growth direction gives better mobility for InAs SAG growth.

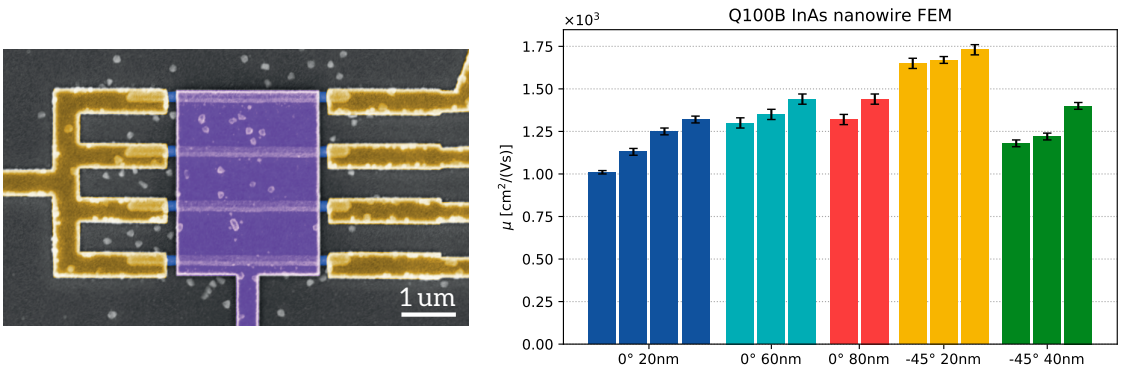

(a) (b)

Figure 6.3: Mobility results for Q100B InAs SAG sample. **(a)** Colorized SEM image of a typical mobility device used. The gate is colored in purple, the contacts in gold and the nanowire that is not covered by metal in blue. **(b)** Bar chart showing the FEM of the wires on this sample. Fit error as error bars.

6.2. Indium-Antimonide

Several samples with InSb growth have been fabricated and measured. The samples that will be discussed in this section are InSb nanowires grown on a [111] InP substrate. The FEM of all relevant chips will be discussed in subsection 6.2.1. This FEM will be compared to Hall mobility obtained from Q169 samples in subsection 6.2.2. Ballistic transport is shown in QPCs from samples Q163 and Q169-1400b in subsection 6.2.3. Phase coherent transport in Aharonov-Bohm loops in sample Q169-1700 and Coulomb blockade in quantum dots in the Q169-1400b sample will be discussed in subsection 6.2.4 and 6.2.5 respectively.

6.2.1. Field-effect mobility

FEM was measured of the single wires on the samples Q169-1700 and Q169-1400b. Methodology was similar to the InAs wires. A 10 mV bias was applied and the gate voltage was swept to obtain pinch-off curves.

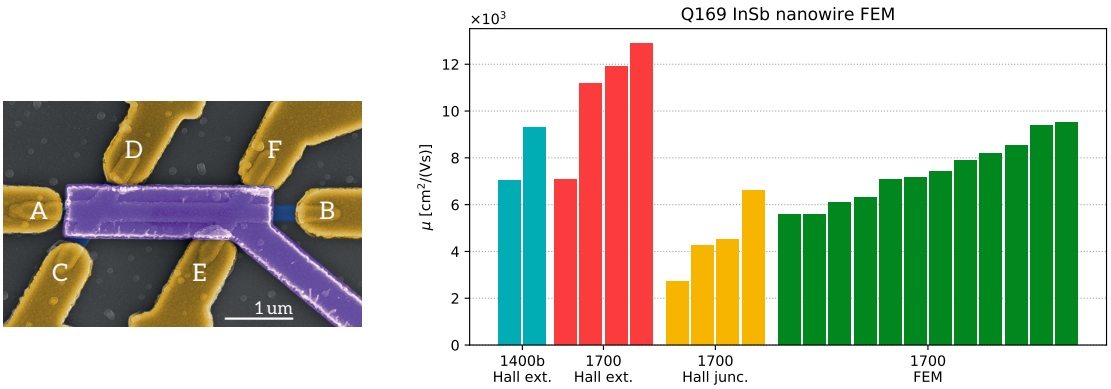

(a) (b)

Figure 6.4: InSb FEM. **(a)** Colorized SEM image of a Hall bar. Gate in purple, contacts in gold. Nanowire not covered by metal in blue. **(b)** Bar chart of the FEM obtained from samples Q169-1700 and 1400b. Labels 'Hall ext.' refers to measurements between the Hall bar extremities, while 'Hall junc.' refers to across-junction measurements.

Figure 6.4b shows the FEM results for these two InSb SAG samples. Here, the capacitance C is obtained from 3D electrostatic simulations using Thomas-Fermi [88, 89]. Labels 'Hall ext.' and 'Hall junc.' indicate FEM measured across a Hall bar, with the former indicating measurement between the two most distant contacts (refer to figure 6.4a: A-B), while the latter refers to cross-junction measurements (figure 6.4a: C-D, E-F). From this it can be seen that the FEM across the junctions are much lower compared to the contacts at the extremities. This is probably caused by the inaccurate estimation of the capacitance C used for FEM fitting. The FEM of the Hall bars between its extremities,

$9.90 \cdot 10^3 \pm 2.49 \cdot 10^3$ cm^2/(Vs), seems larger than that of normal FEM devices, $6.85 \cdot 10^3 \pm 1.89 \cdot 10^3$ cm^2/(Vs), however here again the two values fall within each others error ranges. A larger number of Hall bar FEM might be needed to determine whether there really is a difference between Hall bar FEM and normal FEM devices. Comparing the number for FEM devices with InSb nanowires to InAs nanowires it can be seen that InSb nanowires in general have a much larger mobility than InAs nanowires. As was mentioned for InAs wires, the capacitance might be overestimated due to the metallic model used to obtain it causing the mobility to be underestimated. A reason for the difference between InAs and InSb could be that InAs is known to have more stacking faults based on transmission electron microscopy (TEM).

6.2.2. Hall mobility

Another method of obtaining the mobility is using the Hall effect. The mobility obtained here is not dependent on the value of a capacitance obtained from simulation and is obtained as an inherent property of the semiconductor nanowire. A Hall bar is current biased with 10 nA between points A and B from figure 6.4a. An out of plane magnetic field is turned on and a Hall voltage V_H will develop between the points C and D (or E and F). Due to the current and the finite resistance of the semiconductor nanowire, a voltage will also develop between points D and F (or C and E). By measuring these quantities simultaneously we can do a 4-point measurement of the Hall bar and extract the relevant parameters as was outlined in subsection 2.6.2. A schematic of this measurement can be seen in figure 6.5. The current source can be seen biasing the Hall bar. A magnetic field causes the Hall voltage V_H to develop as electrons accumulate due to their half-cyclotron orbits at the edge of the Hall bar. The length L_{xx} is taken as the center-to-center distance of the crossings. The width W of the nanowire is determined in an area where no overlap with metal is made, since these metal structures will create an apparent broadening of the wire in the SEM images.

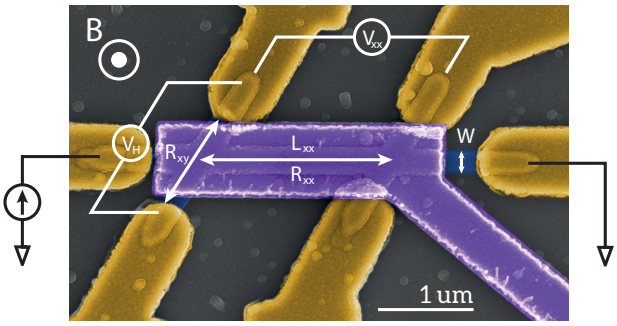

Figure 6.5: Measurement setup of a 4-point measurement on a Hall bar. A current bias is applied between the hall bar extremities. The Hall voltage V_H is measured across the bar while the voltage developing due to the resistance of the semiconductor is measured via V_{xx}.

Hall bars were measured from the Q169 samples. A magnetic field is applied parallel to the substrate normal and 2D field vs. gate voltage sweeps were taken of the equivalent Hall resistance $R_{xy} = V_H/I_{bias}$ and the intrinsic resistance $R_{xx} = V_{xx}/I_{bias}$, which can be seen in figure 6.6. The weak anti-localization (WAL) peak can be seen in figure 6.6a at $B = 0$. Close to pinch-off, the resistance R_{xx} is high and goes down as the gate voltage is increased. To obtain a value for the mobility and carrier density, only a single value of R_{xx} is needed for every value of the field. Therefore, R_{xx} is averaged over field for every gate voltage, since the intrinsic resistance should not be a function of magnetic field apart from the WAL peak and the universal conductance fluctuations (UCF). Sample thickness $t = 105$ nm.

Figure 6.6b shows the equivalent Hall resistance R_{xy} as a function of field vs. gate voltage. As the field strength increases the Hall voltage V_H will increase, which can be seen as an increase in R_{xy} and is anti-symmetric with respect to zero field as V_H changes sign. At zero field, R_{xy} is zero as no Hall voltage develops for zero field. Vertical linecuts can be taken at certain V_g to obtain individual traces for R_{xy} as function of magnetic field. The mobility and carrier density are extracted for a set of gate voltages so to see the evolution of these quantities as a function of gate voltage, shown for three Hall bars in figure 6.7a. Here, the Hall mobility μ can be seen as a function of gate voltage. As was mentioned earlier, the mobility is not a constant and changes as the gate voltage alters the chemical potential in the nanowire and changes the local density of states. Near saturation, the Hall mobility of all Hall bars is greater than 10 000 cm^2/(Vs), with the largest seen for Hall bar C with a value of approximately 16 000 cm^2/(Vs). As was mentioned, the carrier density is not constant but a function of the chemical potential, tuned by the gate voltage, as shown in figure 6.7b. Here the carrier density is seen increasing as the gate voltage is tuned in the positive direction. All Hall bars have carrier concentration on the order 10^{17} cm^{-3} with Hall bar B and C displaying roughly the same carrier density at equivalent gate voltage while bar A is consistently higher than these two. For equivalent gate voltage, the carrier density is seen to increase linearly, while the mobility saturates. This indicates that at saturation of the mobility, the mobility is limited by other factors such as disorder rather than carrier density.

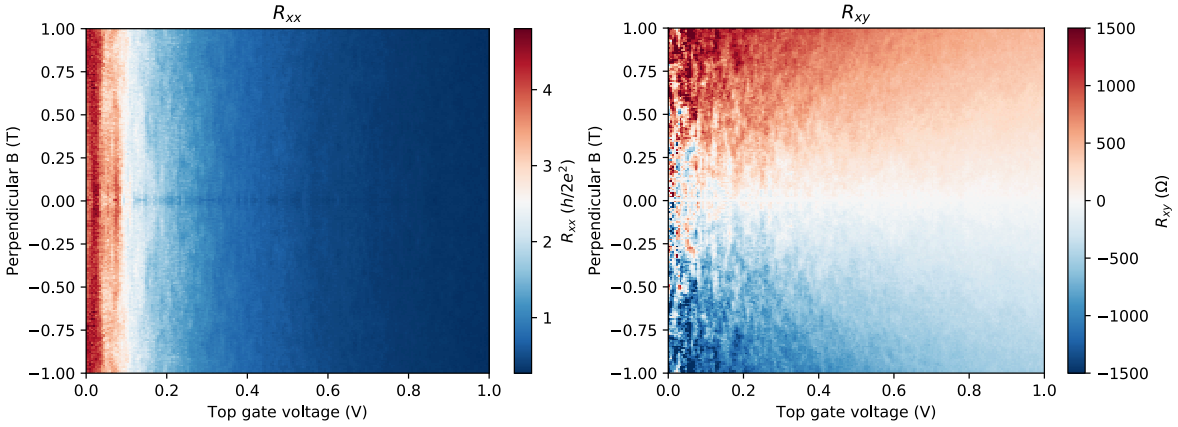

Figure 6.6: 2D field vs. gate voltage measurement results of a Hall bar on Q169. **(a)** Intrinsic resistance R_{xx}. WAL peak visible at $B = 0$. **(b)** Equivalent Hall resistance R_{xy}.

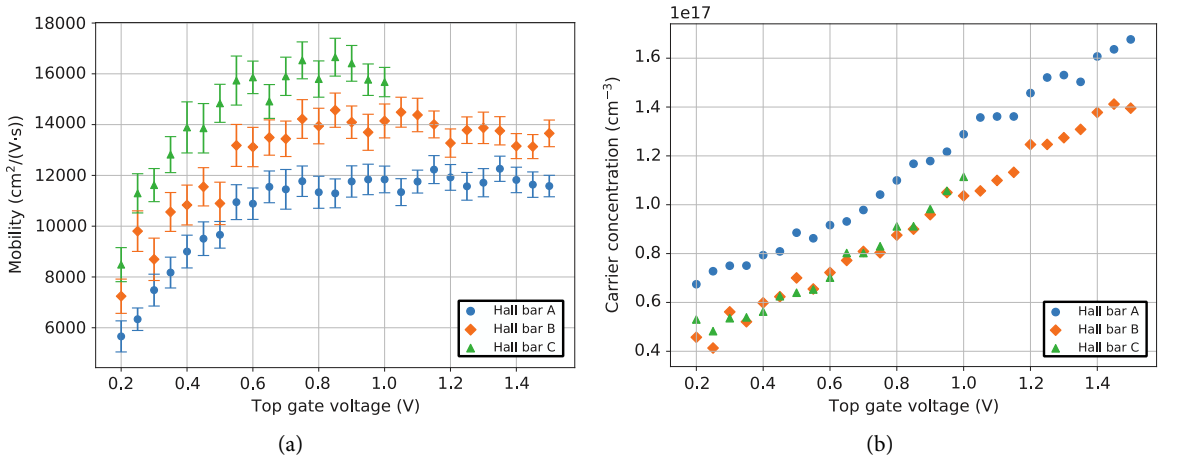

Figure 6.7: Electronic properties of three hall bars from the Q169 samples. **(a)** Mobility as function of gate voltage can be seen to saturate as gate voltage is increased. **(b)** Carrier concentration increases linearly as the gate voltage increases. Mobility saturates while carrier concentration keeps rising, indicating mobility limited by other factors such as disorder after a certain gate voltage is reached.

6.2.3. Quantum point contacts

Quantum point contacts (QPCs) are created by creating a narrow constriction in the energy landscape of the nanowire via a top gate, shown in figure 6.8 in purple. Here, a constriction of approximately 450 nm is created between two contacts, shown in gold, which locally tunes the chemical potential in the nanowire. The differential conductance of this QPC is measured using a lock-in amplifier with a sinusoidal excitation of 20 μV around zero DC bias.

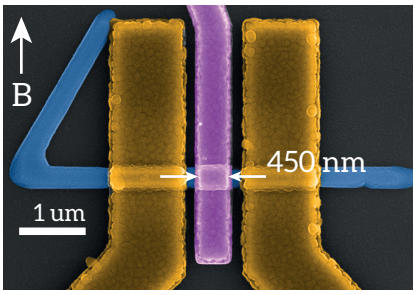

Figure 6.8: Colorized SEM image of the QPC from sample Q163. Top gate in purple. Ohmic Cr/Au contacts in gold. InSb nanowire in blue. Channel length is 450 nm.

A magnetic field of 5.5 T is applied perpendicular to the nanowire but in-plane to the substrate to reduce the effects

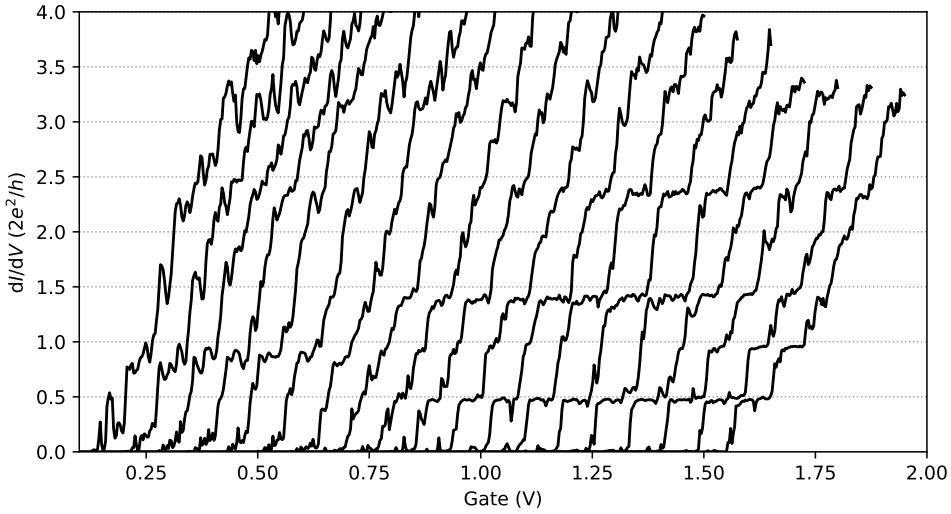

Figure 6.9: Pinch-off traces of the QPC from Q163 at for a range of magnetic values varying from 0 T to 5.4 T. Traces shifted horizontally for clarity. Conductance plateaus at half-integer multiples of G_0 appear as field is increased.

of disorder on the transport through the QPC by forcing the electrons into an edge conductance mode. Due to the small length of the constriction, the electrons are able to traverse it ballistically, giving rise to quantized conductance. This can be seen in figure 6.9. Here several pinch-off curves of the QPC can be seen, with the trace on the left taken at $B = 0$ and each subsequent trace moving to the right taken at a field increasing by 0.3 T. Gate voltages are offset by 75 mV per trace. The last trace is taken at 5.4 T. Here the half-integer G_0 conductance plateaus can be seen to appear at the trace displayed at an offset gate voltage of approximately 0.8 V, corresponding to a field strength of 3 T. Integer plateaus can be seen to join in the trace located at 1.5 V, corresponding to 5.1 T. Peaks that can be seen when the wire is already in pinch-off are most likely resonances from intrinsic quantum dots in the wire.

A 2D gate vs. bias sweep was taken of the differential conductance at 3 T, shown in figure 6.10. Series resistance is substracted in this figure. Here, diamonds can be seen appearing corresponding to the conductance plateaus. The width from center to corner in bias voltage of these diamonds corresponds to the Zeeman energy splitting between conductance channels. For the first energy splitting $\Delta E_{1\uparrow\downarrow} = \left(E_{1\uparrow} - E_{1\downarrow}\right)/e$ we find a splitting of approximately 8 meV which results in a Landé g-factor of $g = \Delta E_{1\uparrow\downarrow}/\left(\mu_B B\right) \approx 46$, with μ_B the Bohr magneton, which is similar to previous results in InSb VLS nanowires [90]. Up to the fourth diamond can be distinguished in this figure.

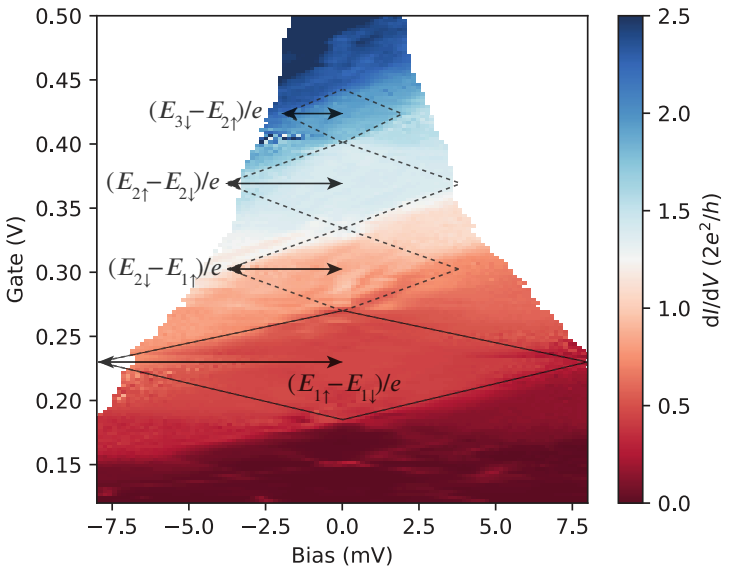

Figure 6.10: Series resistance corrected 2D gate vs. bias sweep of a QPC in InSb nanowire. Diamonds can be distinguished, drawn as dashed lines, corresponding to the conductance plateaus. Corresponding energy splitting between spin subbands shown as arrows.

Figure 6.11 shows a 2D gate vs. magnetic field sweep of the differential conductance. As the magnetic field increases, regions become easier to resolve, corresponding to the conductance plateaus. Drawn in this figure are dashed lines separating the regions as a visual aid. Plateau values in units of G_0 are written in the regions. Zeeman split subbands can be seen merging as the magnetic field is swept. At low finite field (< 2 T) half-integer plateaus are likely to be obscured due to mesoscopic flutuations, which can be attributed to backscattering at the contacts, the long transport region compared to the mean free path and the transport region not being completely covered by the top gate. As can be seen from this figure the plateau at 1.0 G_0 is very narrow around 3 T, which can be compared to the pinch-off trace of figure 6.9 for verification. This plateau does not reappear until the field is near 5 T, indicating that for low magnetic fields, the disorder is too large for this plateau to be clearly distinguished due to bulk disorder and that in the process of moving towards high field, the spin-up subband with energy $E_{1\uparrow}$ crosses with the spin-down subband with energy $E_{2\downarrow}$, narrowing the plateau and obscuring it.

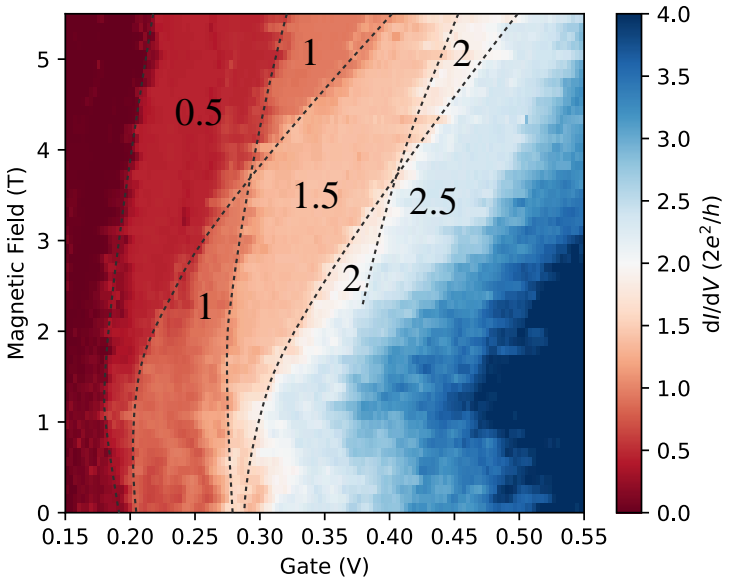

Figure 6.11: 2D gate vs. field sweep of a QPC in InSb nanowire.

6.2.4. Aharonov-Bohm loops

InSb SAG nanowires grown in loop structures were measured and Aharonov-Bohm oscillations were observed. Figure 6.12 shows a typical device. A magnetic field perpendicular to the substrate is swept such that AB-oscillations can be measured using a lock-in amplifier with a 20 μV sinusoidal excitation at 0 bias voltage.

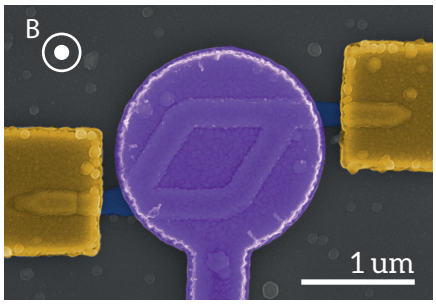

Figure 6.12: Colorized SEM image of one of the Aharonov-Bohm loops on Q169. Circular top gate shown in purple. Ohmic Cr/Au contacts in gold. Nanowire in blue. Magnetic field perpendicular to the substrate.

Two AB-loops with varying cross-sections were measured, as can be seen in figure 6.13. Here, two magnetoconductance oscillations are seen for two devices, one with an area estimated to be 0.69 μm^2, the other 3.25 μm^2. These traces were obtained by sweeping through a range in magnetic field and measuring the magnetoconductance. The UCF background is substracted by averaging over a large window, assuming the UCF-oscillations have a much longer period in magnetic field than the AB-oscillations. This will average out the AB-oscillations, leaving with only a trace of the UCF.

This is then subtracted from the original data to remove the effect of the UCF from the measurement data. The device with an area of 3.25 μm^2 has a broken gate and thus we were unable to tune it to a stable regime in gate space, making phase coherence length measurements unreliable, although we were able to see AB-oscillations in magnetoconductance.

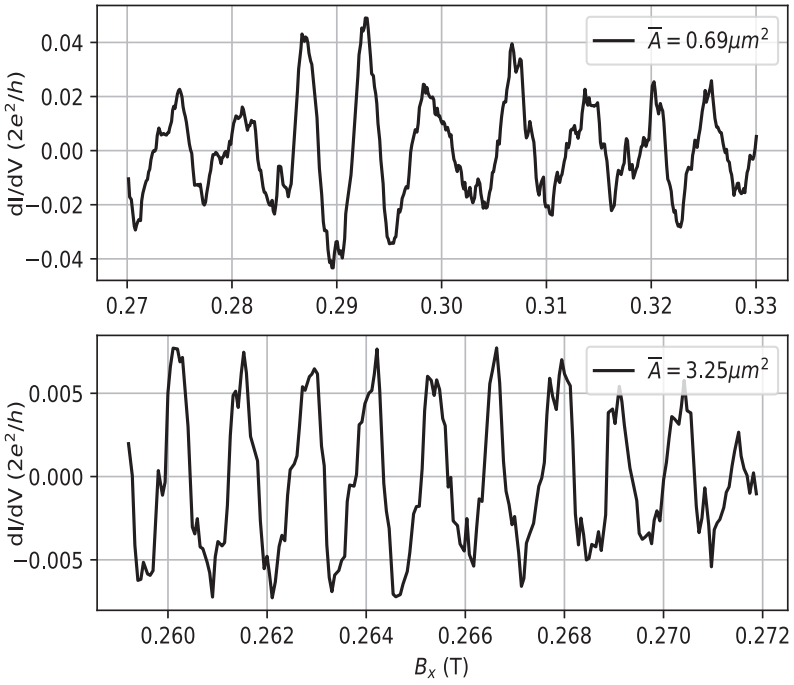

Figure 6.13: Aharonov-Bohm oscillations after background subtraction from SAG nanowire loop structure of sample Q169 1700. **Top:** Small loop with an mid-section area of 0.69 μm^2. **Bottom:** Larger loop with a mid-section area of 3.25 μm^2.

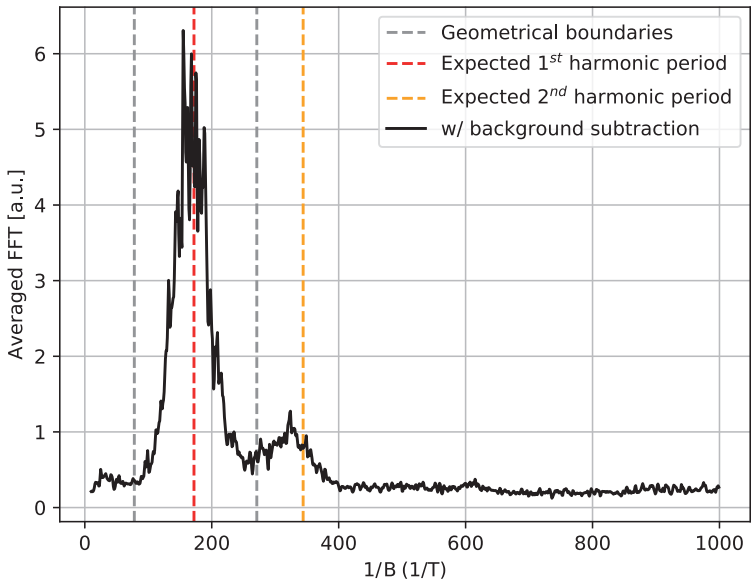

Figure 6.14: Result of averaging the UCF background subtracted FFT traces of individual field sweeps at different temperatures. Two peaks can be clearly distinguished. Dashed vertical lines are drawn according to periodicity estimates from geometry, with red and orange being estimates of the first and second harmonic respectively. Grey dashed vertical lines indicate period estimates based on area estimates along the inner and outer perimeter of the loop, in between which the first harmonic is expected to be found.

Periodicity of the AB-conductance fluctuations is estimated by taking a Fast Fourier Transform (FFT) of the back-

ground subtracted data at different temperatures. The spectra are then averaged to reduce the statistical uncertainty. Area estimates are done by inspection from SEM images. We expect the wavelength of the harmonics of the magneto-conductance in magnetic field-space to appear as integer multiples of $\Delta B = \Phi_0/A$, with $\Phi_0 = h/e$ the magnetic flux quantum. A full oscillation is expected to be observed when exactly a single flux quantum threads the loop. The averaged FFT of the device with an area of $0.69\ \mu m^2$ is shown in figure 6.14. Harmonic estimates $1/\Delta B$ from inspection of the SEM images taken through the center of the nanowire is shown as the red vertical dashed line and the second harmonic $2/\Delta B$ as the orange dashed vertical line, with $\Delta B = 5.96$ mT being the periodicity in magnetic field. These show reasonably good correspondence with the peaks from the averaged FFT. Grey dashed lines are periodicity estimates based on area estimates by going over the inner and outer perimeter of the loops (rather than through the center of the nanowire) and thus are under and over estimates, respectively. As expected, the first harmonic peak falls within these grey lines.

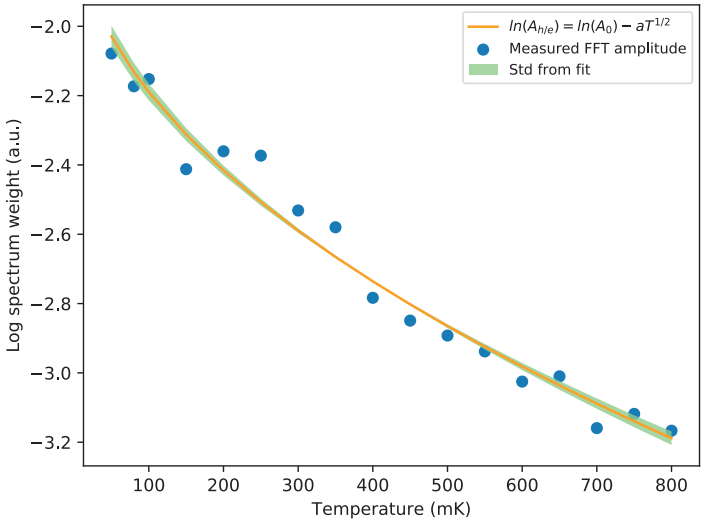

Figure 6.15: Phase coherence length extracted from FFT amplitudes of traces taken at different temperatures. Model fitted with an amplitude dependence $\propto \exp(T^{1/2})$. Fit uncertainty in green.

Phase coherence length estimates can be extracted from temperature dependence traces, as shown in figure 6.15. Here, a phase coherence length dependence $L_\phi \propto T^{-1/2}$ is assumed such that the amplitude of the AB-oscillations scales as $A_{h/e} = A_0 \exp\left(-L/L_\phi\right)$ with $L_\phi = L/\left(aT^{1/2}\right)$ ([46, 91]) where a and L_ϕ are fit parameters. The fit is shown as the orange trace with the fit uncertainty in green. The fitted phase coherence length is extracted as $L_\phi \approx 10.4\ \mu m$ at 50 mK. Temperature dependence of the phase coherence length using the fit parameters obtained is shown in figure 6.15.

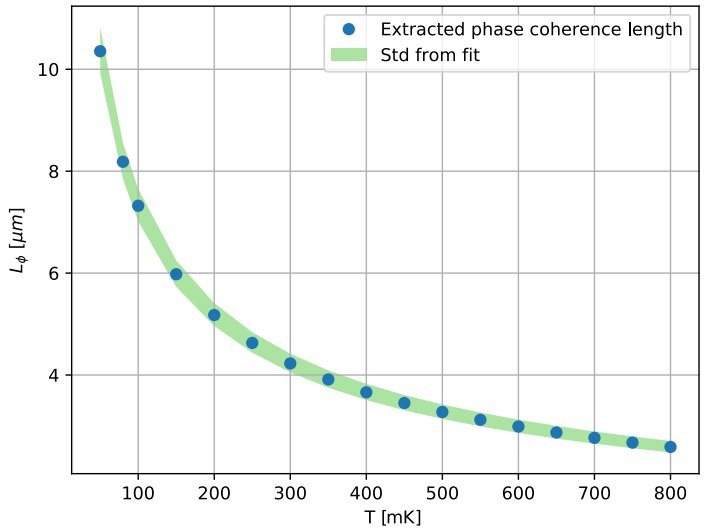

Figure 6.16: Phase coherence length as function of temperature plotted using the fit parameters obtained from the fit in figure 6.15.

6.2.5. Quantum Dots

Trapping of electrons can be done using quantum dots. The ability to create quanum dots and is important for the future development of superconducting islands, used in the qubit proposals discussed before. An island is created in the nanowire by separating an area of the nanowire from the rest of the nanowire in the energy landscape using two cutter gates, tuned close to pinch-off. This will trap charges onto the island. In order to add an electron to the island, an additional amount of energy has to be paid to overcome the Coulomb blockade. Figure 6.17 shows such an island device.

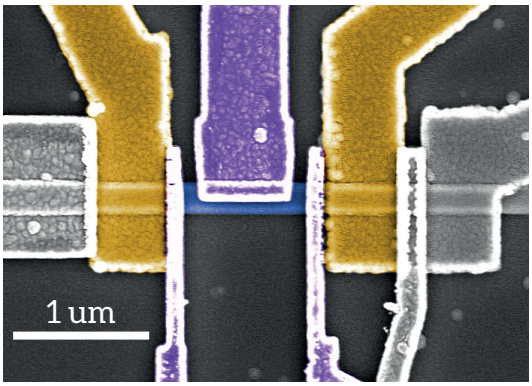

Figure 6.17: Quantum dot created in the nanowire using two cutter gates, shown in purple. A top gate (center) tunes the chemical potential of the dot. Ohmic Cr/Au contacts in gold. Nanowire uncovered by metal in blue. This particular device shares its nanowire with an FEM and a QPC device (leads not colorized).

A 2D map of the cutter gate space is made by measuring the conductance as a sweep of cutter gate 1 vs. cutter gate 2, and a location is found where both cutter gates are very close to pinch-off, shown in figure 6.18. This is necessary to restrict the access of the electrons to the island. In this particular case, suitable values for the gate voltages are $V_{\mathrm{TG1}} = -370$ mV and $V_{\mathrm{TG2}} = -600$ mV.

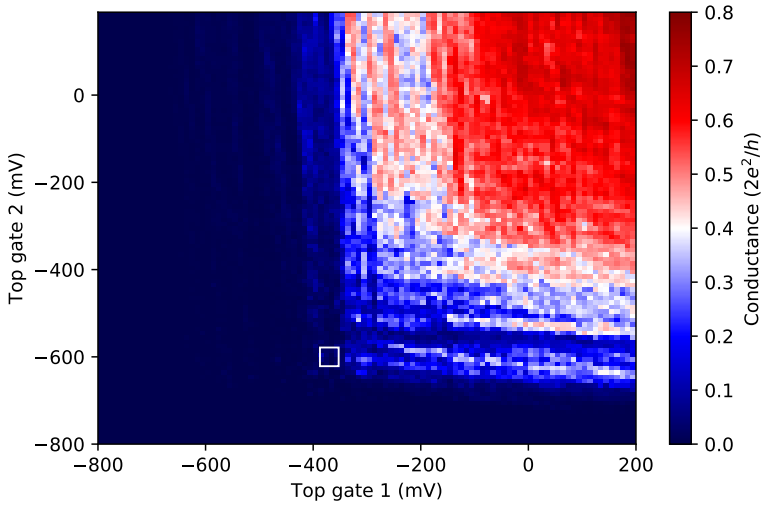

Figure 6.18: 2D map of the conductance in cutter gate space. A location indicted by the white square is found such that both cutters are close to pinch-off.

By tuning the cutter gates to these values, we can control the number of electrons on the island by tuning the chemical potential using the plunger gate. This is shown in figure 6.19 as Coulomb peaks. Each peak corresponds to the addition of an electron to the island. Ideally, the conductance would be zero in between, however as can be seen from the figure, this is not always the case. This can be attributed to the peak width in plunger gate space being wide enough as to overlap with its neighboring peaks, creating an apparent offset in conductance.

By taking a 2D sweep of plunger vs. bias voltage at these cutter gate values, we obtain Coulomb diamonds, shown in figure 6.20. These diamonds should be symmetric with respect to zero bias, however in this case they are asymmetric.

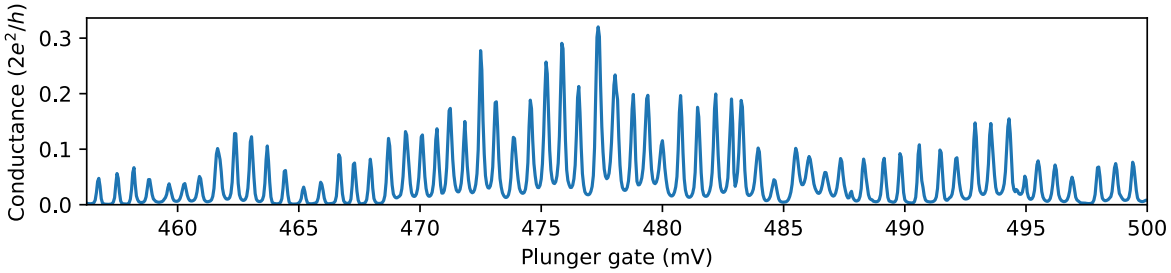

Figure 6.19: Coulomb peaks appear as we sweep V_{PG} corresponding to the addition of an electron to the island each time a peak appears.

This can be attributed to the asymmetric bias that is applied. The charging levels in number of electrons is shown with respect to N, with N being the number of charges on the island for the diamond drawn in dashed lines for illustration purposes. The plunger gate is swept in the range of 490 mV to 494 mV (refer also to figure 6.19). The charging energy is estimated to be $E_C \approx 250\ \mu eV$ which gives for the total capacitance $C_\Sigma = e^2/E_C \approx 0.64$ fF.

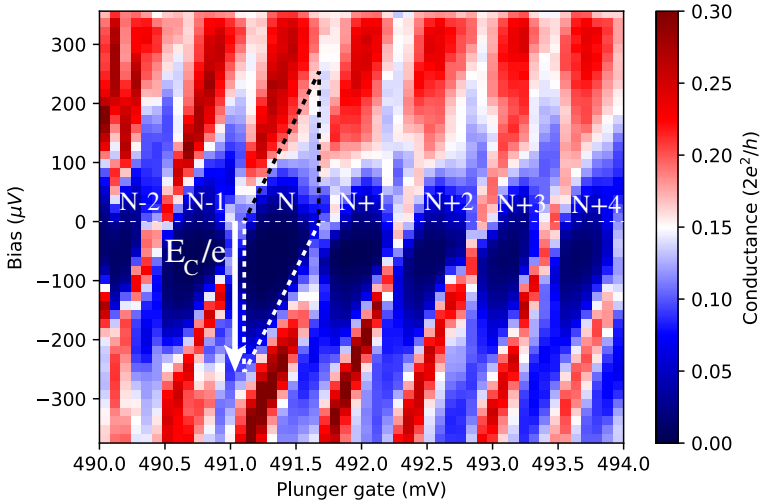

Figure 6.20: Coulomb diamonds when sweeping plunger gate vs. bias voltage while measuring the conductance. One of the diamonds has been drawn with dashed lines as visual aid. The charging energy E_C is indicated by the arrow.

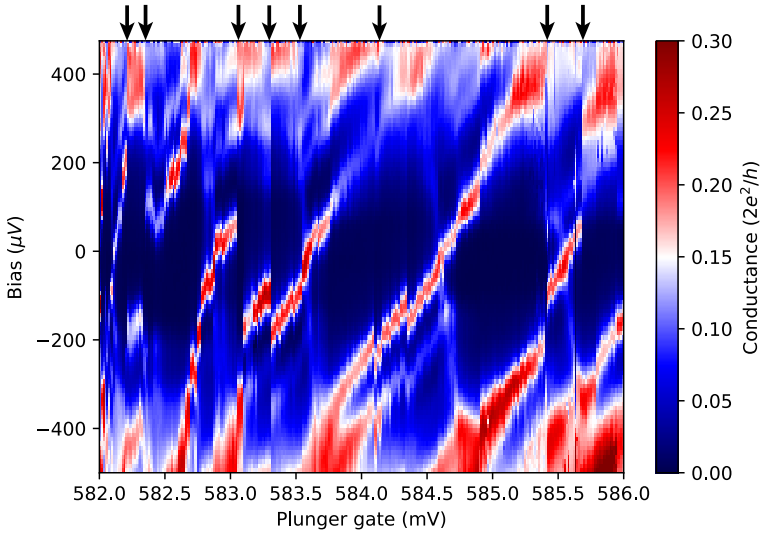

Figure 6.21: Unstable gates and charge jumps can cause the Coulomb diamonds to jump and shift. Most prominent jumps indicated by arrows. Making reliable estimates can be difficult in these cases, as every apparent diamond experiences jumps.

When sweeping the plunger gate, instabilities in gate voltage or charge jumps elsewhere on the sample can cause the local electric field environment to change, causing jumps in the Coulomb diamonds. This can be seen in another island we measured, shown in figure 6.21. These jumps make estimation of E_C and other parameters considerably more difficult. Charge traps in the dielectric close to the plunger gate will have the most effect on this, as these charge traps can empty or fill themselves depending on the gate voltage and the direction it is swept in.

6.3. Indium-Antimonide plus Aluminium

To create Majorana bound states, we need to induce superconductivity in the strong-spin orbit coupled InSb nanowires. A thin aluminium film is deposited on the sample at an angle, covering one side the nanowires. A selective aluminium deposition technique was used, such that etching on the nanowires is not necessary, and instead PMMA windows were placed over the nanowires to protect the aluminium thin film covering them against the etching.

6.3.1. First signs of superconductivity

Normal-Nanowire-Superconducting (N-NW-S) junctions were measured via tunnel spectroscopy. For this sample, gates were not bonded due to difficulty bonding to the gate bondpads. Therefore, the fact that we even see a gap appear without control over the gates must be because of an intrinsic barrier in this nanowire close to the contacts. Figure 6.22 shows the N-NW-S device measured here. A defect in the wire is indicated by an arrow. This defect might be the cause of the constriction needed to see the superconducting gap without control of the gate.

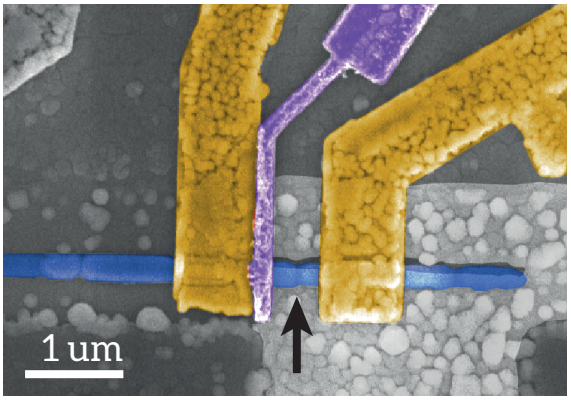

Figure 6.22: Colorized SEM image of an N-NW-S device. Tunnel gate (not connected) in purple, Cr/Au contacts in gold. Nanowire not covered by metal in blue. Defect indicated by arrow. Aluminium in grey.

Figure 6.23 shows a 2D bias vs. field sweep of the N-NW-S junction using the lock-in amplifier with a sinusoidal excitation of 5 μV while measuring the conductance. The magnetic field is applied here parallel to the wire. The gap can be seen to close as magnetic field intensity increases, with a critical field of approximately $B_c \approx 0.5$ T. As can be seen from the linecut at $B = 0$ T in the upper panel, from visual inspection the width of the gap corresponds to the superconducting gap energy Δ of thin film aluminium which is on the order of 200 μeV. The Dynes DOS model for quasiparticle broadening is fitted to the linetrace. This model assumes the energy has an overall complex component and transforms the BCS DOS via the transformation $E \rightarrow E - i\Gamma$. A side effect of this transformation is that the Dynes DOS does not go to zero in the gap, but a non-zero quasiparticle spectrum is predicted everywhere in the gap. The model also assumes that $T = 0$ K, which is however not the case (the electron temperature in the dilution fridge is around 50 mK) and this assumption will also cause a finite broadening. The fit parameters obtained from the model are a quasiparticle lifetime broadening $\Gamma = 0.1\Delta$, above-gap conductance of $G_N = 4.1 \cdot 10^{-3} G_0$ and superconducting order parameter $\Delta = 243$ μeV. The fit model also accounts for a constant offset in bias voltage. The conductance in general is very low, which can be accounted for by considering that the nanowire is most likely very close to pinchoff due to the non-functioning gate. The large amount of noise can be reduced by increasing the lock-in amplifier excitation voltage, which has been done in figure 6.25 by increasing the sinusoidal excitation to 10 μV. Here, the gap can be seen much clearer in the linecut preceding the 2D map. Again, the Dynes DOS is fitted to this linecut. Parameters extracted are $\Gamma = 0.07\Delta$, $G_N = 3.8 \cdot 10^{-3} G_0$ and $\Delta = 239$ μeV. In the 2D map, the gap can be seen to close as magnetic field intensity increases. The field here is aligned perpendicularly to the substrate and the nanowire. The critical field is much less than when the field was aligned parallel to the nanowire, $B_c \approx 0.11$ T. This can be explained by the larger flux per unit surface area that needs to be expelled by the superconducting thin film via the Meissner effect for this field orientation, resulting in larger supercurrents which cause the critical current I_c to be induced at lower field. The values for the superconducting

gap parameter Δ correspond well with experimental results for thin film aluminium obtained by [92].

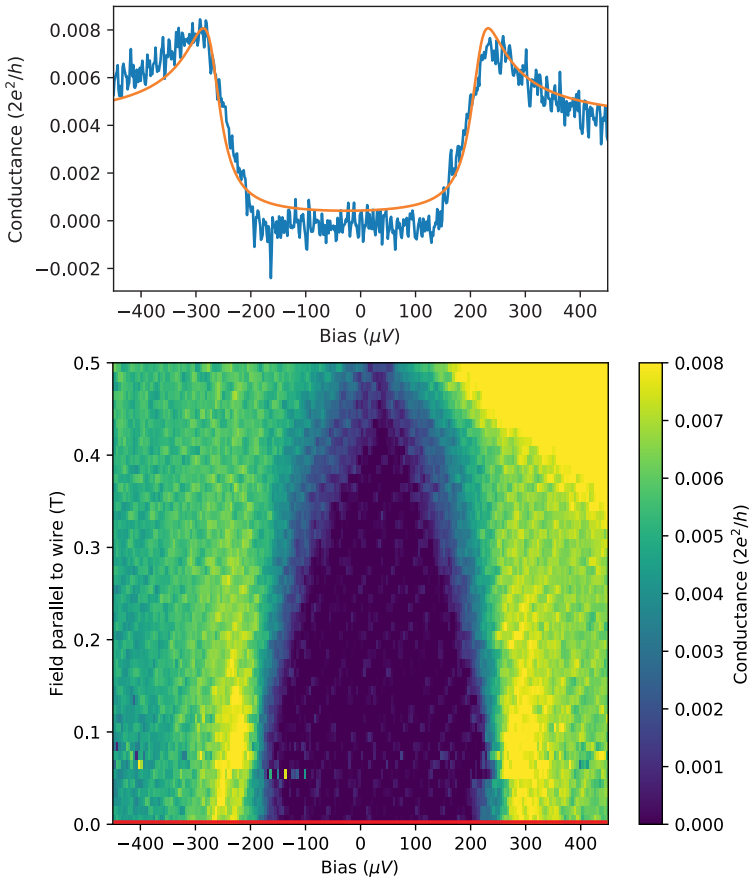

Figure 6.23: 2D bias vs. field sweep while measuring conductance. Magnetic field applied parallel to the nanowire. The superconducting gap can be seen closing at $B_c \approx 0.5$ T. A linecut at $B = 0$ T can be seen above the 2D map (red line). The Dynes DOS is fitted to the data.

Temperature dependence of the gap was done by sweeping the temperature over a range from 50 mK to 1200 mK and performing tunnel spectroscopy at each intermittent temperature. The resulting 2D map can be seen in figure 6.24. From looking at the gap closing we can conclude that for the critical temperature $T_c \approx 1100$ mK, which is in good correspondence with the bulk value [93].

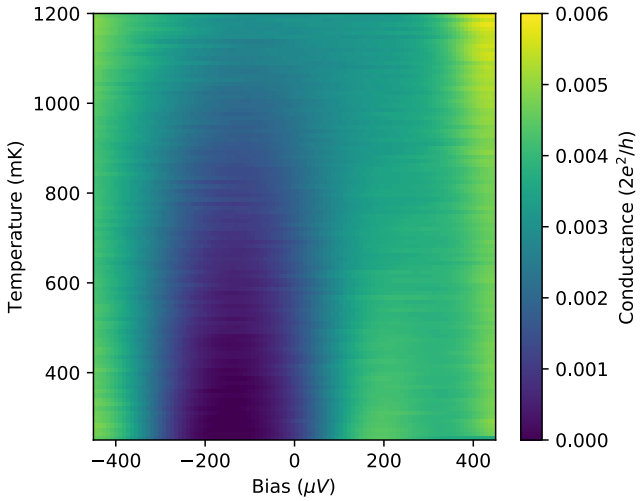

Figure 6.24: Temperature dependence of the superconducting thin aluminium film. T_c is found to be approximately 1100 mK.

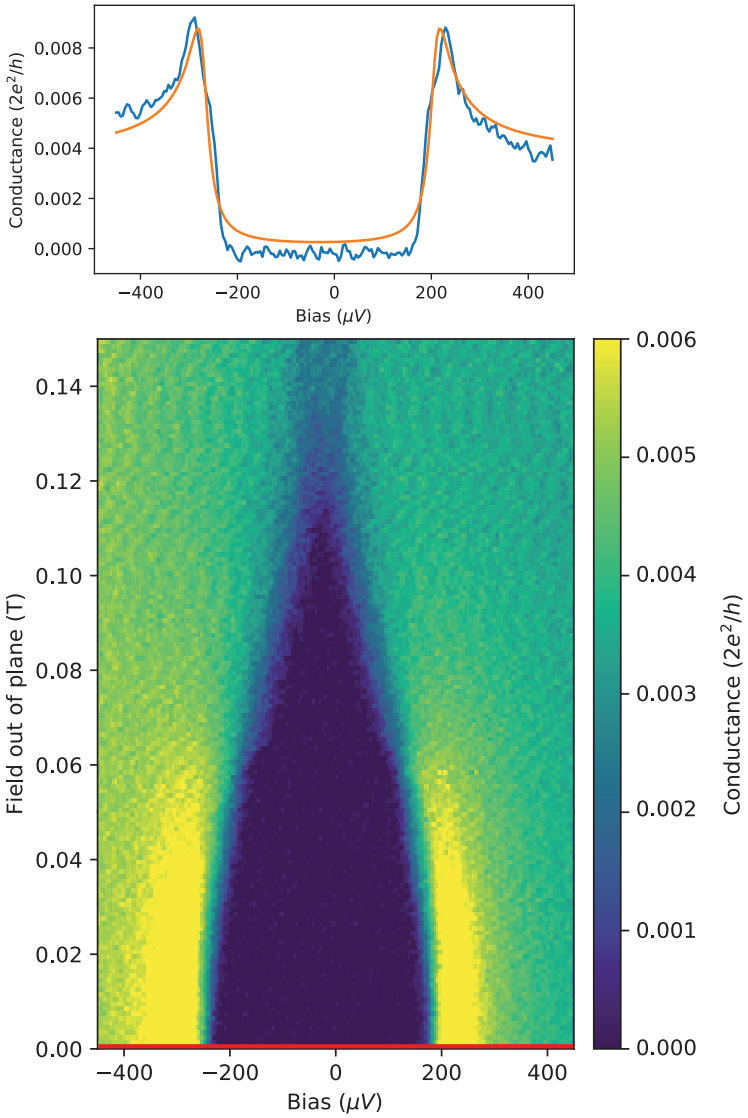

Figure 6.25: 2D bias vs. field sweep while measuring conductance. Magnetic field applied perpendicular to the substrate. The superconducting gap can be seen closing at $B_c \approx 0.11$ T. A linecut at $B = 0$ T can be seen above the 2D map (red line). The Dynes DOS is fitted to the data.

From these results it cannot be concluded whether this method of depositing thin film aluminium will allow us to produce the hard gaps [94] needed to protect our MBS residing at zero bias from quasiparticle poisoning. This is mainly because the out-of-gap conductance G_N is so low for this sample. More work needs to be done on characterizing the aluminium film to either rule out or confirm the existence of a hard gap.

7

Conclusion and outlook

7.1. Conclusion

Scalability is going to be an important factor when creating a topological quantum computer. Growth techniques that have been used to make nanowires in which zero-bias peaks have been observed, a hallmark feature of Majoranas, are difficult to scale up. Selective area growth attempts to provide an answer to the need of a platform with which nanowires can be grown that is easier to scale. In this work, the transport properties of InAs and InSb SAG nanowires have been probed.

We found that the FEM of InSb SAG nanowires are much larger than those of InAs SAG nanowires grown in the same MBE chamber. The FEMs do not change significantly between equivalent crystal orientations or widths of the nanowires and show good reproducibility. Hall mobilities are consistently higher than FEM, indicating the method to determine the FEM might be limited by the quality of the value of the capacitance obtained from simulation.

The measured QPC shows that ballistic transport in InSb SAG can be achieved in channels of almost half a micron, owing to high crystal quality. The Aharonov-Bohm measurements also show phase coherent transport over distances of approximately 10 micron and visibility of up to the second harmonic of the magnetoconductance, indicating high junction quality in the SAG loops.

The ability to create quantum dots is important for future efforts to realize the Majorana box qubit and tetron/hexon qubit proposals [72, 73], as superconducting islands need to be realized. We have observed Coulomb blockade, indicative of our control over the gates and the isolation of the quantum dot region. Gate jumps observed in some quantum dots might be caused by charges jumping elsewhere on the sample or unstable gates due to dielectric quality.

The first tests with N-S spectroscopy of epitaxial aluminium show signs of superconductivity and values for the superconducting gap parameter, critical temperature and critical field which correspond to the literature values for thin film aluminium, showing we can produce indeed the needed superconducting film needed to proximitize the nanowires.

With these results in hand, InSb SAG grown by MBE in Delft shows it is becoming a promising new platform for fabricating InSb nanowires in arbitrary shapes and sizes. These new developments open the door to more interesting experiments difficult or even impossible to realize in competing techniques such as VLS, and allow us to continue progressing towards the Majorana qubit proposals.

7.2. Outlook

The results obtained in this work can be regarded as only the first steps towards developing a scalable platform for topological quantum computing. Much work still needs to be done. The following points are suggestions addressing several issues and what work can be done to improve on them.

- Even though the quality of the wires is high, the yield of the growth still varies. A higher yield will allow for deterministic placement of devices, rather than placing each device manually after inspection under SEM. More growth optimization and characterization needs to be done to improve the SAG growth yield.
- Scaling up can be aided by the use of scripted CAD and autorouting. The current implementation of autorouting works, but is still rudimentary. The implementation of faster, more efficient algorithms that can also dynamically change the routes as to accommodate for routing conflicts has the potential to save a lot of time and reduce the chip design turnaround time. Increased activity in this direction could lead to a more efficient way of designing quantum structures in general.

- More characterizing work for the epitaxial aluminium needs to be done. The first results are promising, but more statistics are needed to draw any clear conclusions on film quality and gap hardness. A trivial to topological transition has still to be observed in epitaxial aluminium from the InSb SAG. Ultimately, this should lead to similar observations of zero-bias peaks as was the case for VLS nanowires [74].
- Faster measurements can be done if the DC measurement techniques used in this work are replaced by much fast RF techniques. Nanowires can be connected in series with a resonator on chip, effectively multiplexing their response to an applied signal in frequency space. So called RF conductance measurements could then be performed at a much higher rate when compared to DC techniques. This could also mitigate gate instabilities because the time-window of a single trace is greatly reduced in such a measurement.
- Majorana zero-bias peaks still have to be observed in InSb SAG nanowires. Therefore future work could focus its efforts on attempting to observe these hallmark features of Majoranas. Non-locality of the Majoranas could also be attempted to be probed.
- It might be that the gap closes and reopens in the bulk, causing a trivial-topological transition to take place also in the bulk rather than just at the ends of the nanowire owing to disorder in the nanowire. In order to figure out whether this is actually the case, proposals have been made [95] to investigate the bulk gap by means of multiprobe Majorana nanowires. In such a setup, tunnel probes are placed along the wire and tunnel spectroscopy is performed, revealing the nature of the gap in the bulk of the nanowire, see figure 7.1.

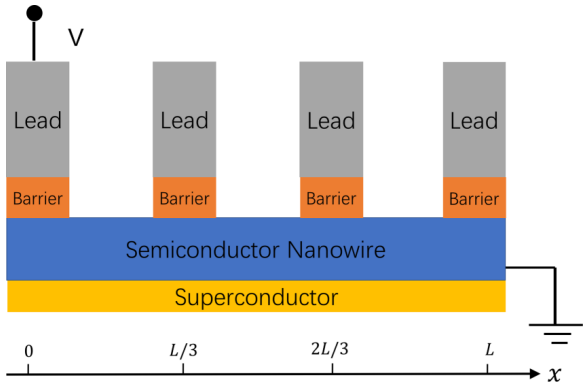

Figure 7.1: Schematic of the multiprobe setup. Leads contact the semiconductor nanowire at $x \in \{0, L/3, 2L/3, L\}$ and tunnel barriers are applied near the nanowire. Using tunnel spectroscopy the gap in the bulk of the nanowire can be probed. Image from [95].

Such a multiprobe nanowire could be fabricated with relative ease using the SAG growth method. One of the concerns laid out by the authors of the proposal is the invasive nature of the tunnel probes, where the metal contacts themselves introduce local potential fluctuations in the nanowire. Such (invasive) experiments have already been done with InAs VLS nanowires [96]. With SAG however, the legs extending from the main nanowire can be part of one and the same crystal structure, which would reduce the effects of any metallic contacts used for the leads of the legs.

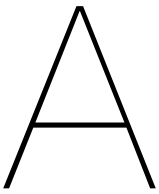

Autorouting script

```python
#!/usr/bin/python3
import json
import numpy as np
import gdspy as gd
import gds_tools as gtools
from operator import add, sub

debug = False

# Import mask file from Alexandra
fp = '../CAD/Delft_SAG_mask_v09_001_only_markers_border.gds'
lib = gd.GdsLibrary()
lib.read_gds(fp)
c = lib.extract('TOP')

# Load locations file
locs = open(fp + '.locations.json', 'r').read()
locs = json.loads(locs)

# Generate bondpads
bondpad_ep = 'B'
r = (100, 150)
dx_top = 175
nx_top = 16
pads = gtools.pads.tri_array(r, dx_top, nx_top, shape = 'square', layer = 15)
gtools.add(c, [*pads[0], *pads[1], *pads[2], *pads[3]])

[pads_T, pads_R, pads_B, pads_L] = pads

# Prove that we have found all the endpoints
if debug:
    for x, col in enumerate(locs['grid']):
        for y, row in enumerate(col):
            if row != 0:
                for ends in locs['grid'][x][y]['ends']:
                    for e in ends:
                        circ = gtools.geometry.circle(1).mov(ends[e])
                        gtools.add(c, circ)

# Generate gridpoints of the bottom left corner of each grid cell
n_grid = int(locs['frame_size'] / locs['grid_size'])
x_grid = np.linspace(-locs['frame_size'] / 2, locs['frame_size'] / 2, n_grid + 1).tolist()
y_grid = x_grid

# Create vias to get transmission lines from bondpads going
a_via = 1
n_via = 6
via_d = 1350
via_T = gtools.markers.square(a_via, spacing = dx_top / 2, pattern = [[1, 1, 1, 0] * 8], layer = 25).mov([-a_via/2]
 ↪  * 2).mov((pads[0][0].endpoints[bondpad_ep][0], via_d))
```

```
via_R = via_T.copy().rot(-np.pi/2)
via_B = via_R.copy().rot(-np.pi/2)
via_L = via_B.copy().rot(-np.pi/2)

bond_vias = [via_T, via_R, via_B, via_L]
if debug:
    gtools.add(c, bond_vias)

# Draw lines from bondpads
bondline_width = 10
bondlines = []
for vi, bv in enumerate(bond_vias):
    for i in range(0, len(bv.endpoints)):

        delta = tuple(map(sub, bv.endpoints['MARKER_' + gtools.alphabet[i]], pads[vi][i].endpoints[bondpad_ep]))
        line = gtools.transmission.line(delta, bondline_width).con('A', pads[vi][i], bondpad_ep)
        bondlines.append(line)

gtools.add(c, bondlines)

# Define which wires you want to connect
first_wire_index = 0
last_wire_index = 3
n_wires = last_wire_index - first_wire_index + 1

# Create vias right next to grid
n_via = n_wires + 2
divider = n_via + 1
spacing = locs['grid_size'] / divider
grid_via_T = gtools.markers.square(a_via, spacing = spacing, pattern = [([1] * n_via + [0] * (divider - n_via)) *
 ↪  n_grid], layer = 25).mov((x_grid[0] + locs['grid_size'] / 2 - spacing * (n_via - 1) / 2, y_grid[-1] + 2 *
 ↪  spacing))
grid_via_R = grid_via_T.copy().rot(-np.pi/2)
grid_via_B = grid_via_R.copy().rot(-np.pi/2)
grid_via_L = grid_via_B.copy().rot(-np.pi/2)

if debug:
    gtools.add(c, [grid_via_T, grid_via_R, grid_via_B, grid_via_L])

# Define mapping between grid cells, bondpads and vias
mapping = [{
            'cell': (1, 2), 'pad_block': pads_L, 'pad_group': 0, 'via_block': grid_via_L, 'via_group': 1
        },{
            'cell': (2, 5), 'pad_block': pads_B, 'pad_group': 2, 'via_block': grid_via_B, 'via_group': 12
        },{
            'cell': (2, 1), 'pad_block': pads_B, 'pad_group': 3, 'via_block': grid_via_B, 'via_group': 13
        },{
            'cell': (9, 1), 'pad_block': pads_B, 'pad_group': 1, 'via_block': grid_via_B, 'via_group': 6
        },{
            'cell': (10, 1), 'pad_block': pads_B, 'pad_group': 0, 'via_block': grid_via_B, 'via_group': 4
        },{
            'cell': (14, 14), 'pad_block': pads_R, 'pad_group': 0, 'via_block': grid_via_R, 'via_group': 0
        },{
            'cell': (1, 6), 'pad_block': pads_L, 'pad_group': 1, 'via_block': grid_via_L, 'via_group': 4
        },{
            'cell': (1, 10), 'pad_block': pads_L, 'pad_group': 2, 'via_block': grid_via_L, 'via_group': 9
        },{
            'cell': (1, 13), 'pad_block': pads_L, 'pad_group': 3, 'via_block': grid_via_L, 'via_group': 12
        },{
            'cell': (2, 14), 'pad_block': pads_T, 'pad_group': 0, 'via_block': grid_via_T, 'via_group': 2
        },{
            'cell': (9, 10), 'pad_block': pads_T, 'pad_group': 1, 'via_block': grid_via_T, 'via_group': 8
        },{
            'cell': (10, 14), 'pad_block': pads_T, 'pad_group': 2, 'via_block': grid_via_T, 'via_group': 10
        },{
            'cell': (13, 13), 'pad_block': pads_T, 'pad_group': 3, 'via_block': grid_via_T, 'via_group': 12
        },{
            'cell': (14, 6), 'pad_block': pads_R, 'pad_group': 1, 'via_block': grid_via_R, 'via_group': 7
        },{
            'cell': (14, 5), 'pad_block': pads_R, 'pad_group': 2, 'via_block': grid_via_R, 'via_group': 10
```

```
        },{
           'cell': (10, 2), 'pad_block': pads_R, 'pad_group': 3, 'via_block': grid_via_R, 'via_group': 12
        }]

# Draw sources/gate/drain on wires in a cell and hook everything up
connector_layer = 23
via_width = 1
border_points = 20
grid_size = 5
precision = 5
for m in mapping:

    cell_index = m['cell']
    cell = locs['grid'][cell_index[0]][cell_index[1]]

    if cell['name'] == 'wires':
        connector = gtools.connectors.nanowire_sgd(cell, first_wire_index, last_wire_index, layer =
         ↪  connector_layer, gate_layer = connector_layer + 8)
        gtools.add(c, connector)
    else:
        print('>> Unknown device in cell ' + str(cell_index) + ', skipping connection steps.')
        continue; # skip iteration

    pad_ends = range(m['pad_group'] * n_via, (m['pad_group'] + 1) * n_via)
    via_ends = range(m['via_group'] * n_via, (m['via_group'] + 1) * n_via)

    for i, e in enumerate(connector.endpoints):

        this_layer = connector_layer + 25 if e[0:4] == 'GATE' else connector_layer + 20

        # Change bondpad layers
        m['pad_block'][pad_ends[i]].next[bondpad_ep].structure.layers = [this_layer]
        m['pad_block'][pad_ends[i]].structure.layer = this_layer
        m['pad_block'][pad_ends[i]].next[bondpad_ep].heal('A')

        # Connect pad to via
        via_ep = 'MARKER_' + gtools.alphabet[via_ends[i]]
        delta = tuple(map(sub, m['via_block'].endpoints[via_ep],
         ↪  m['pad_block'][pad_ends[i]].next[bondpad_ep].endpoints['B']))
        tline = gtools.transmission.line(delta, bondline_width, width_end = via_width, layer = this_layer).con('A',
         ↪  m['pad_block'][pad_ends[i]].next[bondpad_ep], 'B').heal('A')
        gtools.add(c, tline)

        # Autoroute from via to connector endpoints
        route = gtools.transmission.router(c, m['via_block'], via_ep, connector, e, via_width, border_points, layer
         ↪  = this_layer, uniform_width = True, grid_s = grid_size, precision = precision, pref = 'x' if
         ↪  m['via_block'] in (grid_via_T, grid_via_B) else 'y')
        if route:
            gtools.add(c, route.heal('A').heal('B'))

gtools.save(c, 'autorouted.gds')
gd.LayoutViewer()
```

Bibliography

[1] K. L. Brown, W. J. Munro, and V. M. Kendon, "Using quantum computers for quantum simulation," *Entropy*, vol. 12, no. 11, pp. 2268–2307, 2010.

[2] C. H. Bennett, F. Bessette, G. Brassard, L. Salvail, and J. Smolin, "Experimental quantum cryptography," *Journal of cryptology*, vol. 5, no. 1, pp. 3–28, 1992.

[3] N. Gisin, G. Ribordy, W. Tittel, and H. Zbinden, "Quantum cryptography," *Reviews of modern physics*, vol. 74, no. 1, p. 145, 2002.

[4] I. Kassal, J. D. Whitfield, A. Perdomo-Ortiz, M.-H. Yung, and A. Aspuru-Guzik, "Simulating chemistry using quantum computers," *Annual review of physical chemistry*, vol. 62, pp. 185–207, 2011.

[5] S. McArdle, S. Endo, A. Aspuru-Guzik, S. Benjamin, and X. Yuan, "Quantum computational chemistry," *arXiv preprint arXiv:1808.10402*, 2018.

[6] S. Wehner, D. Elkouss, and R. Hanson, "Quantum internet: A vision for the road ahead," *Science*, vol. 362, no. 6412, p. eaam9288, 2018.

[7] S. Jordan, *Quantum Algorithm Zoo*. National Institute of Standards and Technology (NIST), 2018. URL: `https://math.nist.gov/quantum/zoo/`, viewed on 8 December 2018.

[8] D. P. DiVincenzo, "Quantum computation," *Science*, vol. 270, no. 5234, pp. 255–261, 1995.

[9] C. H. Bennett and D. P. DiVincenzo, "Quantum information and computation," *Nature*, vol. 404, no. 6775, p. 247, 2000.

[10] M. Nielsen, M. Nielsen, and I. Chuang, *Quantum Computation and Quantum Information*. Cambridge Series on Information and the Natural Sciences, Cambridge University Press, 2000.

[11] L. H. Kauffman, *Knot logic and topological quantum computing with Majorana fermions*, p. 223–336. Lecture Notes in Logic, Cambridge University Press, 2016.

[12] C. Nayak, S. H. Simon, A. Stern, M. Freedman, and S. Das Sarma, "Non-abelian anyons and topological quantum computation," *Rev. Mod. Phys.*, vol. 80, pp. 1083–1159, Sep 2008.

[13] M. Leijnse and K. Flensberg, "Introduction to topological superconductivity and Majorana fermions," *Semiconductor Science and Technology*, vol. 27, no. 12, p. 124003, 2012.

[14] T. Gamelin and R. Greene, *Introduction to Topology*. Dover books on mathematics, Dover Publications, 1999.

[15] E. Majorana, "Teoria simmetrica dell'elettrone e del positrone," *Il Nuovo Cimento (1924-1942)*, vol. 14, no. 4, p. 171, 1937.

[16] W. Furry, "On transition probabilities in double beta-disintegration," *Physical Review*, vol. 56, no. 12, p. 1184, 1939.

[17] W. Rodejohann, "Neutrino-less double beta decay and particle physics," *International Journal of Modern Physics E*, vol. 20, no. 09, pp. 1833–1930, 2011.

[18] A. Y. Kitaev, "Unpaired Majorana fermions in quantum wires," *Physics-Uspekhi*, vol. 44, no. 10S, p. 131, 2001.

[19] L. Fu and C. L. Kane, "Superconducting proximity effect and Majorana fermions at the surface of a topological insulator," *Physical review letters*, vol. 100, no. 9, p. 096407, 2008.

[20] R. M. Lutchyn, J. D. Sau, and S. D. Sarma, "Majorana fermions and a topological phase transition in semiconductor-superconductor heterostructures," *Physical review letters*, vol. 105, no. 7, p. 077001, 2010.

[21] Y. Oreg, G. Refael, and F. von Oppen, "Helical liquids and Majorana bound states in quantum wires," *Physical review letters*, vol. 105, no. 17, p. 177002, 2010.

[22] J. Davies, *The Physics of Low-dimensional Semiconductors: An Introduction*. Cambridge University Press, 1998.

[23] I. v. Weperen, *Quantum Transport in Indium Antimonide Nanowires*. PhD thesis, Delft University of Technology, 2014.

[24] T. Ihn, *Semiconductor Nanostructures: Quantum States and Electronic Transport*. OUP Oxford, 2010.

[25] H. K. Onnes, "Further experiments with liquid Helium," *Leiden Communications*, no. 120b, pp. 261–263, 1911.

[26] M. Tinkham, *Introduction to Superconductivity*. Dover Books on Physics Series, Dover Publications, 2004.

[27] J. Bardeen, L. N. Cooper, and J. R. Schrieffer, "Theory of superconductivity," *Physical Review*, vol. 108, no. 5, p. 1175, 1957.

[28] R. Dynes, J. Garno, G. Hertel, and T. Orlando, "Tunneling study of superconductivity near the metal-insulator transition," *Physical Review Letters*, vol. 53, no. 25, p. 2437, 1984.

[29] S. Takei, B. M. Fregoso, H.-Y. Hui, A. M. Lobos, and S. D. Sarma, "Soft superconducting gap in semiconductor majorana nanowires," *Physical review letters*, vol. 110, no. 18, p. 186803, 2013.

[30] R. Winkler, *Spin-orbit Coupling Effects in Two-Dimensional Electron and Hole Systems*. Springer Tracts in Modern Physics, Springer Berlin Heidelberg, 2003.

[31] J. Kammhuber, *Spin-orbit interaction in ballistic nanowire devices*. PhD thesis, Delft University of Technology, 2017.

[32] L. H. Thomas, "I. the kinematics of an electron with an axis," *The London, Edinburgh, and Dublin Philosophical Magazine and Journal of Science*, vol. 3, no. 13, pp. 1–22, 1927.

[33] P. Středa and P. Šeba, "Antisymmetric spin filtering in one-dimensional electron systems with uniform spin-orbit coupling," *Physical review letters*, vol. 90, no. 25, p. 256601, 2003.

[34] Y. V. Pershin, J. A. Nesteroff, and V. Privman, "Effect of spin-orbit interaction and in-plane magnetic field on the conductance of a quasi-one-dimensional system," *Physical Review B*, vol. 69, no. 12, p. 121306, 2004.

[35] J. Kammhuber, M. C. Cassidy, F. Pei, M. P. Nowak, A. Vuik, Ö. Gül, D. Car, S. Plissard, E. Bakkers, M. Wimmer, *et al.*, "Conductance through a helical state in an indium antimonide nanowire," *Nature communications*, vol. 8, no. 1, p. 478, 2017.

[36] R. Holm and W. Meissner, "Messungen mit hilfe von flüssigem helium. xiii," *Zeitschrift für Physik*, vol. 74, no. 11-12, pp. 715–735, 1932.

[37] J. Alicea, "Majorana fermions in a tunable semiconductor device," *Physical Review B*, vol. 81, no. 12, p. 125318, 2010.

[38] V. Mourik and K. Zuo, *Signatures of Majorana Fermions in Hybrid Superconductor-Semiconductor Nanowire Devices*. PhD thesis, Delft University of Technology, 2016.

[39] D. van Woerkom, *Semiconductor Nanowire Josephson Junctions: In the search for the Majorana*. PhD thesis, Delft University of Technology, 2017.

[40] Ö. Gül, D. J. Van Woerkom, I. van Weperen, D. Car, S. R. Plissard, E. P. Bakkers, and L. P. Kouwenhoven, "Towards high mobility InSb nanowire devices," *Nanotechnology*, vol. 26, no. 21, p. 215202, 2015.

[41] E. H. Hall, "On a new action of the magnet on electric currents," *American Journal of Mathematics*, vol. 2, no. 3, pp. 287–292, 1879.

[42] L. P. Kouwenhoven, C. M. Marcus, P. L. McEuen, S. Tarucha, R. M. Westervelt, and N. S. Wingreen, "Electron transport in quantum dots," in *Mesoscopic electron transport*, pp. 105–214, Springer, 1997.

[43] B. Van Wees, H. Van Houten, C. Beenakker, J. G. Williamson, L. Kouwenhoven, D. Van der Marel, and C. Foxon, "Quantized conductance of point contacts in a two-dimensional electron gas," *Physical Review Letters*, vol. 60, no. 9, p. 848, 1988.

[44] Y. Nazarov and Y. Blanter, *Quantum Transport: Introduction to Nanoscience*. Cambridge University Press, 2009.

[45] P. A. Lee and A. D. Stone, "Universal conductance fluctuations in metals," *Physical review letters*, vol. 55, no. 15, p. 1622, 1985.

[46] H. Peng, K. Lai, D. Kong, S. Meister, Y. Chen, X.-L. Qi, S.-C. Zhang, Z.-X. Shen, and Y. Cui, "Aharonov–bohm interference in topological insulator nanoribbons," *Nature materials*, vol. 9, no. 3, p. 225, 2010.

[47] G. Ventura and L. Risegari, *The Art of Cryogenics: Low-Temperature Experimental Techniques*. Elsevier Science, 2010.

[48] H. O. McMahon and W. E. Gifford, "A new low-temperature gas expansion cycle," in *Advances in Cryogenic Engineering* (K. D. Timmerhaus, ed.), Springer US, 1960.

[49] F. Pobell, *Matter and Methods at Low Temperatures, 3rd ed.*

[50] R. Schouten, *QT designed instrumentation*. TU Delft, 2010. URL: `http://qtwork.tudelft.nl/~schouten/`, viewed on 27 August 2018.

[51] P. Caroff, J. B. Wagner, K. A. Dick, H. A. Nilsson, M. Jeppsson, K. Deppert, L. Samuelson, L. R. Wallenberg, and L.-E. Wernersson, "High-quality inas/insb nanowire heterostructures grown by metal–organic vapor-phase epitaxy," *Small*, vol. 4, no. 7, pp. 878–882, 2008.

[52] P. Caroff, M. E. Messing, B. M. Borg, K. A. Dick, K. Deppert, and L.-E. Wernersson, "Insb heterostructure nanowires: Movpe growth under extreme lattice mismatch," *Nanotechnology*, vol. 20, no. 49, p. 495606, 2009.

[53] D. Ercolani, F. Rossi, A. Li, S. Roddaro, V. Grillo, G. Salviati, F. Beltram, and L. Sorba, "Inas/insb nanowire heterostructures grown by chemical beam epitaxy," *Nanotechnology*, vol. 20, no. 50, p. 505605, 2009.

[54] S. R. Plissard, D. R. Slapak, M. A. Verheijen, M. Hocevar, G. W. Immink, I. van Weperen, S. Nadj-Perge, S. M. Frolov, L. P. Kouwenhoven, and E. P. Bakkers, "From insb nanowires to nanocubes: looking for the sweet spot," *Nano letters*, vol. 12, no. 4, pp. 1794–1798, 2012.

[55] D. Car, J. Wang, M. A. Verheijen, E. P. Bakkers, and S. R. Plissard, "Rationally designed single-crystalline nanowire networks," *Advanced Materials*, vol. 26, no. 28, pp. 4875–4879, 2014.

[56] J. Gooth, M. Borg, H. Schmid, V. Schaller, S. Wirths, K. Moselund, M. Luisier, S. Karg, and H. Riel, "Ballistic one-dimensional inas nanowire cross-junction interconnects," *Nano letters*, vol. 17, no. 4, pp. 2596–2602, 2017.

[57] L. Desplanque, A. Bucamp, D. Troadec, G. Patriarche, and X. Wallart, "In-plane insb nanowires grown by selective area molecular beam epitaxy on semi-insulating substrate," *Nanotechnology*, vol. 29, no. 30, p. 305705, 2018.

[58] S. Vaitiekėnas, A. Whiticar, M.-T. Deng, F. Krizek, J. Sestoft, C. Palmstrøm, S. Marti-Sanchez, J. Arbiol, P. Krogstrup, L. Casparis, *et al.*, "Selective-area-grown semiconductor-superconductor hybrids: A basis for topological networks," *Physical review letters*, vol. 121, no. 14, p. 147701, 2018.

[59] F. Krizek, J. E. Sestoft, P. Aseev, S. Marti-Sanchez, S. Vaitiekėnas, L. Casparis, S. A. Khan, Y. Liu, T. Stankevič, A. M. Whiticar, *et al.*, "Field effect enhancement in buffered quantum nanowire networks," *Physical Review Materials*, vol. 2, no. 9, p. 093401, 2018.

[60] J. S. Lee, S. Choi, M. Pendharkar, D. J. Pennachio, B. Markman, M. J. Rodwell, P. Krogstrup, and C. J. Palmstrøm, "Selective-area chemical beam epitaxy of in-plane inas one-dimensional channels grown on inp (001) and inp (111) b surfaces," *arXiv preprint arXiv:1808.04563*, 2018.

[61] MicroChem Corp., "Nano pmma and copolymer developer," *Specsheet*, 2001.

[62] L. Morresi, *Basics of Molecular Beam Epitaxy (MBE) technique*. 2013. ISBN: 9781608054565.

[63] M. Ohring, *The Materials Science of Thin Films*. Referex Engineering, Academic Press, 1992. ISBN: 9780125249904.

[64] E. N. Kaufmann, *Characterization of Materials*. No. vol. 2, John Wiley & Sons, Incorporated, 2002.

[65] J. Neave, B. Joyce, P. Dobson, and N. Norton, "Dynamics of film growth of gaas by mbe from rheed observations," *Applied Physics A*, vol. 31, no. 1, pp. 1–8, 1983.

[66] F. Krizek, *Semiconductor Nanowire Networks grown by Molecular Beam Epitaxy*. PhD thesis, University of Copenhagen, 2018.

[67] F. C. Frank and J. Van der Merwe, "One-dimensional dislocations. ii. misfitting monolayers and oriented overgrowth," *Proc. R. Soc. Lond. A*, vol. 198, no. 1053, pp. 216–225, 1949.

[68] M. Azadi *et al.*, "PMMA A2 Contrast Curves," 2016.

[69] D. M. Mattox, "Thin film metallization of oxides in microelectronics," *Thin Solid Films*, vol. 18, no. 2, pp. 173–186, 1973.

[70] D. M. Mattox, *Handbook of physical vapor deposition (PVD) processing*. William Andrew, 2010.

[71] T. V. Lvova, A. L. Shakhmin, I. V. Sedova, and M. V. Lebedev, "Sulfur passivation of InSb (100) surfaces: Comparison of aqueous and alcoholic ammonium sulfide solutions using X-ray photoemission spectroscopy," *Applied Surface Science*, vol. 311, pp. 300–307, 2014.

[72] S. Plugge, A. Rasmussen, R. Egger, and K. Flensberg, "Majorana box qubits," *New Journal of Physics*, vol. 19, no. 1, p. 012001, 2017.

[73] T. Karzig, C. Knapp, R. M. Lutchyn, P. Bonderson, M. B. Hastings, C. Nayak, J. Alicea, K. Flensberg, S. Plugge, Y. Oreg, *et al.*, "Scalable designs for quasiparticle-poisoning-protected topological quantum computation with majorana zero modes," *Physical Review B*, vol. 95, no. 23, p. 235305, 2017.

[74] V. Mourik, K. Zuo, S. M. Frolov, S. Plissard, E. P. Bakkers, and L. P. Kouwenhoven, "Signatures of Majorana fermions in hybrid superconductor-semiconductor nanowire devices," *Science*, vol. 336, no. 6084, pp. 1003–1007, 2012.

[75] H. Zhang, C.-X. Liu, S. Gazibegovic, D. Xu, J. A. Logan, G. Wang, N. Van Loo, J. D. Bommer, M. W. De Moor, D. Car, *et al.*, "Quantized Majorana conductance," *Nature*, vol. 556, no. 7699, p. 74, 2018.

[76] Ö. Gül, H. Zhang, J. D. Bommer, M. W. de Moor, D. Car, S. R. Plissard, E. P. Bakkers, A. Geresdi, K. Watanabe, T. Taniguchi, *et al.*, "Ballistic majorana nanowire devices," *Nature nanotechnology*, vol. 13, no. 3, p. 192, 2018.

[77] S. R. Plissard, I. Van Weperen, D. Car, M. A. Verheijen, G. W. Immink, J. Kammhuber, L. J. Cornelissen, D. B. Szombati, A. Geresdi, S. M. Frolov, *et al.*, "Formation and electronic properties of insb nanocrosses," *Nature nanotechnology*, vol. 8, no. 11, p. 859, 2013.

[78] S. Gazibegovic, D. Car, H. Zhang, S. C. Balk, J. A. Logan, M. W. de Moor, M. C. Cassidy, R. Schmits, D. Xu, G. Wang, *et al.*, "Epitaxy of advanced nanowire quantum devices," *Nature*, vol. 548, no. 7668, p. 434, 2017.

[79] N. Kumar and D. Goswami, "Quantum algorithm to solve a maze: converting the maze problem into a search problem," *arXiv preprint arXiv:1312.4116*, 2013.

[80] T. Lengauer, *Combinatorial algorithms for integrated circuit layout*. Springer Science & Business Media, 2012.

[81] C. Y. Lee, "An algorithm for path connections and its applications," *IRE transactions on electronic computers*, no. 3, pp. 346–365, 1961.

[82] C. Alpert, D. Mehta, and S. Sapatnekar, *Handbook of Algorithms for Physical Design Automation*. Taylor & Francis, 2008.

[83] P. E. Hart, N. J. Nilsson, and B. Raphael, "A formal basis for the heuristic determination of minimum cost paths," *IEEE transactions on Systems Science and Cybernetics*, vol. 4, no. 2, pp. 100–107, 1968.

[84] G. Harman, *Wire Bonding in Microelectronics*. McGraw-Hill Education, 2009.

[85] T. Ando, A. B. Fowler, and F. Stern, "Electronic properties of two-dimensional systems," *Reviews of Modern Physics*, vol. 54, no. 2, p. 437, 1982.

[86] W. Kim, A. Javey, O. Vermesh, Q. Wang, Y. Li, and H. Dai, "Hysteresis caused by water molecules in carbon nanotube field-effect transistors," *Nano Letters*, vol. 3, no. 2, pp. 193–198, 2003.

[87] D. Wang, Y.-L. Chang, Q. Wang, J. Cao, D. B. Farmer, R. G. Gordon, and H. Dai, "Surface chemistry and electrical properties of germanium nanowires," *Journal of the American Chemical Society*, vol. 126, no. 37, pp. 11602–11611, 2004.

[88] L. H. Thomas, "The calculation of atomic fields," in *Mathematical Proceedings of the Cambridge Philosophical Society*, vol. 23, pp. 542–548, Cambridge University Press, 1927.

[89] E. Fermi, "Eine statistische methode zur bestimmung einiger eigenschaften des atoms und ihre anwendung auf die theorie des periodischen systems der elemente," *Zeitschrift für Physik*, vol. 48, no. 1-2, pp. 73–79, 1928.

[90] I. van Weperen, S. R. Plissard, E. P. Bakkers, S. M. Frolov, and L. P. Kouwenhoven, "Quantized conductance in an insb nanowire," *Nano letters*, vol. 13, no. 2, pp. 387–391, 2012.

[91] C. Kurdak, A. Chang, A. Chin, and T. Chang, "Quantum interference effects and spin-orbit interaction in quasi-one-dimensional wires and rings," *Physical Review B*, vol. 46, no. 11, p. 6846, 1992.

[92] A. Ferguson, R. Clark, *et al.*, "Energy gap measurement of nanostructured aluminium thin films for single cooper-pair devices," *Superconductor Science and Technology*, vol. 21, no. 1, p. 015013, 2007.

[93] J. F. Cochran and D. Mapother, "Superconducting transition in aluminum," *Physical review*, vol. 111, no. 1, p. 132, 1958.

[94] W. Chang, S. Albrecht, T. Jespersen, F. Kuemmeth, P. Krogstrup, J. Nygård, and C. M. Marcus, "Hard gap in epitaxial semiconductor–superconductor nanowires," *Nature nanotechnology*, vol. 10, no. 3, p. 232, 2015.

[95] Y. Huang, J. D. Sau, T. D. Stanescu, and S. D. Sarma, "Quasiparticle gaps in multiprobe majorana nanowires," *Physical Review B*, vol. 98, no. 22, p. 224512, 2018.

[96] A. Grivnin, E. Bor, M. Heiblum, Y. Oreg, and H. Shtrikman, "Concomitant opening of a topological bulk-gap with an emerging majorana edge-state," *arXiv preprint arXiv:1807.06632*, 2018.